On-line Optical Operant Conditioning of Cortical Activity

Yuya Kanemoto

University College London

Thesis submitted for the degree of

Doctor of Philosophy

2015

Declaration

I, Yuya Kanemoto, confirm that the work presented in this thesis is my own. Where information has been derived from other sources, this has been indicated.

Abstract

Animals can learn to modify their voluntary behavior to gain rewards in the positive reinforcement form of operant conditioning. It has been shown that animals can also learn to modify neuronal activity that is directly rewarded by using electrophysiological recordings. Electrophysiological approaches exhibit excellent temporal resolution, but do not permit recordings from the same identified neurons in dense local circuits over multiple days. Two-photon calcium imaging makes it possible to observe the activity of the same population of identified neurons in behaving animals over long time periods. Here we introduce a platform to analyze calcium imaging data on-line and feed this neuronal activity back to behaving animals. We have used this approach to investigate how animals modify population activity during operant conditioning. We transfected neurons with adenoassociated virus encoding for the genetically encoded calcium indicator GCaMP6s. While performing calcium imaging, spiking events in multiple neurons could be inferred. Rewards were given to animals in response to inferred events. We found that single neurons in layer 2/3 of motor cortex could be trained to increase activity in a specific manner, and that this increase primes operant conditioning of the same neurons over subsequent days. We also developed 3D two-photon calcium imaging setup to simultaneously record dendritic and somatic activity, with the aim of performing operant conditioning of local dendritic activity. By identifying the neurons that trigger operant conditioning, the approach we have introduced should be useful for localizing plastic changes and determining the parameters that lead to these plastic changes in the dynamics of neuronal populations during learning.

Acknowledgements

I am very grateful to Michael Häusser for giving me the opportunity to work in an exciting environment and supporting this project that has been risky and challenging.

I am truly grateful for all the supervision by Google.com throughout my PhD. It was always there for me anytime I needed help.

My great thanks to Jason Keller for his contribution for developing software and helping the start of the project. I am indebted to Adam Packer for his generous help in experiments and discussions. Particular help at various stages were given by research associates: Spencer Smith, Christian Wilms, Christoph Schmidt-Hieber, Dara Sosulski, Srinivas Turaga, Martha Havenith, Beverley Clark, and Arnd Roth. Thanks to So Chun for all her help in experiments and animal works.

It would have been difficult to carry out this project without support from other lab members, who provided discussions and chats about scientific and non-scientific matters over beers and wines. Particularly thanks go to PhD students and staffs: Charlotte Arlt, Matej Macak, Gabija Toleikyte, James Cottam, Sarah Rieubland, Alex Mathy, Lloyd Russell, Lea Goetz, Matthew Hoddinott, and Arifa Naeem.

Special thanks go to my friends who had drinks with me to forget about unsuccessful experiments. And final thanks go to my family who had been generous and understanding to a bad son who rarely comes home.

Table of contents

List of figures

Abbreviations

AAV	adeno-associated virus
AM	acetoxymethyl
AP	action potential
a.u.	arbitrary unit
bAP	back-propagating action potential
BCI	brain-computer interface
BMI	brain-machine interface
CDF	cumulative density function
ChR2	channelrhodopsin-2
CV	coefficient of variation
DAPI	4,6-diamidino-2-phenylindole
FOV	field of view
FRET	Förster resonance energy transfer
GaAsP	gallium arsenide phosphide
GFP	green fluorescent protein
GUI	graphic user interface
hSyn	human synapsin
IR	infrared

LCD	liquid-crystal display
LED	light-emitting diode
LFP	local field potential
MAD	median absolute deviation
NpHR	halorhodopsin
n.s.	not significant
OGB-1	oregon-green-BAPTA-1
PFC	prefrontal cortex
PMT	photomultiplier tube
PV	parvalbumin
RFP	red fluorescent protein
ROI	region of interest
SD	standard deviation
SEM	standard error of the mean
SNR	signal-to-noise ratio
SOM	somatostatin
STA	spike-triggered average
STDP	spike-timing dependent plasticity
VTA	ventral tegmental area
YFP	yellow fluorescent protein

1 Introduction

1.1 Neural circuits and information

One of the most important and challenging questions in neuroscience is how information is coded in the brain. Classically researchers have suggested three coding schemes: rate coding, temporal coding, and population coding (Dayan and Abbott, 2001). Rate coding model states that information is contained in the frequency of spikes. For example firing rate of neurons increases with increasing stimulus intensity in many sensory systems (Kandel, 2013). Temporal coding model states that information is contained in the precise spike timing or fluctuation of spike rate. Precise timing of first spike relative to the stimulus carries information in some sensory systems (Gollisch and Meister, 2008; Uchida et al., 2014). Spike timings relative to the phase of LFP oscillation precede along animal's movement in hippocampus and entorhinal cortex, known as phase precession (O'Keefe and Recce, 1993; Harris et al., 2002; Hafting et al., 2008; Harvey et al., 2009; Burgess and O'Keefe, 2011). Population coding model states that information is contained in the combination of activity of neuronal population. Direction of arm movement can be predicted from population vector of neuronal activity in motor cortex (Kalaska et al., 1983; Kandel, 2013).

Correlation between activities of neuronal population can carry additional information (Averbeck and Lee, 2004; Averbeck et al., 2006) with modulation by brain states (e.g., attention) (Poulet and Petersen, 2008; Cohen and Maunsell, 2009; Mitchell et al., 2009).

A

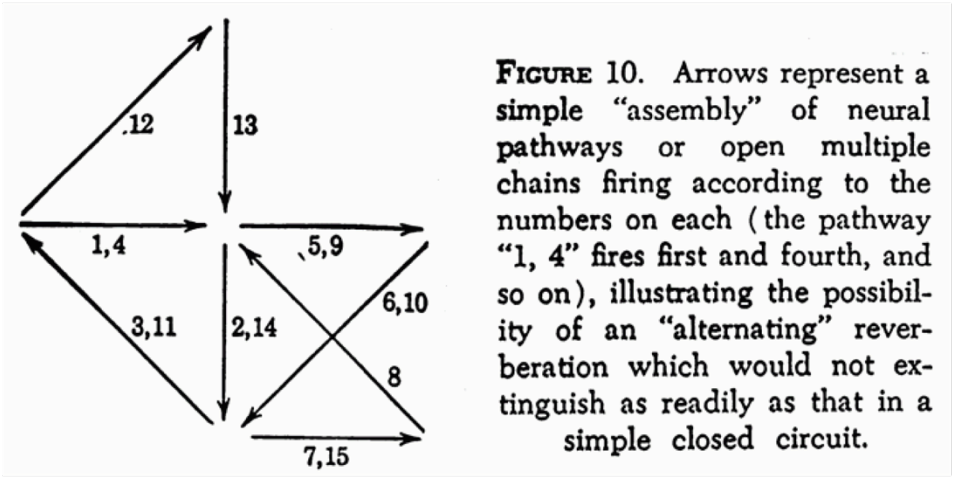

FIGURE 10. Arrows represent a simple "assembly" of neural pathways or open multiple chains firing according to the numbers on each (the pathway "1, 4" fires first and fourth, and so on), illustrating the possibility of an "alternating" reverberation which would not extinguish as readily as that in a simple closed circuit.

Hebb (1949)

B

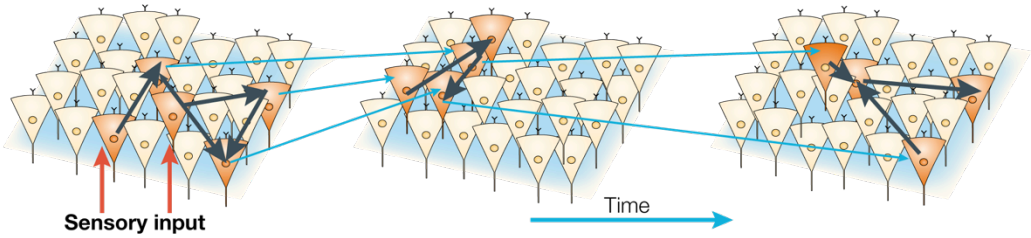

Harris (2005)

Figure 1.1 Cell assembly hypothesis

A, Activity of cell assembly described by Hebb with original legend for the figure (Hebb, 1949). **B**, Cartoon of evolution of assembly's activity. Sensory input (red arrows) drives certain neurons to fire. Thereafter, activity evolves owing to intrinsic cortical dynamics. Strengthened recurrent connections between

members of an assembly (black arrows) transiently stabilize assembly firing through mutual excitation. As the excitability of this assembly fades, inter-assembly connections (blue arrows) lead to subsequent activation of a new assembly. (Harris, 2005)

Another influential idea for population coding, called cell assembly, was proposed by Donald Hebb in his book *The Organization of Behavior* (Hebb, 1949) (Fig1.1). Cell assembly is defined as a network of neurons that is being activated repeatedly during a certain cognitive process and in this way the excitatory synaptic connections among its members are being strengthened (Hopfield, 1982; Nicolelis et al., 1997; Harris, 2005; Fujisawa et al., 2008; Buzsáki, 2010; Wallace and Kerr, 2010). This idea is based on Hebb's another influential idea, called Hebb's rule, stating that any two cells or systems of cells that are repeatedly active at the same time will tend to become associated so that activity in one facilitates activity in the other (Hebb, 1949). Neuronal activity of members evolves owing to mutual excitation and maintains its activity without continuous external stimulation, and this characteristic allows the internal factors initiate the evolution of activity. That is, cell assembly hypothesis states that the same assembly can be triggered either by external sensory stimuli or internal cognitive processes. This feature is in concert with experimental evidences that spontaneous population activity pattern and stimulus-triggered population activity pattern can be very similar (Kenet et al., 2003; MacLean et al., 2005; Han et al., 2008; Xu et al., 2012b; Bermudez Contreras et al., 2013; Miller et al., 2014). Cell assembly can be modeled as a Hopfield network that utilizes Hebb's rule and describes how a network can learn and recall activity patterns with its attractor dynamics (Hopfield, 1982).

Researchers have been investigating cell assembly for decades, but the mechanisms of the formation and evolution of assembly are not well understood largely due to technical limitations and difficulty in defining assembly (Buzsáki, 2010).

1.2 Organization of cortical circuits

Cortical circuits are organized with interconnections within/between cortical layers, and with other brain areas (i.e., other cortex, thalamus, striatum, etc.) (Douglas and Martin, 2004; Thomson and Lamy, 2007; Harris and Mrsic-Flogel, 2013). Here I discuss about primary motor cortex of rodents, especially layer 2/3 neurons, in which I mainly performed our experiments in the following chapters.

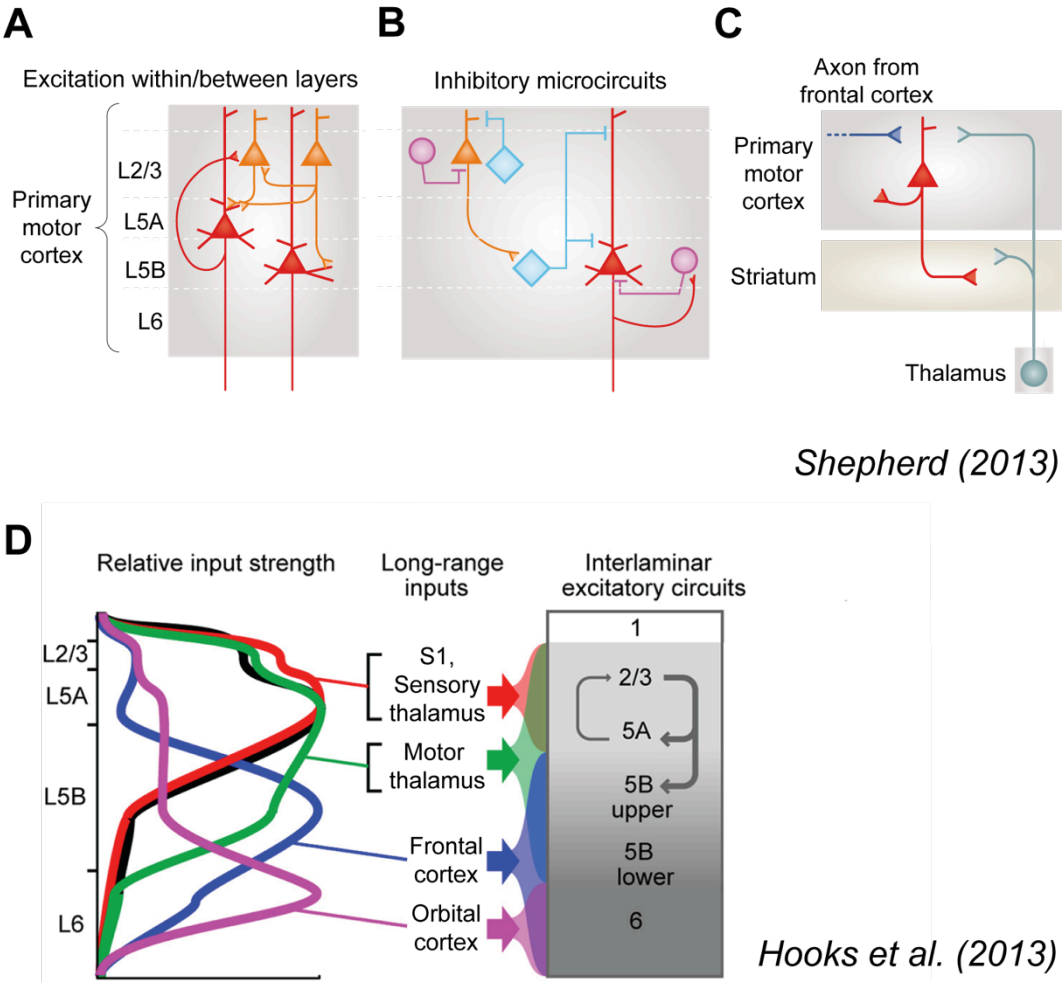

Figure 1.2 Organization of motor cortex and related areas

A, Excitatory connections within/between layers in primary motor cortex. Layer 2/3 and 5 neurons are described in orange and red, respectively. **B**, Microcircuits involving inhibitory interneurons. PV-positive interneurons (purple) innervate cell bodies of excitatory neurons (orange and red), whereas SOM-positive interneurons (blue) innervate dendrites of excitatory neurons. **C**, Both thalamus (gray) and frontal cortex (blue) innervate excitatory neurons in primary motor cortex at their dendritic tufts. Both neurons in primary motor cortex and thalamus innervate striatum. (A-C) were modified from Shepherd (2013). **D**, Circuit diagram for lamina-specific long-range excitation to primary motor cortex. (left) Schematic showing the relative input strength from each pathway to layers in primary motor cortex. Inputs are from sensory thalamus (red), motor thalamus (green), frontal cortex (blue), orbital cortex (magenta), and primary somatosensory cortex (black). (right) A circuit diagram for excitatory inputs to primary motor cortex.

Interlaminar excitatory circuits between primary motor cortex pyramidal neurons are dominated by descending pathways. Modified from Hooks et al. (2013).

Primary motor cortex is mainly innervated by axons from thalamus, other cortical areas (e.g., frontal cortex, somatosensory cortex), and primary motor cortex in a recurrent way (Hooks et al., 2013; Kaneko, 2013; Shepherd, 2013). Layer 2/3 neurons in primary motor cortex receive excitatory inputs from layer 2/3 and 5 neurons in primary motor cortex (Fig1.2A, D). Inhibitory inputs onto layer 2/3 neurons come mainly from PV-positive interneurons at soma, and SOM-positive interneurons at dendrites (Fig1.2B). Layer 2/3 neurons in primary motor cortex receive long-range excitatory inputs mainly from frontal cortex and thalamus (Fig1.2C), but also from somatosensory cortex and orbital cortex with various relative strength across layers (Fig1.2D).

1.3 Operant conditioning

1.3.1 Operant conditioning of behavior

Animals can learn to modify their voluntary behavior in light of its consequences, this is called operant conditioning (Ferster and Skinner, 1957). Classical Pavlovian conditioning requires associations between conditional and unconditional stimuli, whereas operant conditioning requires associations between voluntary behavior and stimulus. In positive reinforcement form of operant

conditioning, animals obtain more appetitive stimulus (e.g. water reward) following correct behavior.

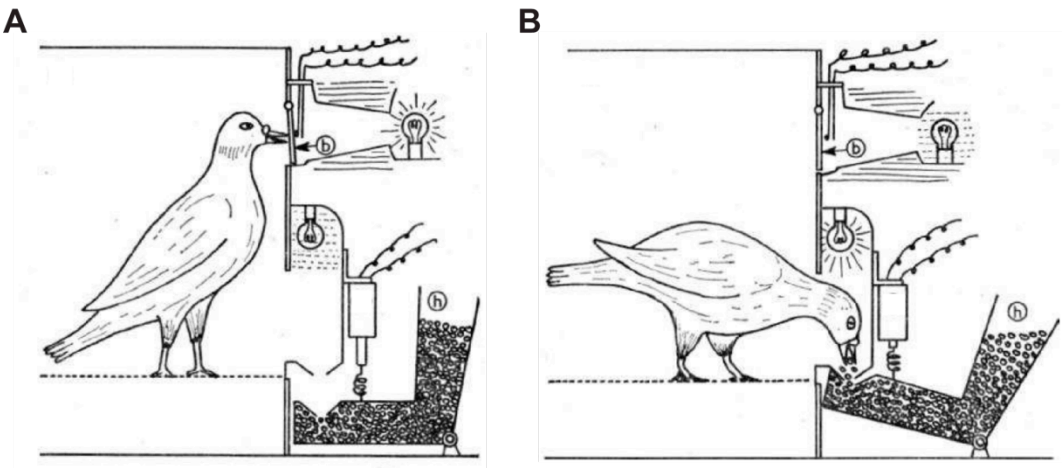

Figure 1.3 Operant conditioning with Skinner box

A, A pigeon just made a contact with the pecking button (b). **B**, This peck is reinforced with the grain in the hopper (h) for a few seconds. Modified from Ferster and Skinner (1957).

Skinner invented the operant conditioning chamber, often called Skinner box, in which animals were isolated from external stimuli and able to make voluntary behaviors (Ferster and Skinner, 1957). Specific voluntary behavior was reinforced, and the rate of the behavior was recorded in the chamber. For example pigeons under food restriction were rewarded with grains in response to their contact with the pecking button in the Skinner box, and they learned to associate the behavior and the reinforcement (Fig1.3). The combination of operant conditioning and neuroscientific recordings has been considered to be a key approach to investigate the neuronal structures for learning.

Dopaminergic system is one of the most studied candidates for biological substrates of reinforcement learning (Wise et al., 1989; Schultz et al., 1997; Schultz, 2006; Boureau and Dayan, 2010). Dopaminergic neurons in ventral tegmental are (VTA) increase their activity when animals predicted reward, and decrease their activity when no reward occurred (Schultz et al., 1997; Schultz, 2006). This neuronal dynamics could be explained as coding of reward prediction error, and can be modeled with temporal difference learning (Niv et al., 2005; Schultz, 2006). As a matter of fact animals can learn to associate voluntary behavior and electrical stimulation of medial forebrain bundle (MFB), which contains dopaminergic axons from VTA to nucleus accumbens, without actual appetitive stimuli (Wise, 1996; Carlezon et al., 2007).

1.3.2 Operant conditioning of neuronal activity

Given the assumption that activity in motor cortex results in behavior, it is straightforward to think that I might be able to perform operant conditioning experiments in which animals obtain reward in response to volitional control neuronal activity instead of behavior. Fetz proved this hypothesis to be true (Fetz, 1969; Fetz and Baker, 1973; Fetz, 2007).

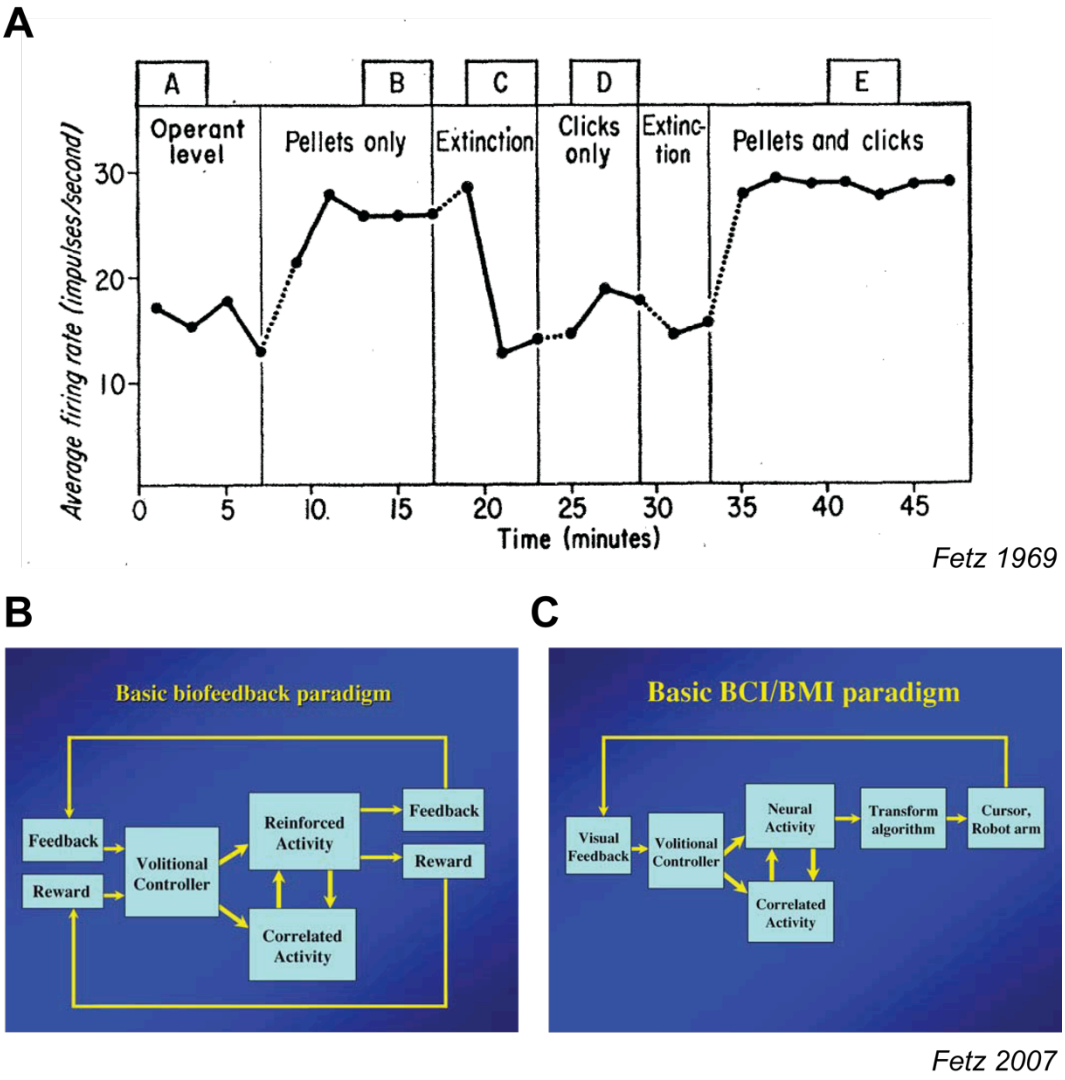

Figure 1.4 Volitional control of neuronal activity

A, Firing rate of motor cortex neuron of a macaque monkey as a function of reinforcement schedule. During operant level and extinction periods neither food nor click feedback was presented. During pellets only period the highest firing rates were reinforced with delivery of a food pellet, without click feedback. During clicks only period a click was presented for each firing of the neuron. At the end of schedule both pellets and clicks were provided. Adapted from Fetz (1969). **B**, Basic components of operant conditioning biofeedback paradigm. Feedback and reward are contingent on the reinforced activity and provided to the brain of the 'volitional controller'. The correlated activity consists of additional neuronal or physiological activity either causally or adventitiously associated with the reinforced activity. **C**, Basic components of the BMI paradigm. Essential

components are identical to those of the biofeedback paradigm, except that feedback is provided by the controlled device or cursor and a more sophisticated transform algorithm is typically used to convert neuronal activity to the requisite control signals. (B, C) are adapted from Fetz (2007).

Fetz performed single-unit recording from neuron in motor cortex of macaque monkey, and gave animal food reward in response to the spikes of the recorded neuron (Fig1.4A). Animal learned to volitionally increase the activity of the neuron when the spikes were followed by food pellets with/without click sounds, whereas the neuronal activity decreased to the baseline when no rewards were given following the spikes (Fetz, 1969).

Basic components of operant conditioning biofeedback paradigm consist of reinforced neuronal activity, rewards/feedbacks that is contingent on the reinforced activity, and 'volitional controller' in the brain that receive rewards/feedbacks signals (Fetz, 2007) (Fig1.4B). Correlated activity, which is either causally or adventitiously associated with reinforced activity, will need to be considered for deeper understanding of operant conditioning.

Operant conditioning of neuronal activity with single-unit recordings have been performed in motor cortex (Fetz, 1969; Fetz and Baker, 1973) and PFC (Kobayashi et al., 2010). Single neuron activity has also been conditioned using *in vivo* whole-cell recording in hippocampus (Ishikawa et al., 2014). To observe correlated activity as well as reinforced activity during the task, population neuronal activity needs to be recorded. Operant conditioning have been carried

out with multi-unit recordings in motor cortex (Koralek et al., 2012; Koralek et al., 2013) and hippocampus (Sakurai and Takahashi, 2012).

Volitional control of neuronal activity has also been utilized in brain-machine interface (BMI) studies (Fetz, 2007). Basic components of BMI paradigm are essentially identical to those of operant conditioning biofeedback paradigm, except that feedback (usually visual) is provided by the controlled device or cursor and a more sophisticated transform algorithm is typically used to convert neuronal activity to the requisite control signals (Fig1.4C). BMI studies have been carried out mainly with neuronal activity in motor cortex of primates/rodents to control robotic arms (Chapin et al., 1999; Wessberg et al., 2000; Carmena et al., 2003), computer cursor (Ganguly and Carmena, 2009; Moritz and Fetz, 2011), and paralyzed arm of their own (Moritz et al., 2008). Humans also learned to volitionally control the neuronal activity of medial temporal lobe (Cerf et al., 2010) and visual cortex (Shibata et al., 2011).

Unlike operant conditioning of behavior, operant conditioning of neuronal activity allows us to train animals based on arbitrary neuronal network pattern. The activity pattern for the training can be artificial ones that do not show up during behavior or innate ones that do show up, and the network that emerge through training could reflect hard-wired assemblies or simply the result from low-dimensional strategies to explore the neural space (Jarosiewicz et al., 2008; Legenstein et al., 2008; Legenstein et al., 2010; Garner et al., 2012; Law et al., 2014; Sadtler et al., 2014).

1.4 Two-photon calcium imaging

1.4.1 Two-photon microscopy

The brain consists of fine structures, scale ranging from a micrometer (e.g., spines) to centimeters (e.g., neural circuits). Neuronal tissues strongly scatter light, making it difficult to perform deep imaging with high spatial resolution (Svoboda and Yasuda, 2006). Confocal microscopy resolved this issue to some extent by rejecting fluorescence from off-focus locations with its pinhole, but its application is still limited to the surface (tens of micrometers) of tissues (Centonze and White, 1998; Conchello and Lichtman, 2005; Helmchen and Denk, 2005).

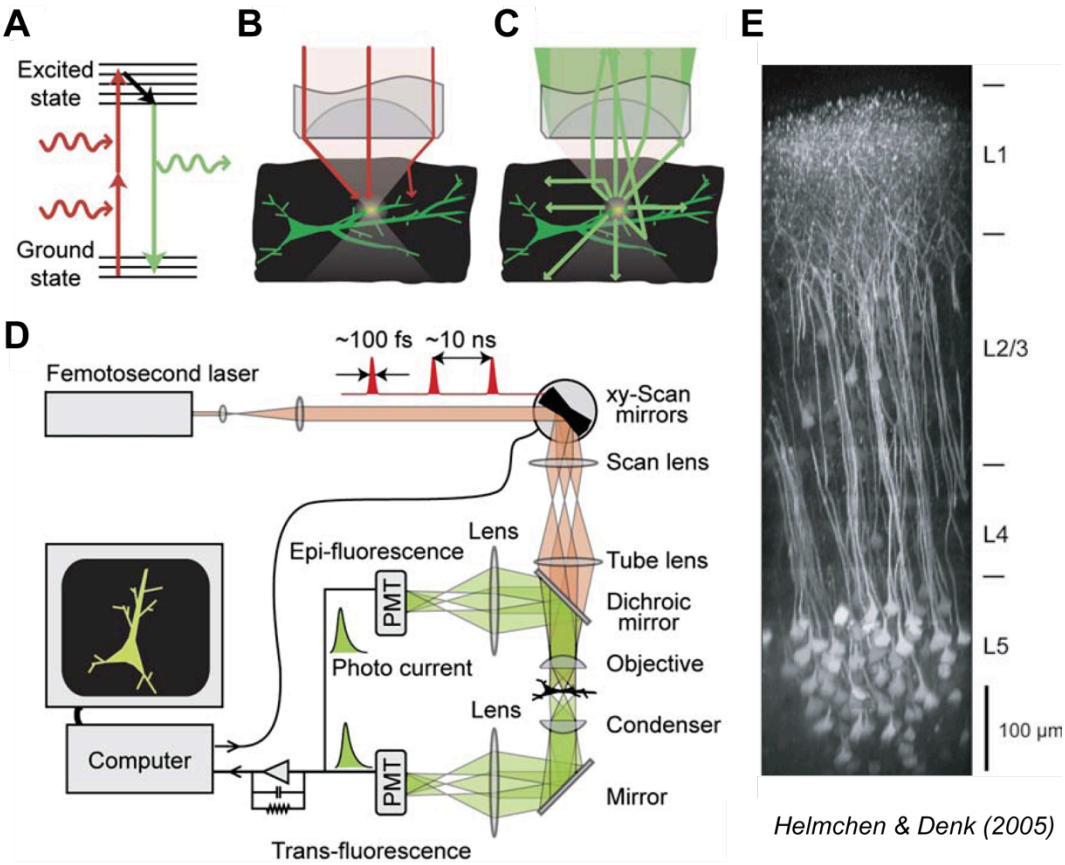

Figure 1.5 Two-photon microscopy

A, Simplified Jablonski diagram of the two-photon excitation process. **B**, Localization of excitation in a scattering medium (black). The excitation beam (red) is focused to a diffraction-limited spot by an objective where it excites green fluorescence in a dendritic branch, but not in a nearby branch. The paths of two ballistic photons and one scattered photon are shown (red lines). Scattered photons are too dilute to cause off-focus excitation. The intensity of the beam decreases with depth as an increasing number of excitation photons are scattered. **C**, Fluorescence collection in a scattering medium. Fluorescence photons are emitted isotropically from the excitation volume (red lines). Even scattered fluorescence photons contribute to the signal if they are collected by the objective. Since the field of view for detection is larger than for excitation, the fluorescence light exciting the objective back-aperture will diverge substantially (green). **D**, Schematic of a two-photon excitation microscope with epifluorescence and trans-fluorescence detection. (A-D) are adapted from

Svoboda (2006). **E**, Example of deep two-photon imaging in mouse neocortex. Maximum-intensity side projection of a fluorescence image stack, obtained in a transgenic mouse expressing YFP-variant under Thy1-promoter, preferentially in deep layer 5 pyramidal cells. (E) is adapted from Helmchen (2005).

Nonlinear optical microscopy is less sensitive to light scattering and thus well suited for high resolution imaging in deep tissues (Helmchen and Denk, 2002; Zipfel et al., 2003). Two-photon laser scanning fluorescent microscopy allows us to image fine structures in intact tissues *in vitro* and living animals *in vivo* (Denk et al., 1990; Helmchen and Denk, 2005; Svoboda and Yasuda, 2006) (Fig1.5). Specimens as diverse as brain, kidney, heart, and so on can be examined in detail at depths of up to one millimeter (Rubart, 2004; Molitoris and Sandoval, 2005).

In two-photon excitation of fluorescence, two low-energy photons cooperate to cause a higher energy electronic transition in a fluorescent molecule (Fig1.5A). Two-photon excitation is a nonlinear process in that the absorption rate depends on the second power of the light intensity. In a focused laser, the intensity is highest near the focus and drops off quadratically with distance above and below. As a result, fluorophores are excited almost exclusively in a tiny diffraction-limited focal volume (Fig1.5B). Since the excitation occurs only in the focal volume, all fluorescence photons captured by the objective are from target structure (Fig1.5C). The key difference between confocal microscopy and two-photon microscopy is that confocal microscopy achieves high resolution at detection side with its pinhole, whereas two-photon microscopy achieves high resolution at excitation side with its localized excitation. Mode-locked Ti:sapphire lasers are used to achieve efficient two-photon excitation process, lasers are

scanned over specimens by galvanometers, and fluorescence are detected by photomultiplier tube (PMT) (Fig1.5D). Two-photon microscopy allows us to image cortical structures, which is about a millimeter deep in mice, *in vivo* (Fig1.5E).

1.4.2 Calcium imaging

Electrophysiological techniques (e.g., multi-unit recordings) enable us to observe activity of neuronal population with high temporal resolution. However these approaches usually do not permit recordings from the same identified neurons over multiple days, and separating neuronal signals in dense local circuits (Ganguly and Carmena, 2009; Einevoll et al., 2012; Lutcke et al., 2013). Two-photon population calcium imaging makes it possible to observe the activity of the same population of identified neurons in behaving animals over long time period (Dombeck et al., 2007; Komiyama et al., 2010; Huber et al., 2012). Two-photon calcium imaging also allows us to combine extraction of geometrical information of neuronal population, identifying/recording of silent cells that will not be detected with extracellular recording, and cell-type specific identification/manipulation using genetic engineering (Dombeck et al., 2010; Komiyama et al., 2010; Chen et al., 2015).

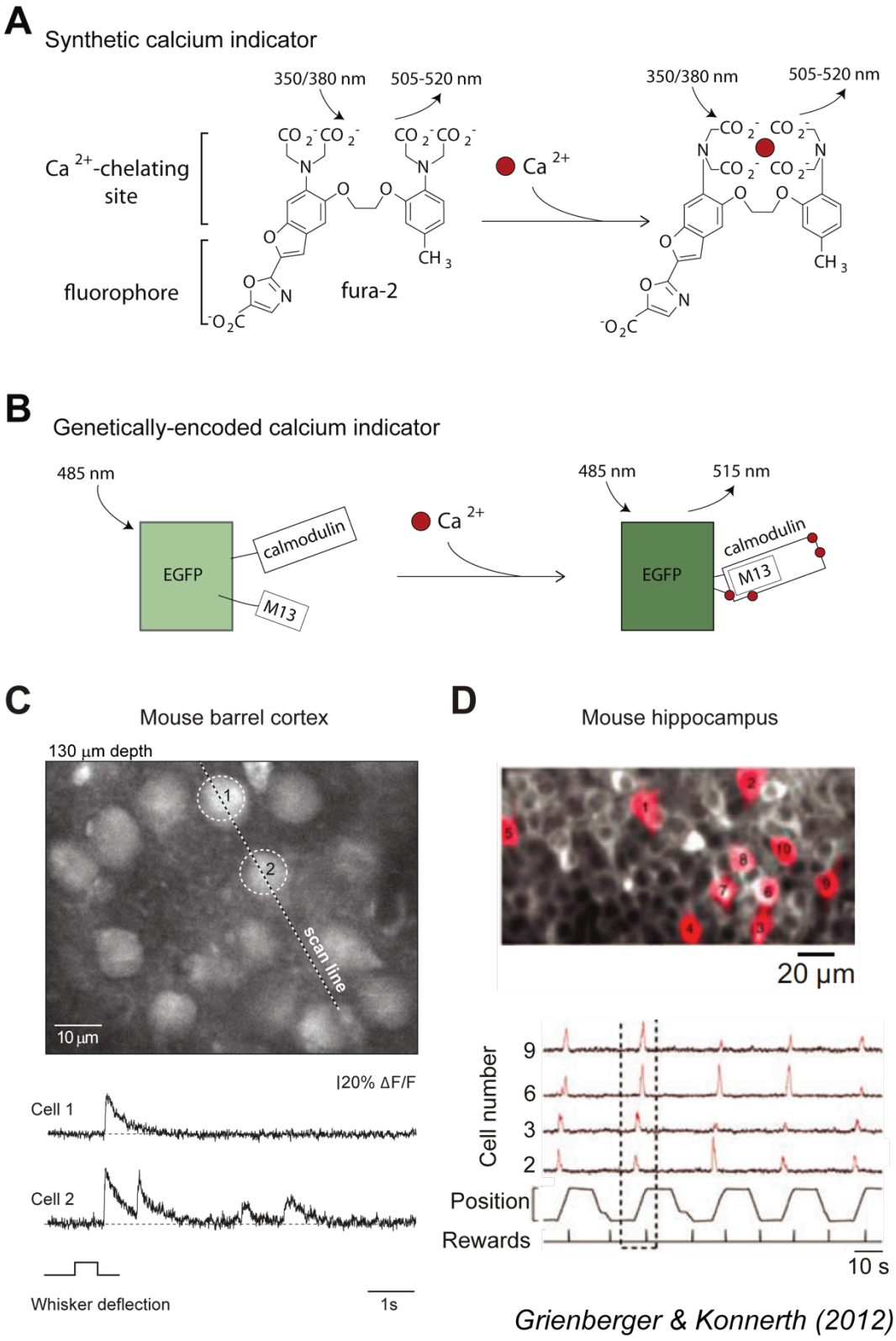

Figure 1.6 *In vivo* calcium imaging

A, Synthetic calcium indicator. Fura-2 is excitable by UV light (e.g., 350/380 nm)

and its emission peak is between 505 and 520 nm. The binding of calcium ions by fura-2 leads to changes in the emitted fluorescence (Grynkiewicz et al., 1985). **B**, Genetically-encoded calcium indicator. After binding of calcium to GCaMP conformational intramolecular changes lead to an increase in the emitted fluorescence of 515 nm (Nakai et al., 2001). **C**, *In vivo* recordings of calcium transients evoked by whisker deflection in mouse barrel cortex. (top) Image of layer 2/3 neurons with description of scan line. (bottom) Line-scan recordings of calcium transients evoked in two neurons by a deflection of the majority of whiskers on the contralateral side of the mouse's snout. The position of the scanned line and the neurons analyzed are indicated in (top) (Stosiek et al., 2003). **D**, Calcium imaging of place cells in the CA1 hippocampal region of mice. (top) Two-photon image of neurons in CA1 labeled with GCaMP3. (bottom) Imaging CA1 place cells while the mouse is running along a virtual linear track. Calcium traces are shown in black, significant calcium transients are indicated in red. The respective regions of interest are shown in (top) (Dombeck et al., 2010). All figures are adapted from Grienberger and Konnerth (2012).

Optical recordings using microscopy allow us to observe neuronal activity in fine structures (Peterka et al., 2011). Especially calcium imaging offers us high SNR signals primarily owing to the huge calcium concentration difference between inside and outside the cell (Grienberger and Konnerth, 2012). Calcium indicators have been the key factor in the development of calcium imaging.

Synthetic calcium indicators (e.g., fura-2, OGB-1) are a combination of calcium chelator and fluorophore (Grynkiewicz et al., 1985) (Fig1.6A). The binding of calcium ions causes intramolecular conformational changes that lead to a change in the emitted fluorescence. Action potentials and postsynaptic potentials cause huge calcium influx into the cell through voltage-gated calcium channels, NMDA

receptors, etc. (Grienberger and Konnerth, 2012). Thus, fluorescence change of calcium indicators inside the cell can be used as a proxy of neuronal activity.

Genetically-encoded calcium indicators are usually either ones with a single-fluorophore (Nakai et al., 2001; Tian et al., 2009; Zhao et al., 2011; Akerboom et al., 2012; Chen et al., 2013b), or ones involving FRET (Nagai et al., 2004; Mank et al., 2008; Thestrup et al., 2014). A representative of genetically-encoded calcium indicators especially for *in vivo* applications is the GCaMP family (Nakai et al., 2001; Tian et al., 2009; Dombeck et al., 2010; Akerboom et al., 2012; Harvey et al., 2012; Huber et al., 2012; Petreanu et al., 2012; Chen et al., 2013b; Peters et al., 2014). GCaMPs consist of a circularly permuted enhanced GFP, which is flanked on one side by the calcium-binding protein calmodulin and on the other side by the calmodulin-binding peptide M13 (Nakai et al., 2001). In the presence of calcium, calmodulin-M13 interactions elicit conformational changes in the fluorophore environment that lead to an increase in the emitted fluorescence (Fig1.6B).

For *in vivo* population imaging, synthetic calcium indicators are usually introduced to neurons by bolus loading in the form of acetoxymethyl (AM) ester (Stosiek et al., 2003). AM ester indicators get trapped inside the cell once they enter the cells and intracellular esterase removes the hydrophobic ester residue of indicators. Fig1.6C shows that *in vivo* two-photon calcium imaging with AM calcium indicators allows us to observe how layer 2/3 neurons in mouse barrel cortex respond to whisker stimulation with single-cell resolution (Stosiek et al., 2003). Genetically-encoded calcium indicators are usually introduced to neurons either with viral transduction (Monahan and Samulski, 2000; Dittgen et al., 2004),

or using transgenic mice (Chen et al., 2012; Zariwala et al., 2012). Fig1.6D shows that *in vivo* two-photon calcium imaging with GCaMP transfected via AAV allows us to observe activity of place cells in CA1 hippocampal region with geometrical information of each cells while the mouse is running along a virtual linear track (Dombeck et al., 2010).

1.5 Dendritic computation

Neurons receive synaptic inputs onto dendrites, and compute outputs with integration of the inputs (London and Häusser, 2005).

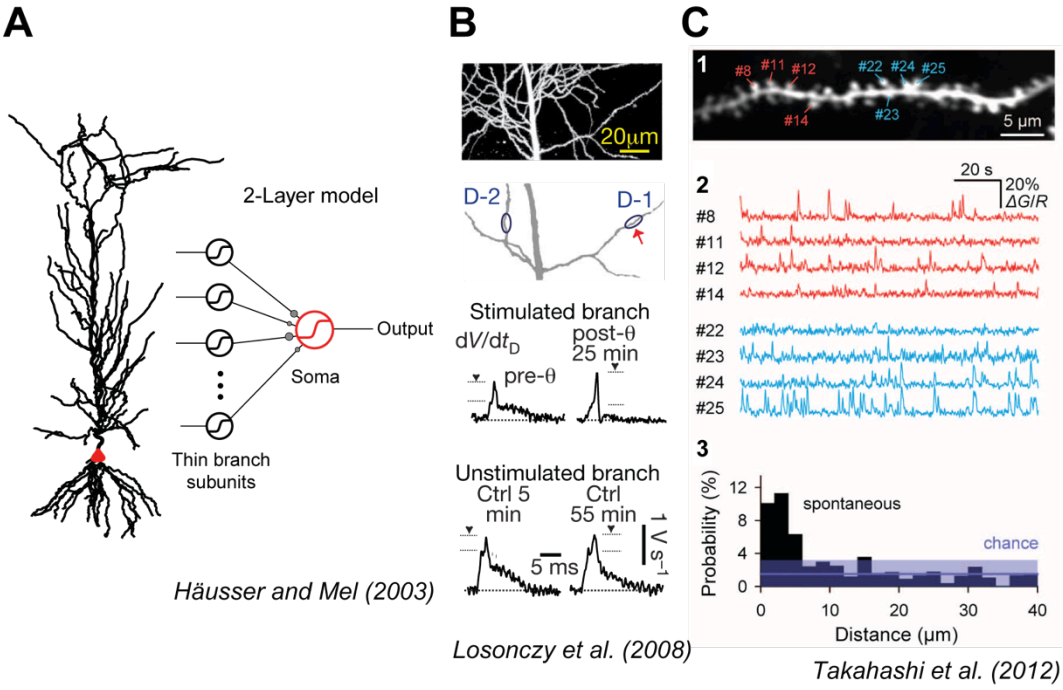

Figure 1.7 Dendrites as a functional subunit

A, (left) CA1 pyramidal cell morphology with soma indicated in red. (right) 2-layer

sum-of-sigmoid model (Poirazi et al., 2003). All thin branches are treated as independent subunits with sigmoidal thresholds whose outputs are summed in the soma. Small grey circles represent subunit weights, which might vary as a function of location or branch order (Hausser and Mel, 2003). **B**, Delivering a theta-burst protocol to individual branches of CA1 pyramidal neurons results in potentiation of dendritic spikes only in the stimulated branch (D-1) (Losonczy et al., 2008). **C**, Spatially-clustered spine calcium transients in layer 2/3 pyramidal cells of the mouse somatosensory cortex. (1) A stack image. (2) Typical traces of spontaneous calcium activity from eight spines shown in (1). (3) The probability of observing coactivated spines as a function of the inter-spine path distance. The chance level and its 95% confidence intervals were indicated in purple (Takahashi et al., 2012).

There have been theoretical models stating that dendrites can perform local computation as a functional subunit, and outputs from these local subunits are subsequently integrated at soma for outputs (Hausser and Mel, 2003; Poirazi et al., 2003) (Fig1.7A). Dendritic branches can perform local computation producing dendritic spikes, and show plasticity for local computation in a branch-specific manner (Losonczy and Magee, 2006; Losonczy et al., 2008; Makara et al., 2009; Branco et al., 2010; Branco and Häusser, 2010; Govindarajan et al., 2011) (Fig1.7B). Clustered synaptic inputs have been proposed to play a key role in local computation at dendritic branches (Losonczy and Magee, 2006; Harvey and Svoboda, 2007; Harvey et al., 2008; Losonczy et al., 2008), and clustering of spontaneous synaptic inputs has been reported *in vivo* (Takahashi et al., 2012) (Fig1.7C). To understand the role of local computation in dendrites for cognitive process, it would be important to monitor local dendritic activity during behavior.

1.6 Hypothesis and aims

1.6.1 Working hypothesis

It has been challenging to define a cell assembly since I have little idea about how large an assembly is, how long its duration/lifetime is, and what exactly does it represent in the cognitive domain (Buzsáki, 2010). Here I would like to propose a hypothesis to define a cell assembly utilizing operant conditioning of neuronal activity.

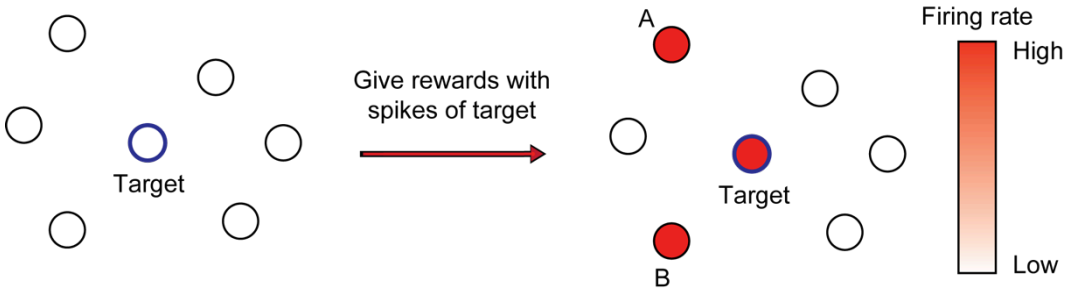

Figure 1.8 Hypothetical observation of cell assembly through operant conditioning

Assuming I perform operant conditioning of activity of target neuron (blue circle), and monitor activity of both target neuron and neurons nearby. Target neuron will increase its firing rate during operant conditioning (Fetz, 1969). If I observe subsets of nearby neurons (A and B) increasing their activity together with target neuron, it is likely that these neurons and target neuron are members of the same assembly.

Animals learn to volitionally increase the activity of target neuron during operant conditioning of target's activity (Fetz, 1969). During learning, I could assume that

animals learn to associate the rewards and the activity of an assembly. Therefore, if I monitor activity of neuronal population and observe subsets of nearby neurons increasing their activity together with target neuron, it is likely that these subsets of neurons and target neuron are in the same assembly (Fig1.8). This definition of cell assembly is potentially able to avoid dealing with the size/lifetime issues for defining an assembly, and could be achievable with utilizing two-photon population calcium imaging from behaving animals.

1.6.2 Aims of the thesis

1. To develop methods to perform operant conditioning of neuronal activity using two-photon population calcium imaging.

2. To perform operant conditioning of neuronal activity using two-photon population calcium imaging.

3. To analyze how target/non-target neurons change their activity during operant conditioning.

4. To perform operant conditioning of dendritic activity using two-photon calcium imaging.

5. To develop the method to monitor local computation in dendrites during behavior.

2 Materials and Methods

2.1 Preparation

All experiments were carried out under license from UK Home Office regulations in accordance with the Animal (Scientific Procedures) Act 1986. The appropriate Personal and Project Licenses (PPL) granted by UK Home Office were in place, and PPL passed ethical review. Imaging experiments were performed on male C57BL/6 mice (6-12 weeks of age).

For acute population imaging (chapter 3 and 4), mice were anesthetized with ketamine (100 mg/kg)/xylazine (15 mg/kg) and a small (<1 mm diameter) craniotomy was opened over whisker-related primary motor cortex 1-2 weeks before the imaging. Mice were then injected with 100-200 nl of AAV2/1-hSyn-GCaMP6s (Chen et al., 2013b) or AAV2/1-hSyn-GCaMP5G (Akerboom et al., 2012) (University of Pennsylvania Vector Core) at a depth of ~350 μm to target layer 2/3 neurons. Custom-designed headplates were attached to the skull with superglue and dental acrylic, and a 2–3 mm diameter craniotomy was opened over the injection site under anesthesia with isoflurane on the day of imaging. The dura mater was left intact. The craniotomy was covered with two layers of coverslips

(a 2 × 2 mm square coverslip and a circle coverslip with 4 mm diameter glued together with optical cement), and the edges glued in place to the skull with superglue and dental acrylic (Holtmaat et al., 2009; Komiyama et al., 2010).

For chronic population imaging (chapter 5), mice were anesthetized with ketamine (100 mg/kg)/xylazine (15 mg/kg) and headplates were attached to the skull with superglue and dental acrylic. A 2–3 mm diameter craniotomy was opened over forelimb-related primary/secondary motor cortex, and the dura mater was left intact. Mice were injected with 100-200 nl of AAV2/1-hSyn-GCaMP6s at a depth of ~350 μm to target layer 2/3 neurons. The craniotomy was covered with two layers of coverslips, and the edges glued in place to the skull with superglue and dental acrylic.

For acute dendritic imaging (chapter 6), mice were anesthetized with ketamine (100 mg/kg)/xylazine (15 mg/kg) and headplates were attached to the skull with superglue and dental acrylic. A 2–3 mm diameter craniotomy was opened over forelimb-related primary motor cortex or whisker-related primary somatosensory cortex, and the dura mater was left intact. Mice were injected with 30-100 nl of mixture of highly diluted (~1:160000) AAV2/1-hSyn-Cre and slightly diluted (1:2-1:4) AAV2/1-hSyn-Flex-GCaMP6s (Atasoy et al., 2008; Chen et al., 2013b) (University of Pennsylvania Vector Core) at a depth of ~350 μm to target layer 2/3 neurons (Fig6.1A, B). The craniotomy was covered with two layers of coverslips, and the edges glued in place to the skull with superglue and dental acrylic.

Mice were habituated under water restriction (to 50% of their daily intake; MPD:92, Mouse Phenome Database at The Jackson Laboratory, (Guo et al.,

2014)) starting 2-3 days after the injection, and operant conditioning with two-photon imaging was carried out 1-2 weeks after the injection. Mice were sitting in an acrylic tube with their head fixed during habituation/operant conditioning. Footrest was attached to the tube to decrease forelimb movements during the task.

2.2 Imaging

For population calcium imaging (chapter 3-5) and dendritic calcium imaging (chapter 6.1), a custom two-photon microscope (Smith and Häusser, 2010) with a 16X, 0.8 numerical aperture (Nikon) water immersion objective and a low-noise photomultiplier tube (7422-40P, Hamamatsu) was used for imaging, in combination with a Ti-Sapphire laser (MaiTai, Spectra Physics) tuned to λ = 910 nm. Images were acquired using ScanImage (Pologruto et al., 2003) at 7 Hz using an image frame of 512 × 256 pixels covering 250 × 250 μm. The typical laser power for imaging was < 50mW under the objective lens.

For 3D dendritic calcium imaging (chapter 6.2), a moving *in vivo* two-photon microscope with resonant galvanometer (Bruker Corporation, formerly Prairie Technologies) with a 16X, 0.8 numerical aperture (Nikon) water immersion objective and a low-noise photomultiplier tube (7422-40P, Hamamatsu) was used for imaging, in combination with a Ti-Sapphire laser (Chameleon Ultra II, Coherent) tuned to λ = 920 nm. Images were acquired using built-in software (Bruker Corporation) at 30 Hz using an image frame of 512 × 512 pixels covering 200 × 200 μm for each plane. 3D two-photon imaging was performed using a

piezoelectric element (Bruker Corporation) at 2-3 Hz with 2-7 imaging planes with 20-30 μm gaps in between.

2.3 Operant Conditioning

Custom-written software with MATLAB (Mathworks, USA) was used for event inference. Two-photon calcium imaging was performed before ('baseline'), during ('epoch 1-4'), and after ('after') the conditioning period. ROIs were drawn by hand (neurons with relatively high baseline activity were preferred) from reference images obtained from baseline recording, and sliding windows of 100 frames before each time point Ire used to infer events. Frame shifts calculated by TurboReg (Thevenaz et al., 1998) during offline motion correction were used as a measure of motion artifacts (Fig3.5), and the motion artifacts were not corrected online during conditioning. I call neurons selected for operant conditioning "target neurons", and other neurons as "non-target neurons" here. Either one or four neurons were selected as target neurons in each session. Events were detected if fluorescent signals exceeded the threshold (= median of baseline + 4 × 1.4 × median absolute deviation of baseline) at the current inference frame, which is one frame delayed from the current imaging frame (Fig3.3A). Inferred event signals were sent to custom-written software with LabVIEW (National Instruments, USA) to give water rewards (9 μl per event) and auditory feedback (14 kHz tone for 0.5 s) to mice. Water rewards were given for each inferred event in any target neuron in a one-to-one manner in multi-target operant conditioning. Training sessions were manually stopped if mice failed to lick for more than 30

seconds, and the training period for further analysis was defined to terminate when mice decreased lick rate to 50% of its maximum lick rate with off-line analysis. The training period (length 15.7 ± 1.5 min, mean ± SEM, n = 14 sessions) was chronologically segmented into four epochs (each length 3.9 ± 0.3 min, mean ± SEM, n = 14 sessions) for time course analysis. In randomized reward experiments, water rewards were given with random intervals at a mean rate of 0.1 Hz, approximately the same as the maximum reward rate during operant conditioning.

2.4 Behavioral recording

Licking was recorded using a lick detector circuit (Slotnick, 2009). The lickometer was kept away from animals before and after the conditioning. Behavior was also monitored with an IR-sensitive webcam in conjunction with an IR LED at 30 Hz during the task. Absolute difference of pixel intensities between two sequential frames were calculated from the acquired video, and ROIs were drawn to select pixels around forelimbs. Forelimb movement events were detected by thresholding the obtained absolute difference values.

2.5 Electrophysiology

An isoflurane-anesthetized mouse with GCaMP6s injected in barrel cortex was used for simultaneous calcium imaging and cell-attached recording. The imaging

was performed at 4.3 Hz with 256 × 256 pixels resolution covering 200 × 200 μm. Cell-attached recording was performed with pipettes (~5 MΩ) containing HEPES-buffered artificial cerebrospinal fluid (150 mM NaCl, 2.5 mM KCl, 10 mM HEPES, 2mM $CaCl_2$ and 1mM $MgCl_2$; pH adjusted with NaOH to 7.3; 300 mmol kg^{-1}) and 50 μM Alexa 594 (Invitrogen) using a MultiClamp 700A amplifier (Molecular Devices) and custom-written data acquisition software (LabVIEW) under the guidance of two-photon imaging. Signals were sampled at 20 kHz. Frames with more than 2 spikes were defined as bursting frames, and the ratio of inferred spiking events to bursting frames detected was defined as the hit rate. Frames without any spikes were defined as silent frames, and the ratio of inferred spiking events to silent frames was defined as the false alarm rate (Fig3.4B). As frames with only one spike did not reliably produce large calcium transients, I excluded these frames from this analysis.

2.6 Histochemistry

Animals with mixture of highly diluted hSyn-Cre and slightly diluted hSyn-Flex-GCaMP6s injection were anesthetized with ketamine (100 mg/kg)/xylazine (15 mg/kg). They were then perfused first with 1X phosphate buffered saline (PBS), then with 4% paraformaldehyde. After fixing overnight 100 μm sections were cut and washed three times for 10 minutes in 1X PBS. Nuclei of neurons were stained with DAPI as a control to indicate sparse expression of GCaMP6s.

Images were collected using a Perkin Elmer Ultra*VIEW* confocal system and

Volocity software. This system allowed for fast imaging of large 3D volumes and accurate stitching offline in Volocity software.

2.7 Data analysis

Images were aligned with TurboReg offline. ROIs were selected by hand to obtain calcium signals of neurons in the field of view. The number of neurons in each FOV was 23.0 ± 2.3 (mean ± SEM, n = 8 FOVs) for multi-target conditioning, and 26.4 ± 2.3 (mean ± SEM, n = 14 FOVs) for single-target conditioning. Slow drifts of fluorescent signals were removed by subtracting 8 percentile value of fluorescent signals in a 15 sec window around each sample time point before detecting events (Dombeck et al., 2010). Spiking events were inferred by the thresholding algorithm used for on-line analysis.

I arbitrarily chose neurons with relatively high baseline activity as targets to enable mice to receive as many rewards as possible per training session during association of a target neuron's activity and rewards (Fig4.4C, Fig5.2E). To compare target and non-target neurons with approximately the same baseline activity assuming targets had been randomly chosen, non-target neurons were classified into two groups: neurons with high baseline activity (non-target control) and ones with low baseline activity (non-target low-baseline). Non-target neurons either with top 50 percentile (Fig4.4C) or top 33 percentile (Fig5.2E) baseline activity were defined as non-target controls so that they have approximately the same baseline with targets ($P > 0.05$, Wilcoxon rank-sum test, n = 32 and 75

neurons for Fig4.4A, n = 6 and 54 neurons for Fig5.2A, n = 8 and 63 neurons for Fig5.2B). In randomized reward experiments, neurons were also classified into neurons with high-baseline (randomized control, top 50 percentile baseline activity) and low-baseline (randomized low-baseline) to compare them with target neurons/non-target controls (Fig4.5A).

Area under the curve of each calcium event (Fig5.2F) was calculated using trapezoidal numerical integration. Correlation between licks and calcium signals were calculated using coefficients from generalized linear model (GLM) fitting. To explain the slow decay of GCaMP6s signals, several temporally filtered calcium signals were used during GLM fitting (Fig5.3C). That is,

$$Ca = g^{-1}\left(a * L + b * Ca_{filtered} + c\right)$$

where Ca is calcium signals, L is lick signals, $Ca_{filtered}$ is temporally filtered calcium signals, g is link function (identity), $a/b/c$ are coefficients. Correlation in Fig5.3C is a in the formula.

Neuropil signal subtraction was performed for the Pearson's correlation coefficient calculation (Fig5.5A). 40 × 40 μm squares around each neuron's center excluding neuronal ROIs were defined as neuropil regions for calculating neuropil signals. Neuropil signals were subtracted from raw calcium signals with a factor of 0.7 (Kerlin et al., 2010; Chen et al., 2013b). Normalized change of event rate (Fig5.5) was defined as (event rate at epoch 4) / (event rate at baseline) – 1. Non-target neurons that showed top 5 percentile spiking events in 12 time bins (±0.21 s window around -1.50, -1.07, -0.64, -0.21, +0.21, +0.64, +1.07, +1.50, +1.92, +2.35, +2.78, +3.21 s from water rewards) were selected to analyze

the relationship between neuronal activity change and spike timings from water rewards (Fig5.5D).

For 3D two-photon calcium imaging, ROIs were selected with free drawing by hand (Fig6.4A, Fig6.6A). Distances between dendrites and soma were defined as the distance between centroids of ROIs for dendrites/soma (Fig6.6C, D). Neuronal identity of dendrites was confirmed with z-stack images (Fig6.4A, Fig6.6A).

Spike-triggered averages (STAs) of calcium signals were analyzed to study how co-active dendrites and soma are (Fig6.5, Fig6.7). Calcium signals of dendrites/soma were triggered by inferred events of dendrites/soma from the same cell. I classified STAs into three categories: positive events, negative events, and gray events (Fig6.5, Fig6.7). STAs were defined as positive events if (1) spiking events were detected, (2) maximum $\Delta F/F_0$ was above 2, and (3) Pearson's correlation coefficient with the source signal for triggering (e.g., somatic auto-STA with spiking event used for triggering dendritic STA) was over 0.4. Likewise, STAs were defined as negative events if (1) spiking events were not detected, (2) maximum $\Delta F/F_0$ was below 2, and (3) Pearson's correlation coefficient with the source signal for triggering was below 0.4. If STAs were not classified into neither positive nor negative events, I called these STAs as gray events since I cannot surely say if dendrite/soma is co-active with soma/dendrite. Linear regression was performed for scatter plot of amplitudes of dendritic calcium signals, and R^2 was used as a measure of how co-active dendrites from the same cell are (Fig6.8).

2.8 Statistics

Circles/columns and error bars represent mean and SEM in figures, respectively. Statistical analysis was performed using Wilcoxon signed-rank test or Wilcoxon rank-sum test unless otherwise mentioned. Multiple comparisons were performed using Bonferroni correction and/or ANOVA. Statistical significance was indicated as ** ($P < 0.01$), * ($P < 0.05$), and n.s. ($P \geq 0.05$).

3 On-line analysis of two-photon calcium imaging

3.1 Introduction

On-line analysis of neuronal activity has been utilized in BMI studies (Lebedev and Nicolelis, 2006; Hatsopoulos and Donoghue, 2009; Nicolelis and Lebedev, 2009; Shibata et al., 2011), and BMI studies have been intensively performed using electrophysiological recordings (Chapin et al., 1999; Wessberg et al., 2000; Carmena et al., 2003). On-line analysis of neuronal activity has also been applied to perform operant conditioning using electrophysiological recordings (Fetz, 1969; Fetz and Baker, 1973; Fetz, 2007; Kobayashi et al., 2010; Schafer and Moore, 2011; Koralek et al., 2012; Ishikawa et al., 2014). Electrophysiological approaches exhibit excellent temporal resolution, but do not permit recordings from the same identified neurons in dense local circuits over multiple days (Einevoll et al., 2012; Lutcke et al., 2013). Two-photon population calcium imaging makes it possible to observe the activity of the same population of identified neurons in behaving animals over long time periods (Dombeck et al.,

2007; Komiyama et al., 2010; Huber et al., 2012; Lutcke et al., 2013). Since conventional analysis techniques for inferring activity from calcium imaging data are computationally slow and often require a great deal of offline analysis, this has precluded the use of calcium imaging in behavioral tasks that require real-time feedback of neuronal activity. Here I have developed a platform to analyze calcium imaging data on-line and feed this neuronal activity back to behaving animals.

3.2 Results

I performed two-photon imaging using the genetically encoded calcium indicator GCaMP6s (Chen et al., 2013b) with a custom two-photon microscope. Images were acquired using MATLAB-based image acquisition software ScanImage (Pologruto et al., 2003), and I developed a custom-written MATLAB-based software to analyze acquired images from ScanImage on-line.

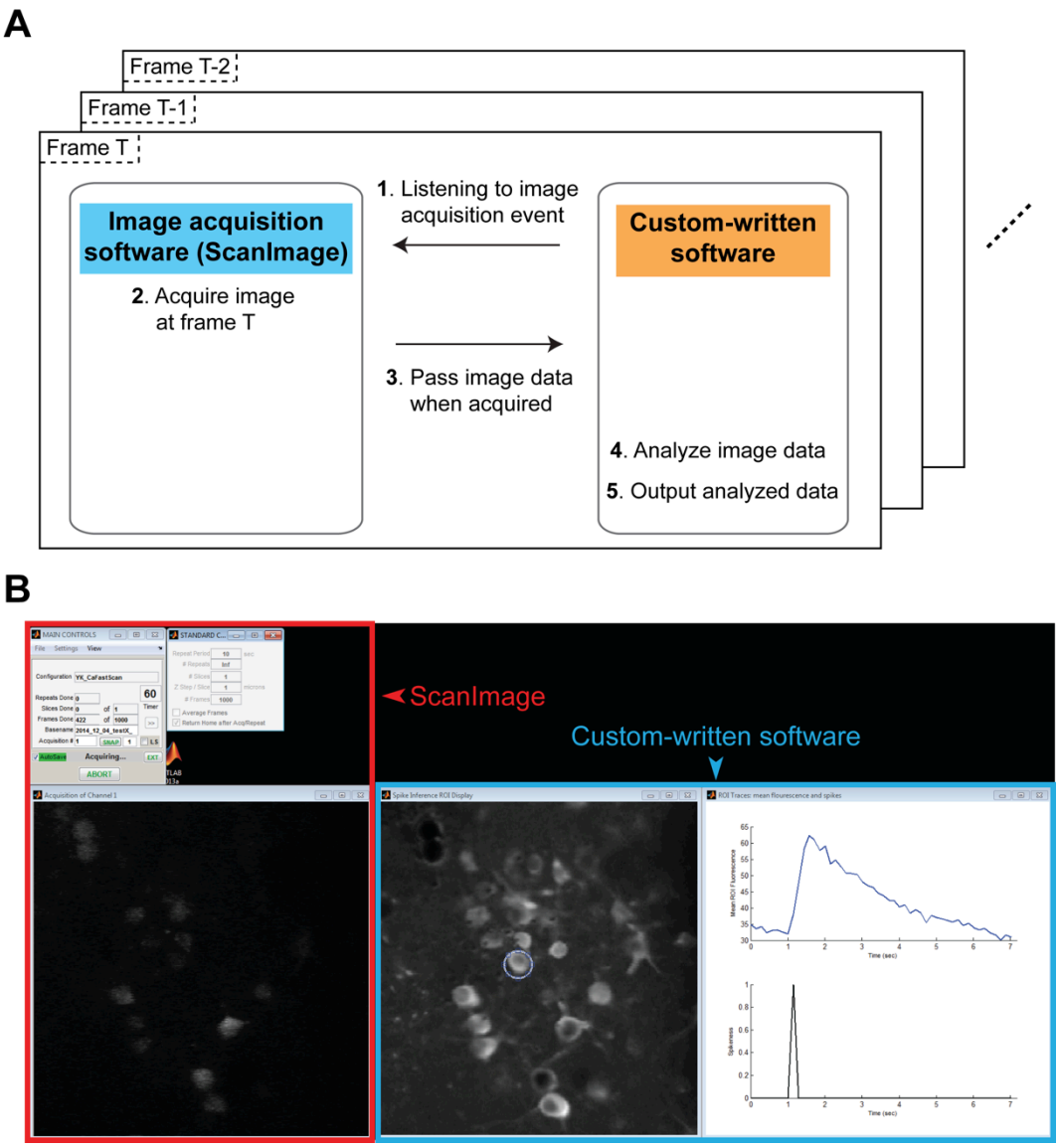

Figure 3.1 Schematic diagram of the algorithm for on-line analysis

A, The diagram shows how the algorithm works at each image acquisition frame (at frame T here). (1) Custom-written software listens to image acquisition software (ScanImage) for the image acquisition event (i.e., the occasion when image acquisition is completed at each frame). (2) ScanImage completes image acquisition at frame T. (3) Custom-written software receives image data from ScanImage. (4) Custom-written software analyzes image data. (5) Custom-written software sends analyzed data as an output to other hardware. **B**, GUIs of Scanimage (left side in red rectangle) and custom-written software (right side in blue rectangle) on the monitor. As for ScanImage, details of imaging setups (top two windows) and live movie of calcium imaging (bottom window) are shown. As

for custom-written software, reference image (left window) to choose ROI (blue circle) and result of on-line analysis (right window) with calcium signal (blue line) and inferred spike (black line) are shown.

Custom-written software waits for the image acquisition completion by ScanImage. Every time ScanImage completes image acquisition, custom-written software retrieves image data from ScanImage. Custom-written software then analyze image data, and send analyzed data to other hardware as an analog /digital output (Fig3.1A). In practice, GUIs for ScanImage consist of setups for imaging and live movie of imaging, and GUIs for custom-written software consist of a reference image to choose ROI and result of on-line analysis. These GUIs from the two software are shown on the same monitor and observed by experimenter (Fig3.1B).

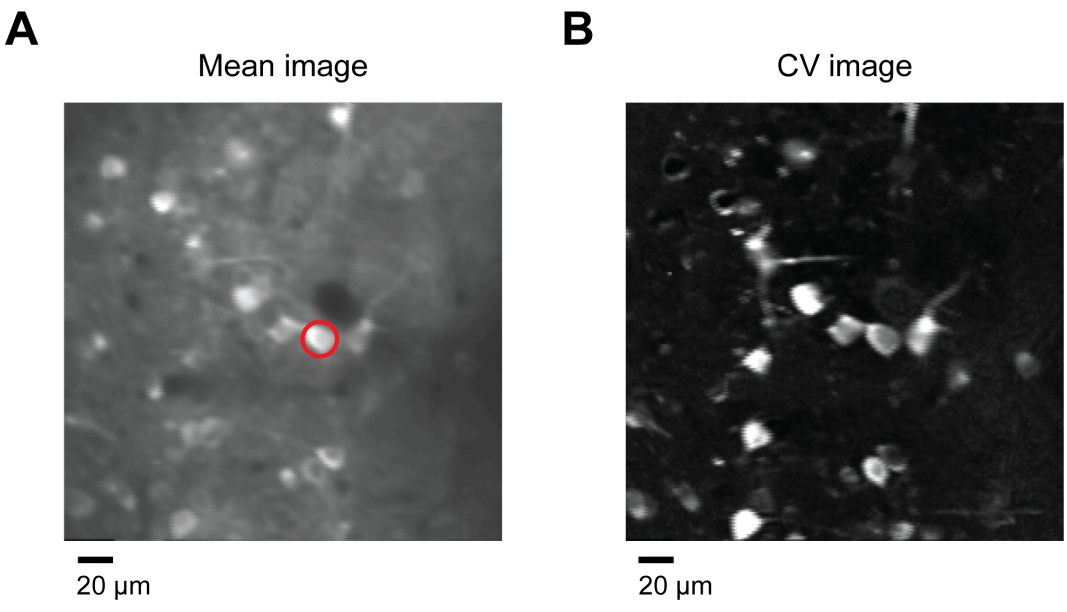

Figure 3.2 Hand selection of ROI from mean/CV image

A, A sample image with a hand-selected ROI (red circle). Mean image, obtained by averaging over time, was used as a sample image. **B**, A sample image using CV obtained from the same movie that produced the mean image in (A).

I acquired a sample image before starting on-line analysis, and ROIs were selected by hand in the field of view (Fig3.1B, Fig3.2A). For the sample image I obtained mean image and coefficient of variation (CV, = *standard deviation / mean*) image (Fig3.2). The mean image shows structure of neurons, and CV image reflects activity-dependent fluorescent changes. I hand-selected neurons using these two images. Fluorescence intensities in each ROI were averaged to obtain calcium signals of neurons. Sliding windows of 100 frames of calcium signals before each acquired time point were used to infer events, i.e., here I have N (number of ROIs) × 100 (number of frames) matrix to infer events for each neurons.

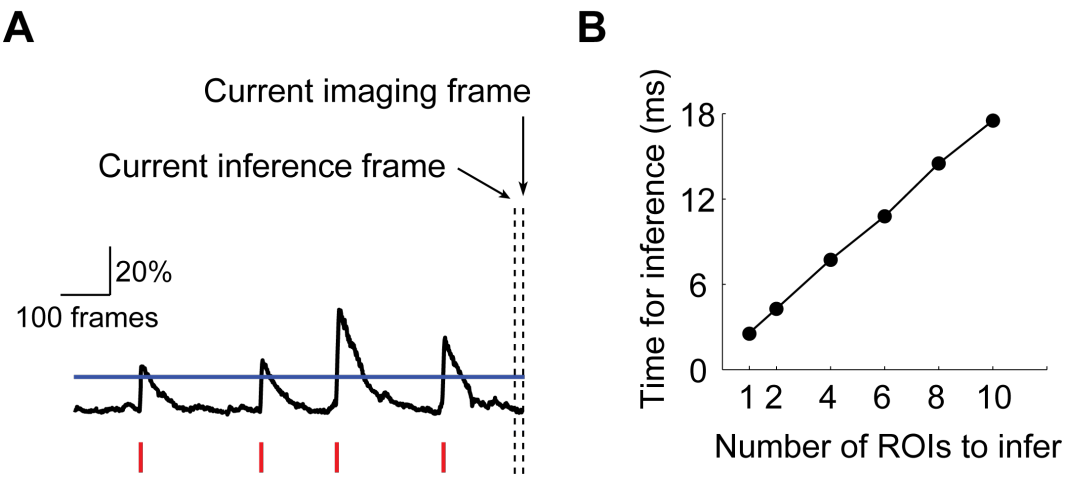

Figure 3.3 Spike inference from calcium signals

A, Spiking events (red) were inferred when the calcium signals (black) crossed the threshold (blue horizontal line). Inference was performed with a one-frame delay from the current imaging frame. **B**, Computational time required for spike inference after the acquisition of inference frame (n = 5 trials).

Although several algorithms exist for inferring events from calcium imaging data (Yaksi and Friedrich, 2006; Greenberg et al., 2008; Vogelstein et al., 2009; Vogelstein et al., 2010), the high signal-to-noise ratio of GCaMP6s allowed us to simply infer events by thresholding calcium signals based on the deviation of the signals in order to maximize processing speed (Fig3.3A). The time required for the inference was then approximately 2 ms for single ROI, and the time linearly increased with the number of ROIs (Fig3.3B). The time lag between the onset of an event and delivery of a water reward was the sum of the time to acquire a single imaging frame (~140 ms at frame rate of 7 Hz) and the time to infer an event from an acquired frame.

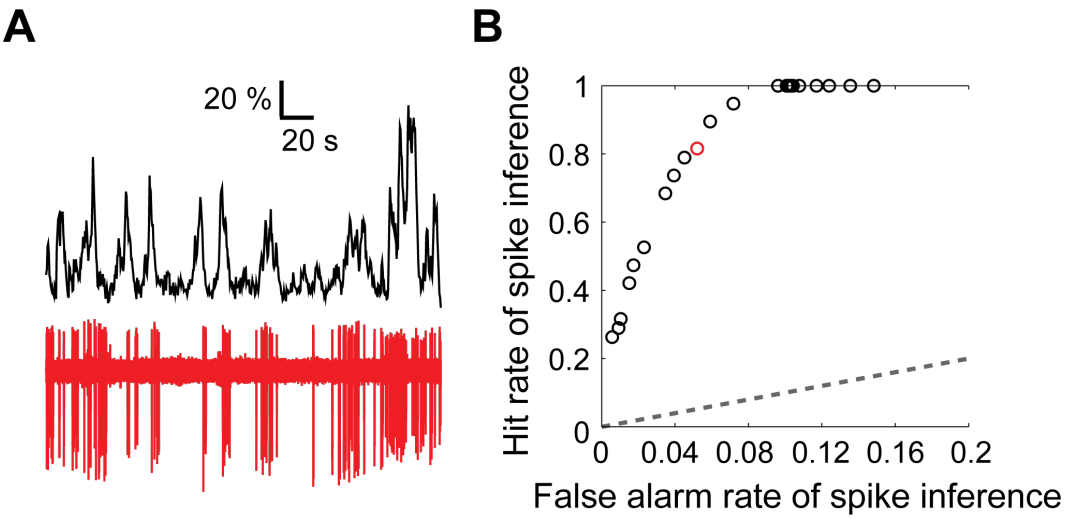

Figure 3.4 Calibration of inference with cell-attached recording

A, Simultaneously recorded calcium signals using GCaMP6s (black) and cell-attached recording signals (red). **B**, ROC of spiking event inference evaluated with cell-attached recording. Circles were plotted by changing threshold for inference (threshold = baseline + X ×1.4 × median absolute deviation). X = 4 was used as a threshold to balance true and false positive rates for operant conditioning (red circle).

I then performed simultaneous two-photon calcium imaging and cell-attached recording to calibrate the performance of the event inference (Fig3.4A). I inferred spiking events from calcium signals, and then analyzed how well inferred events actually matched action potentials. I calculated hit rate and false alarm rate of the spike inference, and estimated the performance using ROC curve (Fig3.4B). I chose *median of baseline + 4 × 1.4 × median absolute deviation of baseline* as the threshold to balance true and false positive rates for the inference. I used median absolute deviation (MAD) instead of standard deviation (SD) since MAD is more resilient to outliers in a data set than SD (Vogelstein et al., 2010). Applying lower threshold (*baseline + 2 × 1.4 × MAD*) produced inferred spiking signals showing correlation coefficient of 0.92 ± 0.02 (mean ± SD, n = 8) with spiking signals using the chosen threshold (*baseline + 4 × 1.4 × MAD*). Applying higher threshold (*baseline + 8 × 1.4 × MAD*) produced inferred spiking signals showing correlation coefficient of 0.15 ± 0.09 (mean ± SD, n = 8) with spiking signals using the chosen threshold.

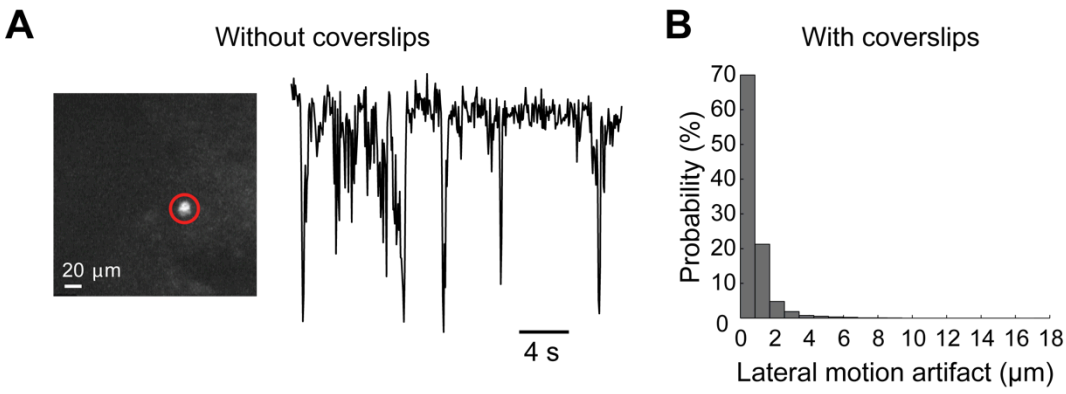

Figure 3.5 Motion artifacts during two-photon imaging

A, (left) A field of view containing a single GFP-expressing cell (red circle). The cranial window was made without coverslip stabilization of the brain surface. (right) Fluorescent intensity of GFP signal within ROI (red circle) in awake mouse. Rapid decreases of the signal indicate motion artifacts. **B,** Normalized histogram (probability) of lateral motion artifacts of calcium imaging in behaving mice. N = 35910 frames from 6 animals.

Since two-photon calcium imaging was performed in behaving animals, motion artifacts were expected to occur (Fig3.5A). Stabilizing brain surface with coverslips suppresses vertical motion artifacts well, but lateral motion artifacts usually need to be corrected (Dombeck et al., 2007; Komiyama et al., 2010). Although there have been several efforts to correct lateral motion artifact on-line (Paukert and Bergles, 2012; Chen et al., 2013a), I found lateral motion artifact in our setup to be negligible (Fig3.5B, N = 35910 frames from 6 animals) and did not perform on-line motion correction in order to maximize processing speed.

3.3 Discussion

3.3.1 Brief summary

In this chapter I have shown that on-line analysis of two-photon calcium imaging is possible. I developed a custom-written software to perform on-line analysis of imaging data (Fig3.1). I characterized the algorithm to infer spiking events from calcium signals (Fig3.2, Fig3.3), and then optimized the algorithm using electrophysiological recordings (Fig3.4). I also developed methods to stably observe neurons in behaving animals (Fig3.5). The methods allow us to perform operant conditioning by feeding inferred neuronal activity back to animals as rewards, and I would like to observe how neuronal population change their activity during the task.

3.3.2 Possible applications of on-line analysis of two-photon calcium imaging

On-line analysis of two-photon calcium imaging will be applied to operant conditioning experiments in the following chapters. But the methods have more potential applications in neuroscience.

With the coming development of imaging techniques, it will be very interesting to perform all-optical spike-timing dependent plasticity (STDP) experiment. That is, I could observe activity of upstream neurons with two-photon calcium imaging and activate downstream neurons with two-photon optogenetic stimulation within STDP time window (Markram et al., 1997; Bi and Poo, 1998; Izhikevich, 2006; Legenstein et al., 2008; Legenstein et al., 2010). Two-photon optogenetic

stimulation with single-cell resolution can be achieved using Channelrhodopsin-2 (ChR2) variant C1V1 (Packer et al., 2012; Prakash et al., 2012). It has recently been shown that one can perform all-optical experiment with simultaneously observing and stimulating neuronal activity at single-cell resolution in behaving animals as well (Packer et al., 2014; Rickgauer et al., 2014). It is still technically difficult to optically stimulate downstream neurons within ~20 ms (i.e., STDP time window) after the optically inferred spiking events of upstream neurons. However this issue can be solved by achieving fast enough optical recording and stimulation possibly with the development of engineering for microscopy and biophysics for optogenetics (Packer et al., 2013).

Although I did not correct motion artifacts using on-line image analysis, the methods could be beneficial in other kinds of experiments. The amount of motion artifacts I observed were negligible for observing cell bodies (~20 μm diameter), but will not be negligible for finer neuronal structure like dendritic spines (~1 μm diameter) (Nimchinsky et al., 2002). On-line motion correction of spines might be useful even for slice experiments since it is usually difficult to completely avoid the drift of slices over time, and precise coordinates of spines are crucial for two-photon stimulation of spines using caged-glutamate or ChR2 (Matsuzaki et al., 2001; Losonczy et al., 2008; Branco et al., 2010; Packer et al., 2012).

4 Multi-target optical operant conditioning of cortical activity

4.1 Introduction

Operant conditioning of neuronal activity has been done using several techniques and approaches (Fetz, 2007). Single-unit recording was originally used for operant conditioning by rewarding animals in response to the activity of a single neuron (Fetz, 1969; Fetz and Baker, 1973; Kobayashi et al., 2010). *In vivo* whole-cell recording was utilized to train animals based on subthreshold synaptic activity of single neurons (Ishikawa et al., 2014). Multi-unit recording was utilized to train neuronal populations. Koralek et al. performed multi-electrode recording and divided neuronal populations into two groups based on the location of electrodes, and then trained the rats/mice to differentiate the activity of two neuronal population (Koralek et al., 2012; Koralek et al., 2013). Sakurai & Takahashi performed on-line spike sorting with multi-unit recording, and trained animals based on synchronous activity of sorted neurons (Sakurai and Takahashi, 2012).

I was able to train neurons using various approaches since I observe activity of neuronal population at single-cell resolution using two-photon calcium imaging.

Here I firstly chose multiple neurons as targets and performed operant conditioning based on activity of these neuron.

4.2 Results

4.2.1 From on-line analysis of two-photon imaging to optical operant conditioning

I have developed on-line analysis of two-photon calcium imaging data in the previous chapter. I now would like to apply the methods to operant conditioning of cortical activity.

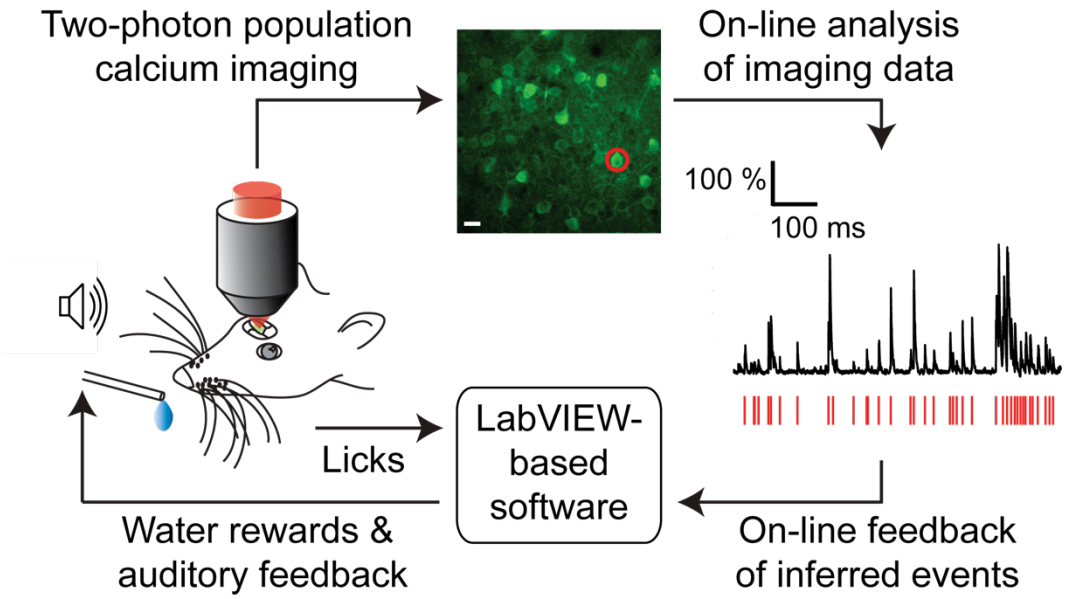

Figure 4.1 Experimental strategy for operant conditioning using on-line analysis of two-photon population calcium imaging

(Left) Schematic diagram of two-photon calcium imaging in awake, head-fixed mice. **(Top)** A two-photon image of neurons expressing GCaMP6s. Scale bar represents 20 μm. The red circle indicates a manually selected ROI from which **(Right)** calcium signals (black) were analyzed online to infer spiking events (red). **(Bottom)** Custom LabVIEW software receives inferred event signals and feeds it back to animals as water rewards and auditory feedback while recording lick signals.

I selected neurons for operant conditioning from the sample image and called them "target neurons", and other neurons "non-target neurons". Either one (next chapter) or four (this chapter) neurons were selected as target neurons in each session. On-line analysis of two-photon calcium imaging data was performed, and inferred spiking events were sent to another computer with a custom-written LabVIEW-based software as digital output. Water rewards (9 μl per event) and auditory feedback (14 kHz tone sound for 0.5 s) were delivered to animals via the LabVIEW-based software as soon as spiking events were inferred. The LabVIEW-based software also recorded licking behavior of mice with a lickometer (Fig4.1).

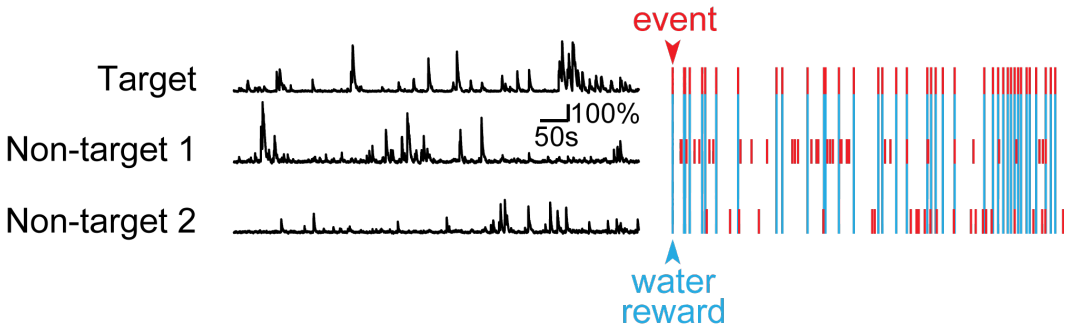

Figure 4.2 Schematic diagram of optical operant conditioning

Calcium signals (left, black) from three neurons (one target and two non-target), and inferred events (right, red). Water rewards (right, blue) were given in response to each inferred event in the target neuron.

I performed operant conditioning by giving water rewards based on activity of the target neurons, and also observed activity of target and non-target neurons during the task (Fig4.2).

4.2.2 Multi-target operant conditioning of cortical activity

I chose four neurons in layer 2/3 of whisker-related primary motor cortex to be target neurons for operant conditioning.

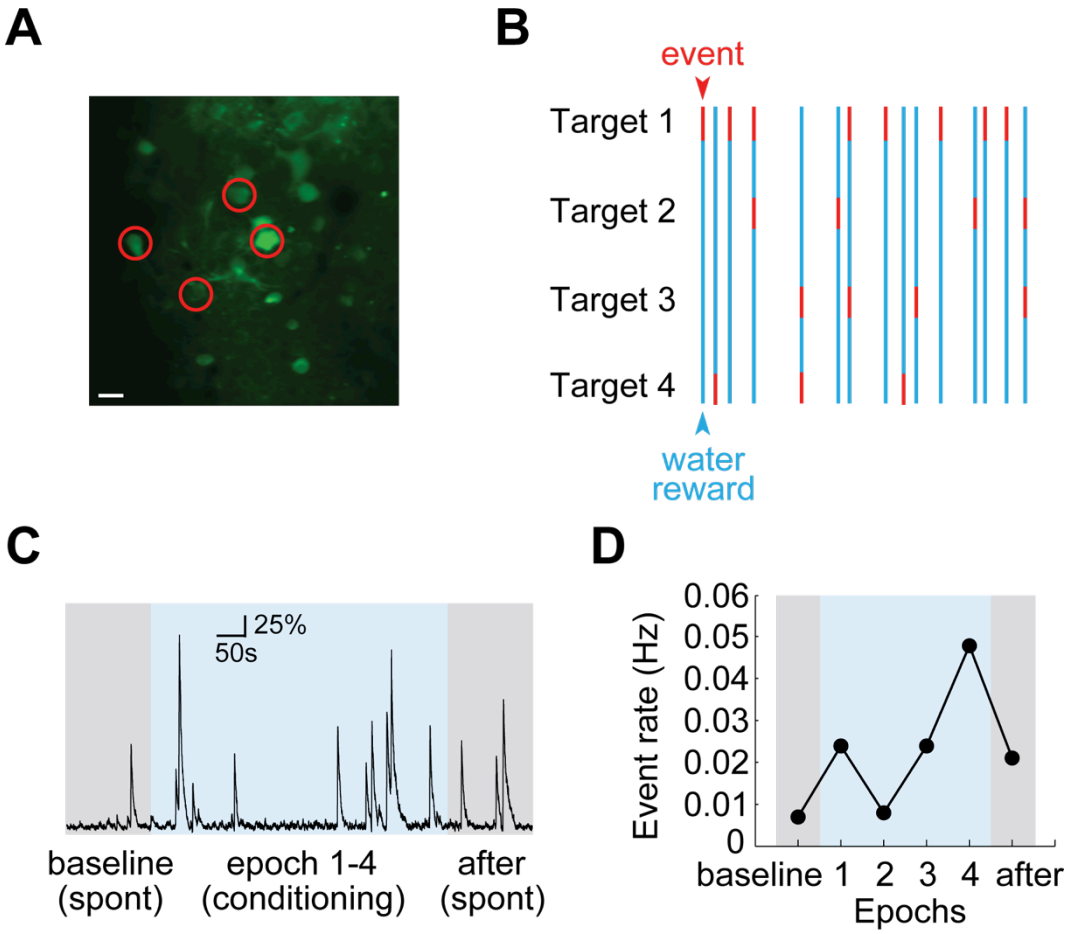

Figure 4.3 Optical operant conditioning with four target neurons

A, Neurons in motor cortex expressing GCaMP6s imaged *in vivo*, with four target neurons indicated (red circles). Scale bar represents 20 μm. **B**, Schematic diagram of the task. Water rewards (blue) were given if any of four target neurons showed spiking events (red). **C**, Calcium signals from one of the target neurons in **a**, showing baseline spontaneous activity ("baseline"), activity during conditioning ("epochs 1-4"), and spontaneous activity after the conditioning ("after"). **D**, Event rate change during the task inferred from the calcium signal in (C).

Rewards were given to animals in response to activity of any of four target neurons, i.e., in OR-gate manner (Fig4.3A, B). I decided to firstly choose four neurons to give animals water rewards enough frequently given low spiking event

rate with GCaMP6s calcium imaging. Calcium imaging was performed before, during, and after the conditioning period (Fig4.3C). Conditioning periods were chronologically segmented into four epochs for time course analysis, and event rates at each period were calculated as a measure of neuronal activity (Fig4.3D).

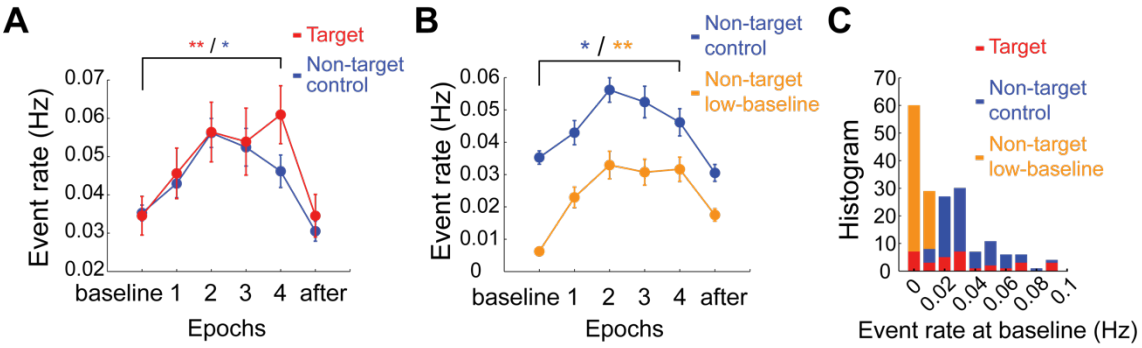

Figure 4.4 Event rate change during multi-target conditioning

A, Event rate change of target neurons (red) and non-target controls (blue) during conditioning. Wilcoxon signed-rank test between baseline and epoch 4; n = 32 and 75 neurons for target neurons and non-target neurons from 8 animals, respectively. **B**, Activity of non-target controls (blue, non-target neurons with top 50 percentile baseline activity) and non-target low-baseline (orange, the rest of non-target neurons) during four-target operant conditioning. The plot of non-target control (blue) is the same as the one in (A), and shown here for comparison. Wilcoxon signed-rank test between baseline and epoch 4, n = 75 neurons for both plots. **C**, Histogram of event rates at baseline in multi-target conditioning. N = 32, 75 and 75 neurons for target, non-target control and non-target low-baseline, respectively. Circles and error bars represent mean and SEM, respectively. Statistical significance was indicated as ** ($P < 0.01$) and * ($P < 0.05$).

Neurons with relatively high baseline activity were chosen as targets to enable mice to receive as many rewards as possible per training session to help associate target neuron activity and rewards. To compare targets and non-targets with approximately the same baseline activity, non-targets were classified into high-baseline "non-target control" and low-baseline "non-target low-baseline" (Fig4.4).

I analyzed how target and non-target neurons change activity during operant conditioning. I found that both target neurons and non-target controls increased their event rate when I compared periods before and at the end of learning, i.e., baseline and epoch 4 (Wilcoxon signed-rank test between baseline and epoch 4; n = 32 and 75 neurons for target neurons and non-target neurons from 8 animals, respectively. Fig4.4A). Non-target low-baseline population also increased their event rate when I compared periods before and at the end of learning (Wilcoxon signed-rank test between baseline and epoch 4, n = 75 neurons. Fig4.4B). There were 32 targets, 75 non-target controls, and 75 non-target low-baseline population in this experiment (Fig4.4C).

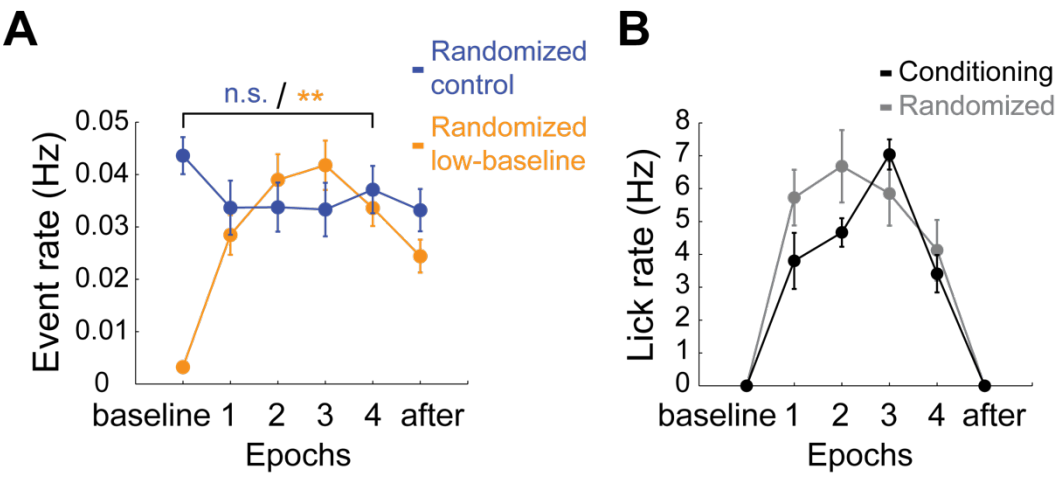

Figure 4.5 Control experiment with temporally randomized rewards

A, Activity of randomized controls (neurons with top 50 percentile baseline activity) and randomized low-baseline (the rest of neurons) during randomized water reward experiment. Wilcoxon signed-rank test between baseline and epoch 4, n = 39 neurons for both plots. **B**, Lick rate during multi-target operant conditioning (black, n = 8 animals) and randomized reward experiments (gray, n = 4 animals). Circles and error bars represent mean and SEM, respectively. Statistical significance was indicated as ** ($P < 0.01$), and n.s. ($P \geq 0.05$).

To confirm if the increased event rate resulted from learning, I performed control experiments in which mice were given water rewards with randomized intervals (but approximately at the same reward rate). To compare neurons in randomized experiments with target/non-target control in multi-target conditioning experiments (Fig4.4B) with approximately the same baseline activity, neurons were classified into high-baseline "randomized control" and low-baseline "randomized low-baseline" (N = 39 neurons for both population). No increase in event rate was observed from randomized control population during randomized reward experiments (Wilcoxon signed-rank test between baseline and epoch 4; n = 39 neurons. Fig4.5A). Randomized low-baseline population increased event rate during conditioning (Wilcoxon signed-rank test between baseline and epoch 4; n = 39 neurons. Fig4.5A), and this could be explained by the fact that mice conducted more licking behavior during conditioning period than baseline period (Fig4.5B).

Thus, mice could learn to increase neuronal activity during conditioning as opposed to randomized reward experiments. This learning did not occur only in

target neurons as mice increased activity across target and non-target neurons in a non-specific manner.

4.2.3 Results from different calcium indicator

In this thesis I used GCaMP6s (Chen et al., 2013b) as a calcium indicator otherwise mentioned, but I previously tried GCaMP5G (Akerboom et al., 2012) for optical operant conditioning before GCaMP6s became available.

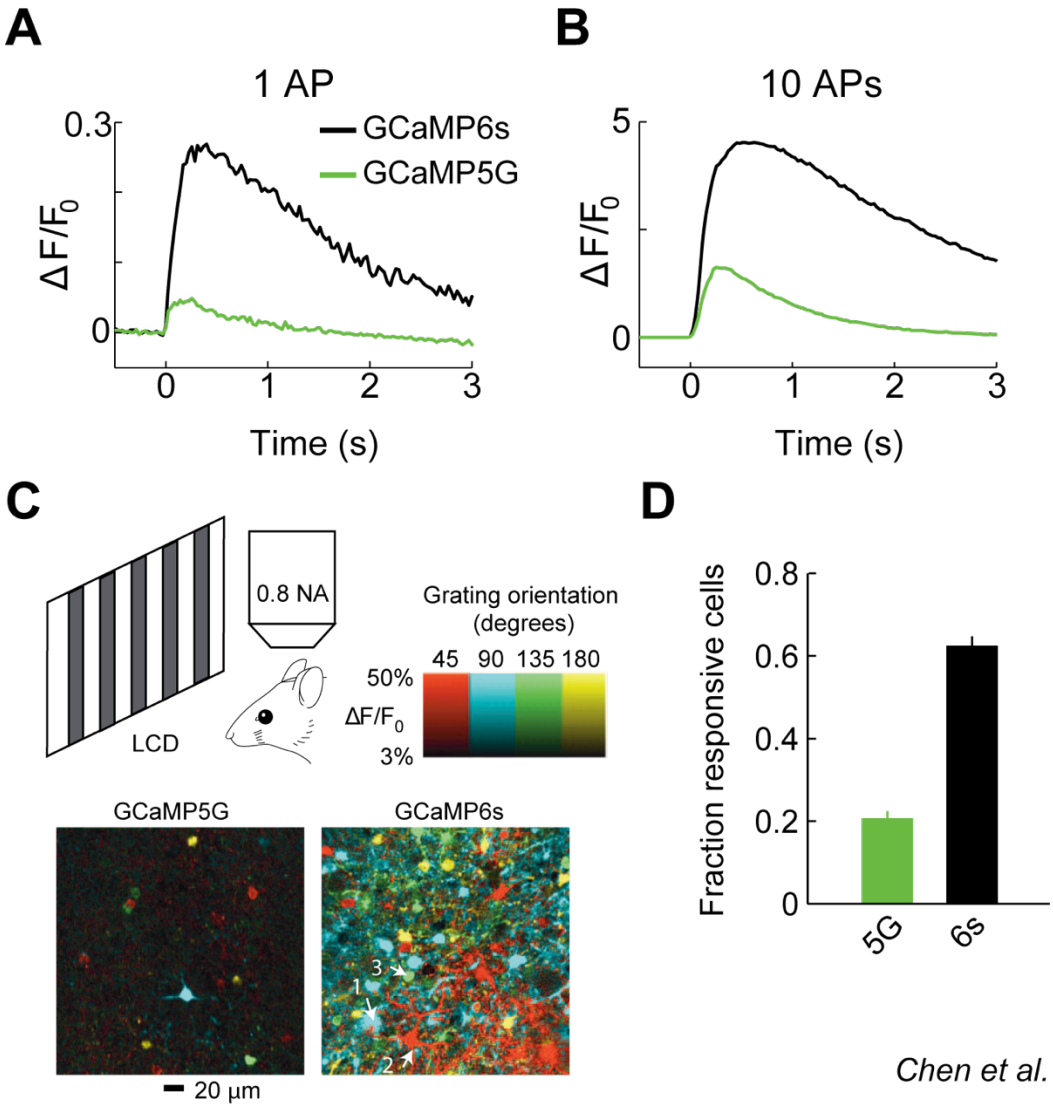

Figure 4.6 Comparisons of GCaMP6s and GCaMP5G for calcium imaging

A, Calcium signals evoked by single action potentials (APs) with GCaMP6s (black) and GCaMP5G (green). Calcium signals were defined as $\Delta F/F_0$ (= fluorescence increase from baseline signal divided by baseline signal). **B**, Calcium signals evoked by ten APs with GCaMP6s (black) and GCaMP5G (green). **C**, Two-photon calcium imaging in visual cortex with grating visual stimuli (top left) using GCaMP6s and GCaMP5G. Neurons responsive to specific orientation visual stimuli were described using pseudo color (top right) in each FOV (bottom two images). **D**, Fraction of neurons responsive to visual stimuli

using GCaMP5G (green) and GCaMP6s (black). All figures were adapted from Chen et al. (Chen et al., 2013b).

Two-photon calcium imaging with GCaMP6s gives us calcium signals with higher amplitudes (in $\Delta F/F0$, i.e., fluorescence increase from baseline signal divided by baseline signal) than with GCaMP5G (Fig4.6A, B). Imaging with GCaMP6s also gives us higher fraction of responsive cells to sensory stimuli than with GCaMP5G (Fig4.6C, D). These characteristics of GCaMP6s are supposed to be beneficial to perform optical operant conditioning.

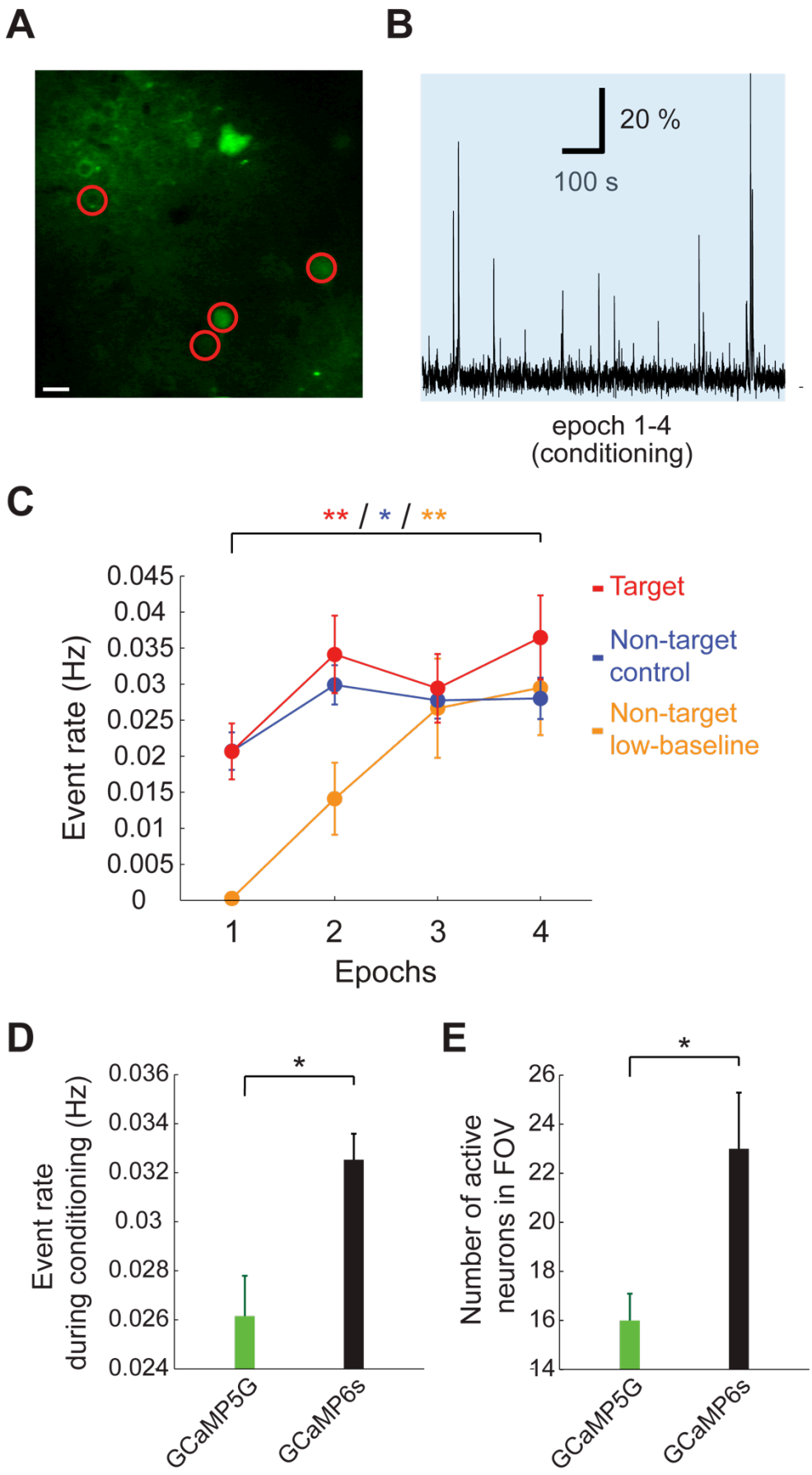
A
B
20 %
100 s
epoch 1-4
(conditioning)
C
** / * / **
Event rate (Hz)
0.045
0.04
0.035
0.03
0.025
0.02
0.015
0.01
0.005
0
1
2
3
4
Epochs
Target
Non-target
control
Non-target
low-baseline
D
Event rate
during conditioning (Hz)
0.036
0.034
0.032
0.03
0.028
0.026
0.024
*
GCaMP5G
GCaMP6s
E
Number of active
neurons in FOV
26
24
22
20
18
16
14
*
GCaMP5G
GCaMP6s

Figure 4.7 Optical operant conditioning with GCaMP5G imaging

A, Neurons in motor cortex expressing GCaMP5G imaged *in vivo*, with four target neurons indicated (red circles). Scale bar represents 20 μm. **B**, Calcium signals from one of the target neurons in (A), showing activity during conditioning ("epochs 1-4"). I did not perform two-photon calcium imaging before/after the conditioning period. **C**, Event rate change of targets (red), non-target controls (blue), and non-target low-baseline during conditioning. Wilcoxon signed-rank test between epoch 1 and epoch 4, n = 20, 48, 12 neurons for targets, non-target controls, and non-target low-baseline from 5 animals, respectively. **D**, Event rates of whole neuronal population during conditioning period using GCaMP5G (green) and GCaMP6s (black). Wilcoxon rank-sum test between, n = 80 and 405 neurons from 5 and 8 animals for GCaMP5G and GCaMP6s, respectively. **E**, Number of active neurons that showed spiking events during conditioning in the FOV. Wilcoxon rank-sum test between, n = 5 and 8 animals for GCaMP5G and GCaMP6s, respectively. Circles/columns and error bars represent mean and SEM, respectively. Statistical significance was indicated as ** ($P < 0.01$), and * ($P < 0.05$).

I performed operant conditioning with four target neurons as previously described (Fig4.3) using GCaMP5G (Fig4.7A-C). I did not observe calcium signals at baseline/after spontaneous period in the experiments with GCaMP5G. All target, non-target control, non-target low-baseline population increased their activity during operant conditioning with GCaMP5G when I compared event rate at epoch 1 and epoch 4 period (Wilcoxon signed-rank test between epoch 1 and epoch 4, n = 20 (target), 48 (non-target control), 12 (non-target low-baseline) neurons from 5 animals. Fig4.7C).

As expected from characteristics of GCaMP6s and GCaMP5G (Fig4.6), I detected inferred spiking events more often during operant conditioning with GCaMP6s

than GCaMP5G (Wilcoxon rank-sum test, n = 80 (GCaMP5G) and 405 (GCaMP6s) neurons. Fig4.7D). This means that I could reward animals more often in response to inferred events of target neurons with GCaMP6s than GCaMP5G. I also found more active neurons that showed spiking events during conditioning with GCaMP6s than GCaMP5G in the same size of FOV (Wilcoxon rank-sum test, n = 5 (GCaMP5G) and 8 (GCaMP6s) animals. Fig4.7E). In other words, I obtained more non-target neurons for analysis with GCaMP6s than GCaMP5G from the same size of FOV. These characteristics of GCaMP6s should have aided optical operant conditioning in the previously described experiments (Fig4.4).

4.3 Discussion

4.3.1 Brief summary

In this chapter I described application of on-line analysis of two-photon calcium imaging to operant conditioning of cortical activity, and results from multi-target operant conditioning. Operant conditioning of cortical activity using on-line analysis of two-photon calcium imaging was possible (Fig4.1, Fig4.2). I chose four neurons as target neurons, and trained animals in response to activity of target neurons with two-photon calcium imaging using GCaMP6s as calcium indicator (Fig4.3). I found that both targets and non-target controls increased their activity during the conditioning (Fig4.4). I performed control experiments in which mice were rewarded in a randomized manner, and no increase was

observed in a randomized control population (Fig4.5). Taken together, mice learned to increase activity of both target and non-target neurons in a non-specific manner. Similar results were observed when I performed multi-target operant conditioning using GCaMP5G as calcium indicator, though GCaMP5G gives us fewer spiking events and less active neurons than GCaMP6s (Fig4.6, Fig4.7).

4.3.2 Event rate change during conditioning and control experiments

In multi-target conditioning, both target and non-target neurons increased their activity during the task. In control experiments with randomized rewards, randomized control population did not increased their event rates whereas randomized low-baseline population increased their event rates during the task. These differences can be discussed in two aspects. Firstly, as mentioned in results section mice show licking behavior during conditioning whereas they don't at baseline/after spontaneous periods (Fig4.5B). I recorded from layer 2/3 neurons in whisker-related primary motor cortex in these experiments, and it has been shown that part of these neurons are responsible for licking behavior as well (Huber et al., 2012). I should note it is possible silent neurons at non-licking period (i.e., baseline/after spontaneous period) are tend to be licking-related neurons and supposed to be active during licking period (i.e., conditioning period). Secondly, the trend that low-baseline population increase activity in later periods (and high-baseline decrease activity in later periods) might partly be explained as a bias from how I defined two population. That is, highly active neuron at one period (at

baseline period in our definition) are statistically tend to decrease activity in other periods and vice versa, then activity of these two population are tend to be merged in other periods to some extent. It should be noted that increased activity during reward periods can possibly be related to auditory stimuli associated with rewards (Thompson and Sindberg, 1960).

4.3.3 Possible tasks for optical operant conditioning

I am able to train neurons in various approaches since I observe activity of neuronal population at single-cell resolution using two-photon calcium imaging. I could train animals based on activity of single neuron, multiple neurons, synchronous activity of neuronal population (Sakurai and Takahashi, 2012), differentiating activity of two neuronal population (Koralek et al., 2012), or activity patterns of neuronal population (e.g., some specific sequential activity in neuronal population (Fujisawa et al., 2008; Long et al., 2010; Harvey et al., 2012)).

In this chapter I did not choose specific neuron as GCaMP6s can be expressed in many subtypes of neurons under hSyn promoter. I could target specific neurons for operant conditioning. Specific subtypes of neurons (e.g., PV/SOM/VIP-positive interneurons) can be determined before the conditioning by molecular markers (Kawaguchi and Kubota, 1993; Kawaguchi and Kubota, 1998; Markram et al., 2004; Taniguchi et al., 2011; Gentet, 2012). Neurons can also be classified based on their functional characteristics in behavioral tasks: movement-related

neurons in motor cortex (Dombeck et al., 2009; Isomura et al., 2009; Huber et al., 2012; Hira et al., 2013), neurons with specific orientation tuning in visual cortex (Hubel and Wiesel, 1959; Ferster and Miller, 2000; Ohki et al., 2005; Ohki et al., 2006), place cells in hippocampus (O'Keefe and Dostrovsky, 1971; Eichenbaum et al., 1999), and so on.

5 Single-target optical operant conditioning of cortical activity

5.1 Introduction

Volitional control of neuronal activity for BMI studies has been investigated mostly by recording activity of neuronal populations (Chapin et al., 1999; Wessberg et al., 2000; Carmena et al., 2003; Carmena et al., 2005; Fetz, 2007; Moritz et al., 2008; Ganguly and Carmena, 2009; Cerf et al., 2010; Green and Kalaska, 2011; Moritz and Fetz, 2011; Shibata et al., 2011). Operant conditioning of neuronal activity, on the other hand, has been studied using single-unit recordings in various approaches (Fetz, 2007). The difference comes from the idea that it is often beneficial for BMI applications to have as many degrees of freedom as possible (i.e., as many neurons as possible), whereas neuronal operant conditioning often requires only one degree of freedom (i.e., a single target neuron) and many degrees of freedom (i.e., many target neurons) can possibly be confusing in this context.

Fetz originally gave rewards to primates in response to activity of single neuron in primary motor cortex observed with single-unit recording, and confirmed increase

in firing rate of the target neuron (Fetz, 1969; Fetz and Baker, 1973). Similar approaches have been applied to single neurons in PFC (Kobayashi et al., 2010) and hippocampus (Ishikawa et al., 2014). Here I performed operant conditioning of single neuron activity in primary motor cortex using two-photon calcium imaging, and observed how target and non-target neurons modify their activity during the task.

5.2 Results

5.2.1 Single-target operant conditioning of cortical activity

In the previous chapter I chose four neurons as targets for operant conditioning with acute two-photon calcium imaging in whisker-related primary motor cortex. In this chapter single neurons were chosen to be targets for operant conditioning with chronic two-photon calcium imaging in forelimb-related primary motor cortex.

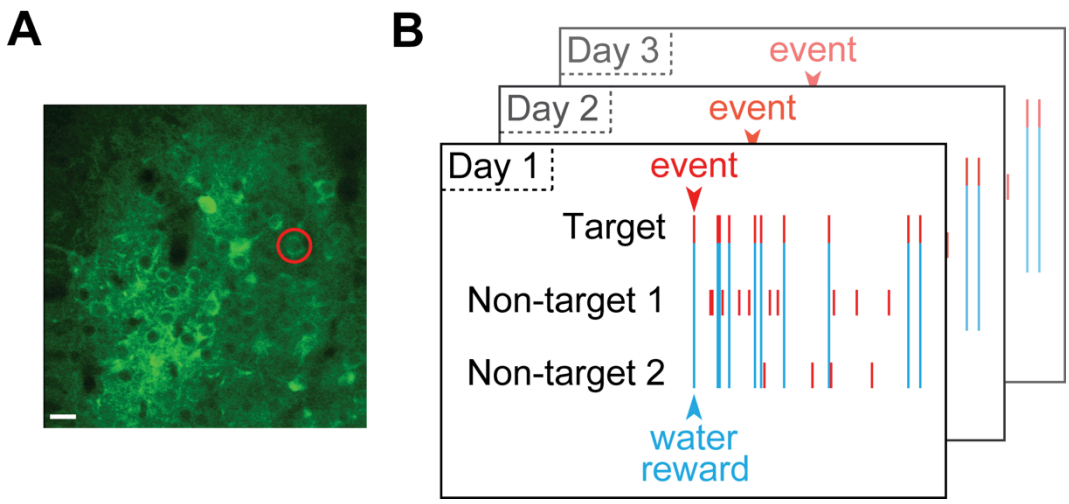

Figure 5.1 Optical operant conditioning with single target neurons over multiple days

A, Field of view of layer 2/3 neurons in motor cortex expressing GCaMP6s, with a single target neuron indicated (red circle). Scale bar represents 20 μm. **B**, Schematic diagram of the task. Water rewards (blue) were given if the single target neuron showed spiking events (red). Operant conditioning was repeated from the same target neurons for multiple days.

I performed operant conditioning in response to the activity of the same single target neuron and observed activity of the same sets of target/non-target neurons for multiple days (Fig5.1).

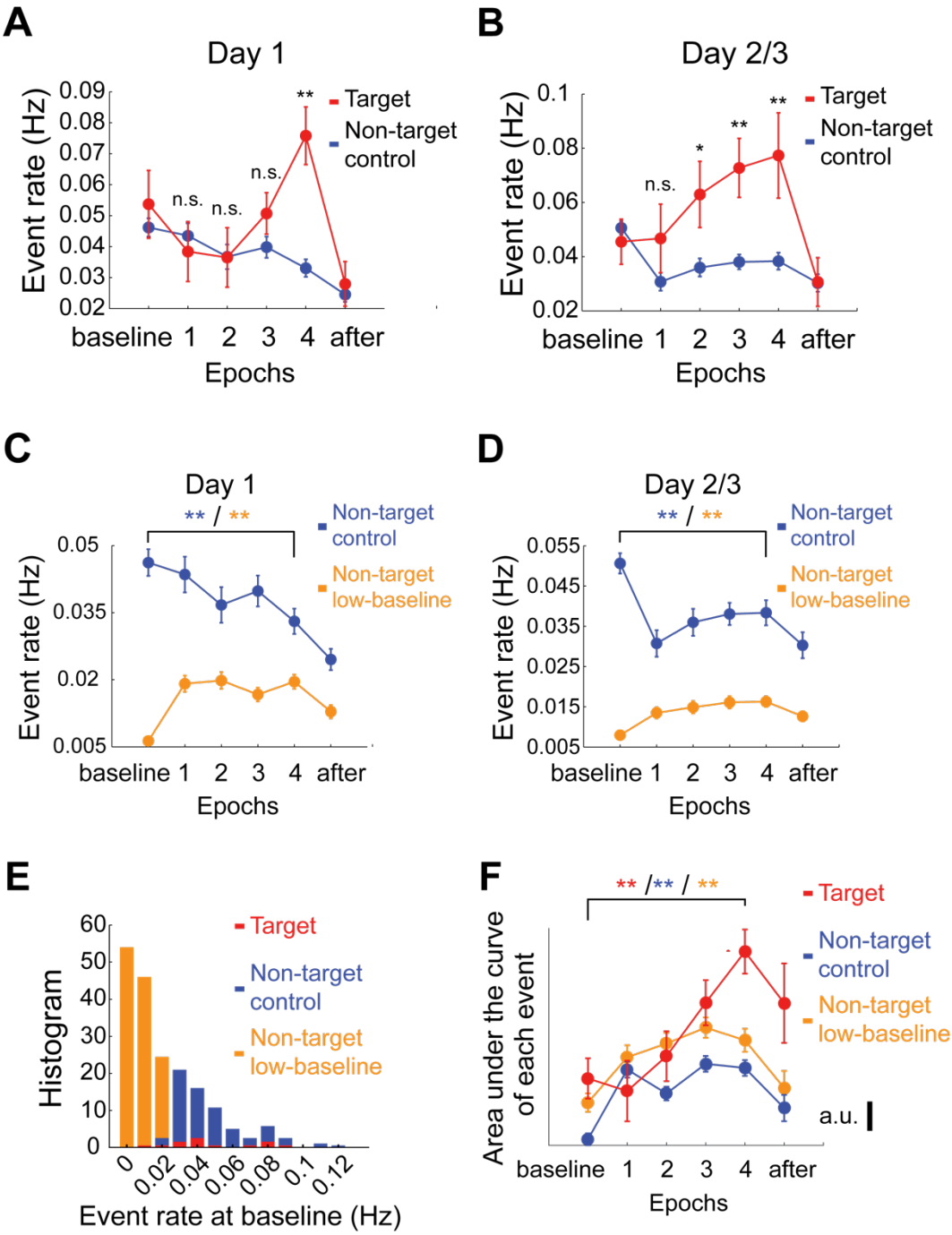

Figure 5.2 Event rate change during single-target conditioning

A, Event rate of target neurons (red) and non-target controls (blue) during conditioning on day 1. Wilcoxon rank-sum test with Bonferroni correction, n = 6 and 54 neurons for target and non-target control from 6 animals, respectively. **B**, Event rate of target neurons (red) and non-target controls (blue) during conditioning on day 2/3 (pooled from day 2 and day 3). Wilcoxon rank-sum test

with Bonferroni correction, n = 8 and 63 neurons for target and non-target control from 6 animals, respectively. **C**, Activity of non-target controls (blue, non-target neurons with top 33 percentile baseline activity) and non-target low-baseline (orange, the rest of non-target neurons) during single-target operant conditioning at day 1. The plots of non-target control (blue) are the same as the ones in (A). Wilcoxon signed-rank test between baseline and epoch 4, n = 54 and 110 neurons for non-target control and non-target low-baseline, respectively. Note that non-target controls significantly decreased their activity during conditioning. **D**, Activity of non-target controls (blue, non-target neurons with top 33 percentile baseline activity) and non-target low-baseline (orange, the rest of non-target neurons) during single-target operant conditioning at day 2/3. The plots of non-target control (blue) are the same as the ones in (B). Wilcoxon signed-rank test between baseline and epoch 4, n = 63 and 128 neurons for non-target control and non-target low-baseline, respectively. Note that non-target controls significantly decreased their activity during conditioning. **E**, Histogram of event rates at baseline in single-target conditioning. N = 14, 117 and 238 neurons for target, non-target control and non-target low-baseline, respectively. F, Area under the curve of each calcium event from target (red), non-target control (blue), non-target low-baseline (orange) during conditioning. Wilcoxon rank-sum test between baseline and epoch 4, n = 14 sessions from 6 animals. Circles and error bars represent mean and SEM, respectively. Statistical significance was indicated as ** ($P < 0.01$), * ($P < 0.05$), and n.s. ($P \geq 0.05$).

Here I found two changes in the activity of target neurons during chronic operant conditioning (Fig5.2). First, the target neurons specifically increased their event rate as opposed to non-target controls both on day 1 and day 2/3 (pooled from day 2 and 3) during conditioning (Wilcoxon rank-sum test with Bonferroni correction, n (target) = 6 (day 1) and 8 (day 2/3) neurons from 6 animals, n (non-target control) = 54 (day 1) and 63 (day 2/3) neurons from 6 animals. Fig5.2A, B). Second, the increase in activity of the target neurons emerged earlier within a

session on day 2/3 than on day 1 (increase in the activity was significant at epoch 4 at day 1, whereas increase in the activity was significant from epoch 2 at day 2/3. Fig5.2A, B). Non-target low-baseline population also increased activity during the conditioning (Wilcoxon signed-rank test between baseline and epoch 4, n (non-target control) = 54 (day 1) and 63 (day 2/3) neurons, n (non-target low-baseline) = 110 (day 1) and 128 (day 2/3) neurons. Fig5.2C, D), but this trend had been discussed in the previous chapter (chapter 4.3.2) and will be discussed further in this chapter. There were 14 targets, 117 non-target controls, and 238 non-target low-baseline populations in this experiment (Fig5.2E). The area under the curve of each calcium event, which reflects the number of spikes in each event (Chen et al., 2013b), increased in all target, non-target control, non-target low-baseline neurons during conditioning (Wilcoxon rank-sum test between baseline and epoch 4, n = 14 sessions from 6 animals. Fig5.2F).

Thus, these results indicate that mice can learn to increase activity of single target neurons in a specific manner during operant conditioning, and also subsequently learn to increase their activity earlier within a session over multiple days.

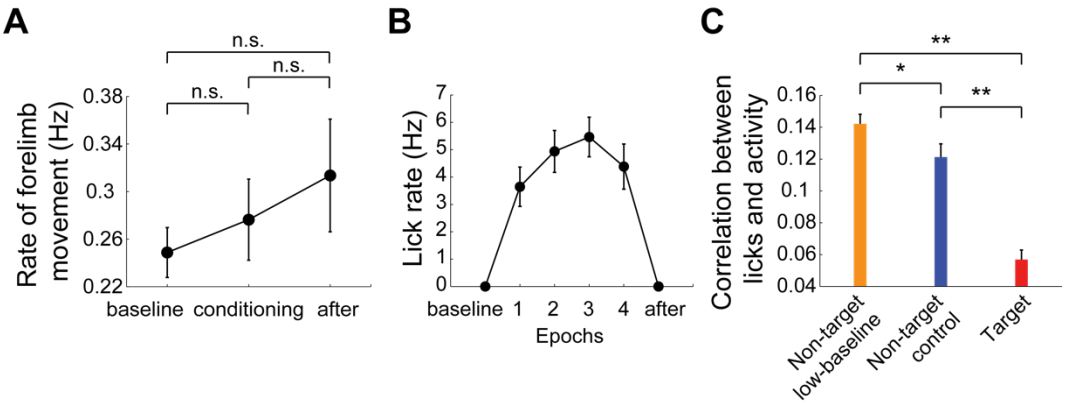

Figure 5.3 Behaviors during single-target conditioning

A, Rate of forelimb movement detected from movies during single-target operant conditioning. Wilcoxon signed-rank test without correction, n = 7 sessions. **B**, Lick rate during single-target operant conditioning (n = 6 animals). **C**, Correlation between licks and neuronal activity calculated from coefficients of GLM fitting during single-target operant conditioning. Wilcoxon rank-sum test with Bonferroni correction, n = 238 and 117 and 14 neurons for non-target low-baseline and non-target control and target, respectively. Note that non-target low-baseline showed significantly higher correlation with licks, and both their activity (Fig5.2B, C) and lick rate (B) increase during conditioning period. Circles/columns and error bars represent mean and SEM, respectively. Statistical significance was indicated as ** ($P < 0.01$), * ($P < 0.05$), and n.s. ($P \geq 0.05$).

The target neurons were located in the forelimb-related region of motor cortex, so it could be argued that increased activity during conditioning were related with increased forelimb movements during the task. I analyzed forelimb movements during the task from recorded movies, and there were no difference in forelimb movements between before, during, and after the conditioning period (Wilcoxon signed-rank test without correction, n = 7 sessions. Fig5.3A). I also argued that increase in the activity of non-target low-baseline population could be related to licking behavior (chapter 4.3.2, Fig5.2C, D, Fig5.3B). I analyzed correlations between neuronal activity and licking behavior with generalized linear model (GLM), and I found that non-target low baseline showed higher correlation with licking than non-target controls and targets (Wilcoxon rank-sum test with Bonferroni correction, n = 238 and 117 and 14 neurons for non-target low-baseline and non-target control and target, respectively. Fig5.3C). This result supports the idea that the increase in the activity of low-baseline population

during operant conditioning can partly be explained by their contribution to licking behavior.

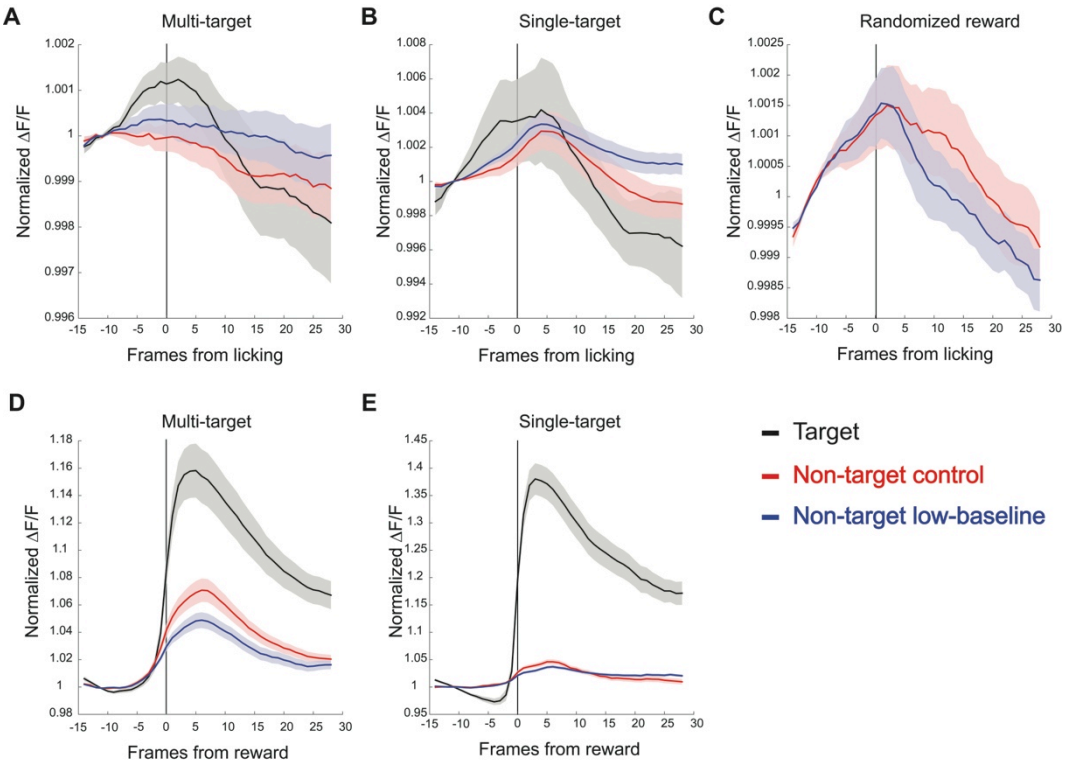

Figure 5.4 Event-triggered averages of calcium signals

A, Lick-triggered averages of calcium signals (ΔF/F) of target (black), non-target control (red), and non-target low-baseline (blue) neurons in multi-target conditioning. Signals were acquired at 7 Hz, and normalized with the mean of first 7 frames (-15 to -8 frames from licking). Shades represent SEM (n = 32, 75 and 75 neurons for target, non-target control and non-target low-baseline, respectively). **B**, Lick-triggered averages of calcium signals (ΔF/F) of target (black), non-target control (red), and non-target low-baseline (blue) neurons in single-target conditioning. Shades represent SEM (n = 14, 117 and 238 neurons for target, non-target control and non-target low-baseline, respectively). **C**, Lick-triggered averages of calcium signals (ΔF/F) of randomized control (red), and randomized low-baseline (blue) neurons in randomized reward experiment. Shades represent SEM (n = 39 neurons for both population). **D**, Reward-

triggered averages of calcium signals (ΔF/F) of target (black), non-target control (red), and non-target low-baseline (blue) neurons in multi-target conditioning. Shades represent SEM (n = 32, 75 and 75 neurons for target, non-target control and non-target low-baseline, respectively). **E**, Reward-triggered averages of calcium signals (ΔF/F) of target (black), non-target control (red), and non-target low-baseline (blue) neurons in single-target conditioning. Shades represent SEM (n = 14, 117 and 238 neurons for target, non-target control and non-target low-baseline, respectively).

I also analyzed event-triggered (either by licking or reward) averages of calcium signals (ΔF/F) to confirm if non-target low-baseline population is more strongly contributed to licking behavior (Fig5.4). However, lick-triggered averages of calcium signals from non-target control and non-target low-baseline population were not difference at the timing of licking ($P>0.05$, Wilcoxon rank-sum test) against the result from GLM analysis (Fig5.4A,B, Fig5.3C).

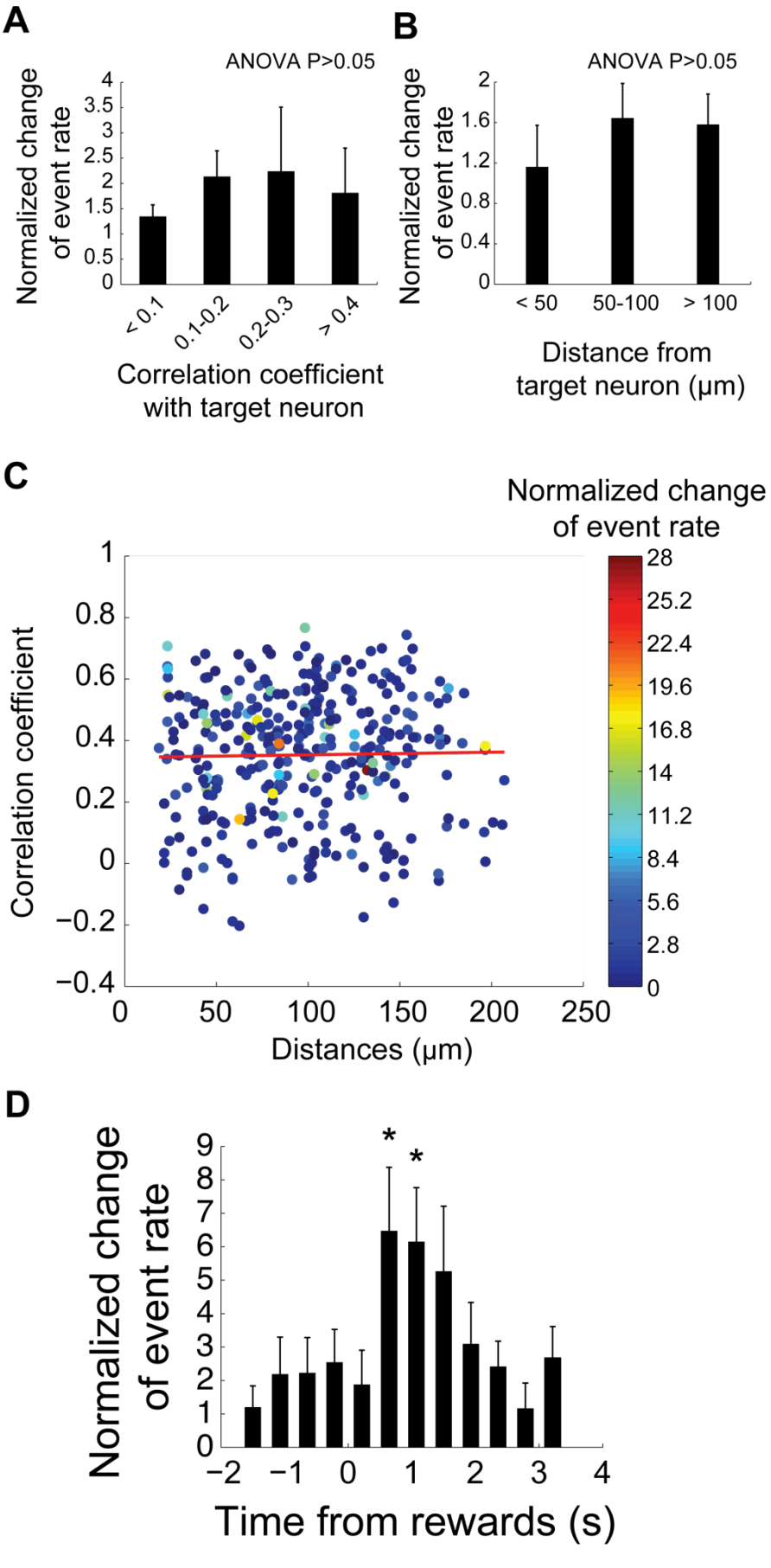
A
ANOVA P>0.05
Normalized change of event rate
Correlation coefficient with target neuron
< 0.1
0.1-0.2
0.2-0.3
> 0.4
B
ANOVA P>0.05
Normalized change of event rate
< 50
50-100
> 100
Distance from target neuron (μm)
C
Normalized change of event rate
Correlation coefficient
Distances (μm)
D
Normalized change of event rate
Time from rewards (s)

Figure 5.5 Effects of the relationships between target and non-target neurons

A, Correlation coefficient between non-target and target neurons (x-axis) had no correlation with activity change of non-target neurons during conditioning (y-axis). ANOVA P>0.05, n = 255 and 64 and 15 and 21 neurons for < 0.1 and 0.1-0.2 and 0.2-0.3 and > 0.4, respectively. **B**, Distance between non-target and target neurons (x-axis) had no correlation with activity change of non-target neurons during conditioning (y-axis). ANOVA P>0.05, n = 65 and 121 and 173 neurons for < 50 μm and 50-100 μm and > 100 μm, respectively. **C,** Scatter plot of correlation coefficient and distance with showing normalized event rate with pseudo color. Linear regression was performed between correlation coefficient and distance ($y = (8.44\times10^{-5}) x + 0.35$, $R^2 = 3.17\times10^{-4}$). **D**, Activity change of non-target neurons (y-axis) that showed top 5-percentile spiking event numbers in each time bins (x-axis, see Methods). Student's t-test between each bin and zero with Bonferroni correction, n = 18 neurons in all bins. ANOVA P<0.05. Note that non-target neurons that were most active around 0.4-1.2 s after water rewards showed significant increase of activity, implying that those neurons were responsible for licking behavior. Columns and error bars represent mean and SEM, respectively. Statistical significance was indicated as * (P < 0.05).

Since I expected to observe subsets of non-target neurons that increase activity together with target neurons, I analyzed how the relationships between target and non-target neurons correlate with the increase in the activity of non-target neurons. Firstly I focused on correlation between neurons. Correlation in neuronal activity has been investigated as a key feature in neural circuits (Shadlen and Newsome, 1998; Averbeck and Lee, 2004; Averbeck et al., 2006; Cohen and Maunsell, 2009; Mitchell et al., 2009; Jeanne et al., 2013), and it has been shown that neuronal pairs with high correlation tend to connect to each other (Ko et al., 2011). I classified non-target neurons based on Pearson's correlation coefficients

between target and non-target neurons, and there were no significant correlations between the coefficients and the increase in the activity (ANOVA $P>0.05$, n = 255 and 64 and 15 and 21 neurons for < 0.1 and 0.1-0.2 and 0.2-0.3 and > 0.4, respectively. Fig5.5A). Secondly I focused on geometrical distances between neurons, since it has been shown that neurons nearby tend to change their dynamics together during the task (Komiyama et al., 2010). I classified non-target neurons based on distances to target neurons, and there were no correlation between the distances and the increase in the activity (ANOVA $P>0.05$, n = 65 and 121 and 173 neurons for < 50 μm and 50-100 μm and > 100 μm, respectively. Fig5.5B). These two analyses was combined as scatter plot to visualize the relationships between correlation coefficient, distances, and normalized change of event rate (Fig5.5C). Lastly I focused on the timing of reward to animals. The relationship between reward and STDP has been discussed by researchers (Izhikevich, 2006; Legenstein et al., 2008; Legenstein et al., 2010), and it has been shown that reward can affect the dynamics of STDP (Cassenaer and Laurent, 2012). I classified non-target neurons based on how active they are at each timing from the reward onset, and non-target neurons that were most active from 0.4 to 1.2 s after the reward significantly showed more increase in their activity during conditioning (Student's t-test between each bin and zero with Bonferroni correction, n = 18 neurons in all bins. ANOVA $P<0.05$. Fig5.5D). However the period from 0.4 to 1.2 s after the reward is the period mice lick water rewards, so the increase in the activity will be explained by licking behavior (Fig5.3B, C, Fig5.5D).

Taken together, I found no correlation between activity changes in non-target neurons and correlation coefficients, distances, or spike times from rewards (Fig5.5).

5.2.2 Comparison of multi-target and single-target operant conditioning

In the previous chapter I showed the results from multi-target operant conditioning, and in this chapter I showed the results from single-target operant conditioning.

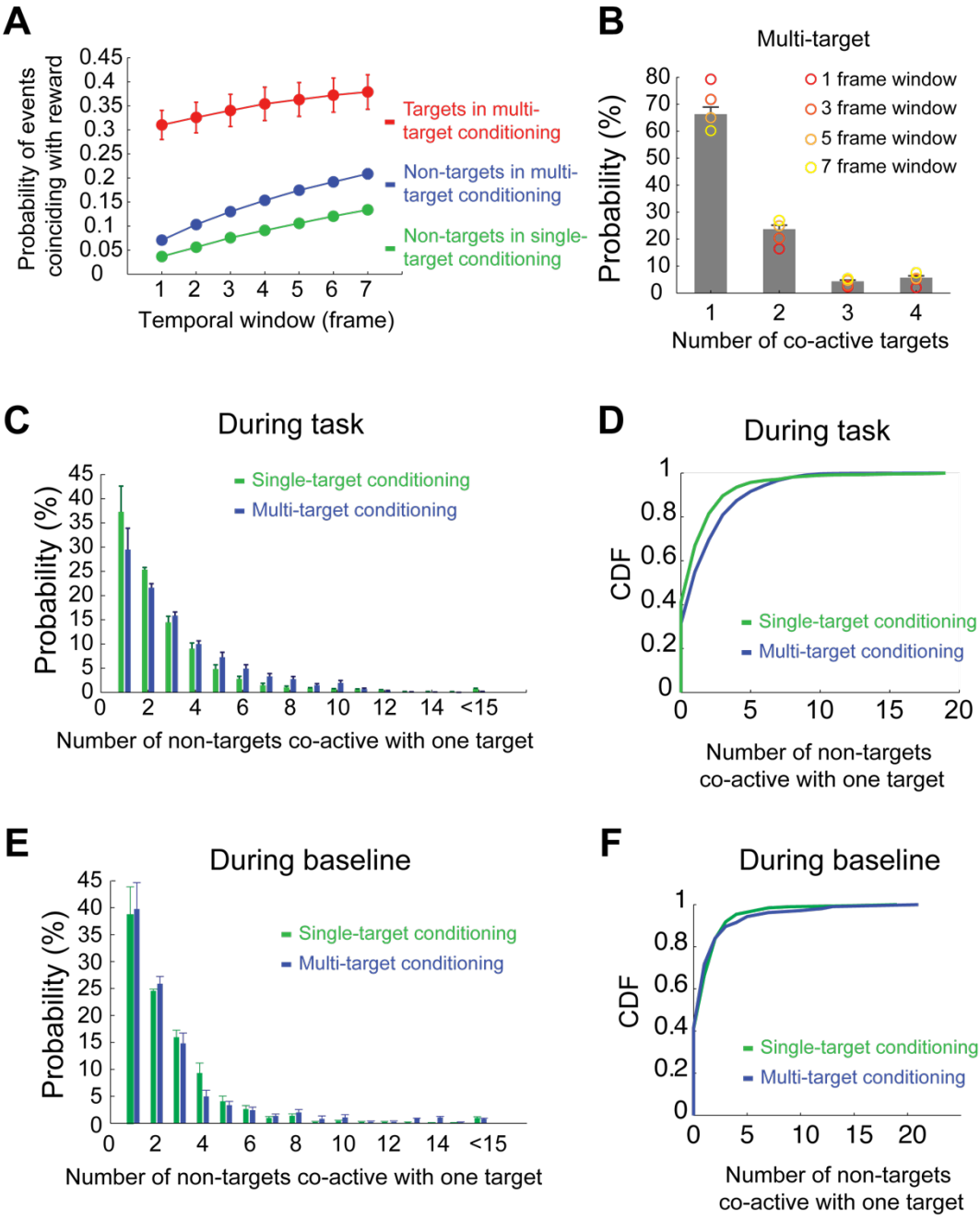

Figure 5.6 Probability of coincidence between neuronal activities and reward

A, Probability of neuronal events coinciding with water reward in multi-target conditioning (target and non-target neurons indicated in red and blue, respectively) and single-target conditioning (non-target neurons indicated in green). Probability of target neuron's events coinciding with reward in single-target conditioning equal to one. Coincidence of events and reward is defined

using temporal windows (± X frames from water reward, X = 1 to 7, image acquisition at 7 Hz). N = 32, 150 and 355 neurons for red, blue and green plots, respectively. **B**, Probability of the number of co-active target neurons in multi-target conditioning. Coincidence of neuronal activity of targets is defined using temporal windows (± X frames from events of one target neuron, X = 1,3, 5, and 7). Columns and error bars represent mean and SEM, n = 4 width of temporal windows (32 neurons in 8 sessions). **C**, Probability of the number of non-target neurons co-active with one target neuron in single-target and multi-target conditioning during task. Coincidence of neuronal activity of one target and non-targets is defined using temporal windows (± X frames from events of one target neuron, X = 1 to 7). Columns and error bars represent mean and SEM, n = 7 width of temporal windows (14 target and 355 non-target neurons in 14 sessions for single-target conditioning. 32 target and 152 non-target neurons in 8 sessions for multi-target conditioning.). **D**, Cumulative distribution function (CDF) of the histogram in (C) obtained with 3 frame window during task. Note that non-target neurons in multi-target conditioning were more co-active with target than in single-target conditioning ($P < 10^{-7}$, two-sample Kolmogorov-Smirnov test, $P < 10^{-11}$, Wilcoxon rank-sum test, data obtained with 3 frame window). Circles/columns and error bars represent mean and SEM, respectively. **E**, Probability of the number of non-target neurons co-active with one target neuron in single-target and multi-target conditioning during baseline. Coincidence of neuronal activity of one target and non-targets is defined using temporal windows (± X frames from events of one target neuron, X = 1 to 7). Columns and error bars represent mean and SEM, n = 7 width of temporal windows (14 target and 355 non-target neurons in 14 sessions for single-target conditioning. 32 target and 152 non-target neurons in 8 sessions for multi-target conditioning.). **F**, CDF of the histogram in (E) obtained with 3 frame window during baseline. Note that co-activity was not significantly different between multi-target conditioning and single-target conditioning ($P > 0.05$, two-sample Kolmogorov-Smirnov test, data obtained with 3 frame window). Circles/columns and error bars represent mean and SEM, respectively.

In multi-target conditioning, the learning did not occur only in target neurons as mice increased activity across target and non-target neurons in a non-specific manner (Fig4.4, Fig4.5). In single-target conditioning, on the other hand, mice learned to specifically increase activity of target neurons during conditioning (Fig5.2). These results imply that it might be unclear to the mouse which neuron's activity was rewarded during operant conditioning with four target neurons, whereas it was clearer in single-target conditioning.

I analyzed coincidental spiking/reward events in multi-target and single-target conditioning experiments. As for coincidental events between spikes and rewards, I analyzed how often these events coincide with using several temporal windows (Fig5.6A). The target neurons in single-target conditioning were omitted in Fig5.6A since they always coincide with rewards. I also analyzed how many target neurons are co-active in multi-target conditioning with using several temporal windows (Fig5.6B). Only one of target neurons was often active (~66 %), but target neurons were otherwise co-active. As for coincidental events between target and non-target neurons, I analyzed how many non-target neurons were co-active with one target neuron in multi-target and single-target conditioning during task (Fig5.6C, D). When I compared cumulative density function (CDF), more non-target neurons tended to be co-active with one target neuron in multi-target conditioning than in single-target conditioning ($P < 10^{-7}$, two-sample Kolmogorov-Smirnov test, $P < 10^{-11}$, Wilcoxon rank-sum test, data obtained with 3 frame window. Fig5.6D). This difference was not observed when the same analysis was applied to baseline period (Fig5.6E, F), implying that

stronger co-activity between target and non-target neurons during multi-target conditioning was resulted from the task.

Taken together, this analysis showed that target and non-target neurons are often active at the same time during multi-target conditioning than in single-target conditioning. This result supports the idea that it might be unclear to the mouse which neuron's activity was rewarded during operant conditioning with four target neurons.

5.3 Discussion

5.3.1 Brief summary

In this chapter I described how neurons change their activity during single-target optical operant conditioning. I chose single neurons as target neuron and performed operant conditioning for multiple days with chronic two-photon calcium imaging (Fig5.1). I found that mice could learn to increase activity of single target neurons in a specific manner without increasing activity of non-target control neurons during operant conditioning. I also observed that mice subsequently learn to increase activity of target neurons earlier within a session over multiple days (Fig5.2). Forelimb movements cannot simply explain the increase in the activity of target neurons since there was no significant difference in forelimb movements between before, during, and after the conditioning period (Fig5.3A). Increase in the activity of non-target low-baseline neurons can partly be explained by their contribution to licking behavior (Fig5.3B, C). I found no

correlation between activity changes in non-target neuron and correlation coefficients, geometrical distances, or spike times from water rewards (Fig5.5). I compared results between multi-target operant conditioning and single-target operant conditioning, and found that non-target neurons were more co-active with rewards/target neurons during multi-target conditioning than single-target conditioning (Fig5.6).

5.3.2 Event rate change during single-target and multi-target operant conditioning

I demonstrated that single layer 2/3 neurons could be trained with operant conditioning, in the absence of significant increases in activity in their local neighbors (Fig5.2A, B). Non-target neurons in the FOV did not correlate their activity change with their relationships to target neurons (Fig5.5), although I expected to observe subsets of non-target neurons, which are somehow related to target neurons, increase their activity together with target neurons. These results suggest that neuronal assemblies (Hebb, 1949; Harris et al., 2003; Buzsáki, 2010) generated by operant conditioning can be highly sparse (at least as sparse as our FOV, 250 × 250 μm). The 'priming' of operant conditioning of single neurons on subsequent days following the first day of training demonstrates that 'savings' observed with repeated behavioral plasticity episodes (Medina et al., 2001; Malone et al., 2011) can also occur on the single-cell level.

Mice increased neuronal activity in a non-specific manner during multi-target conditioning, whereas they increased activity of target neurons in a specific manner during single-target conditioning. Non-target neurons were more co-active with rewards/target neurons during multi-target conditioning than single-target conditioning (Fig5.6). This could explain why animals increased neuronal activity in a non-specific manner during multi-target conditioning. It could be argued that a global increase of activity is a worthwhile strategy in multi-target conditioning, whereas the resulting reward does not justify the effort of increasing all neurons when only one neuron is rewarded. Animals might calculate costs for increasing neuronal activity, and it could be possible to model cost function to study the dynamics.

It should also be noted that there was a difference between multi-target and single-target conditioning in the way of performing surgeries (Chapter 2.1). In multi-target conditioning, the experiment was acute and a craniotomy was opened on the day of conditioning. On the other hand, in single-target conditioning the experiment was chronic and a craniotomy was opened more than a week before the conditioning. This also means that animals might have been affected by isoflurane during the task even though animals were recovered from anesthesia in multi-target conditioning experiments.

5.3.3 Comparison with past works, and similar works recently published

This experiment is inspired by the work by Fetz demonstrating that single neuron can be trained to increase its activity during operant conditioning using single-unit recording in primates (Fetz, 1969). My results agree with Fetz's paper in that target neurons increase activity during operant conditioning, but time course of learning is different. In Fetz's experiment monkey learned to increase single-unit activity within several minutes (Fig1.4A), whereas mice took approximately 15 minutes to learn to increase event rate of calcium signals (Fig5.2A). The difference could be derived from difference in species of subjects or SNR/temporal resolution of recording techniques, resulting in huge difference in the observed rate of neuronal activity. The firing rate was at tens of Hz in electrophysiological recording at layer 5 of motor cortex with primates, whereas the inferred event rate was below 1 Hz in two-photon calcium imaging at layer 2/3 of motor cortex with rodents. The advantage of two-photon calcium imaging comparing to single-unit recording for operant conditioning is to be able to observe activity of neighboring neuronal population (Fig4.4, Fig5.2). It is also an advantage to use two-photon calcium imaging to observe identified local circuits over multiple days (Fig5.2).

There have been similar works recently published describing operant conditioning of cortical activity using two-photon calcium imaging (Clancy et al., 2014; Hira et al., 2014). Clancy et al. chose two groups of neuronal population, and rewarded mice in response to the difference of the activity of two groups. Mice learned to differentiate the activity in approximately 10 minutes, and they found that learning was accompanied by modifications of firing correlations in spatially localized networks. Hira et al. performed almost the same experiments as my

single-target operant conditioning, and mice learned to increase the activity of target neurons in approximately 15 minutes. They showed that increase/decrease in the activity of non-target neurons depends on their timing of active moments compared to reward timing, although this is not confirmed in my data (Fig5.5). Time course of learning described in these two papers agrees with my results (Fig5.2), and together show that mice can quickly learn to volitionally control neuronal activity.

6 Optical operant conditioning of dendritic activity

6.1 Introduction

Neurons receive synaptic inputs onto dendrites, and then the inputs are integrated and transformed to APs as outputs (London and Häusser, 2005; Stuart et al., 2007). It has been argued that single dendrites perform local computation as a functional unit to transform inputs to dendritic spikes, and outputs from these local units are subsequently integrated at soma for transforming inputs to AP outputs (Poirazi et al., 2003; Losonczy and Magee, 2006; Losonczy et al., 2008; Makara et al., 2009; Branco et al., 2010; Branco and Häusser, 2010; Govindarajan et al., 2011).

To understand the role of local computation in dendrites it is important to record dendritic activity *in vivo*. There have been several attempts to perform *in vivo* whole-cell recording from dendrites (Helmchen et al., 1999; Smith et al., 2013), but this experiment is technically demanding and low-yield. Two-photon calcium imaging enables us to record dendritic activity *in vivo* (Jia et al., 2010; Chen et al.,

2011; Chen et al., 2013b; Hill et al., 2013; Palmer et al., 2014) even from behaving animals (Xu et al., 2012a; Sheffield and Dombeck, 2014).

Dendritic activity can be triggered not only by synaptic inputs/dendritic spikes, but also by back-propagating APs (bAPs) originating from cell bodies (Hausser et al., 2000; Waters, 2004). It has been reported that these two sources of dendritic activity (i.e., local dendritic spikes and bAPs) can be separated by their kinetics of the voltage onset when using *in vivo* dendritic whole-cell recordings (Smith et al., 2013), but not with two-photon calcium imaging of dendrites (Sheffield and Dombeck, 2014).

If I can capture local dendritic activity, an interesting experiment to perform would be to differentiate local activity of two dendritic branches of the same cell. This is aimed to tackle the hypothesis that dendrites can work as a functional unit for processing information (Chapter 1.5). If two dendrites process two independent information, local activity of these dendrites can be differentiated with operant conditioning (i.e., training animal based on the difference of the activity of two dendrites).

Here I firstly developed methods to perform operant conditioning of dendritic activity using two-photon calcium imaging. I observed increase in the dendritic activity during operant conditioning as I observed in previous chapters with somatic calcium imaging. I then developed three-dimensional (3D) two-photon calcium imaging to simultaneously record activity of dendrites and soma, in the hope of separating dendritic calcium signals derived from dendritic spikes and the ones derived from bAPs.

6.2 Results

6.2.1 Operant conditioning of dendritic activity with two-photon calcium imaging

Conventional AAV injection used in previous chapters yields dense expression of GCaMP6s. This is desirable for performing two-photon calcium imaging from cell bodies, but it is difficult to separate the neuronal identity of dendrites (i.e., to identify which dendrite is coming from which neuron) when I perform two-photon calcium imaging from dendrites.

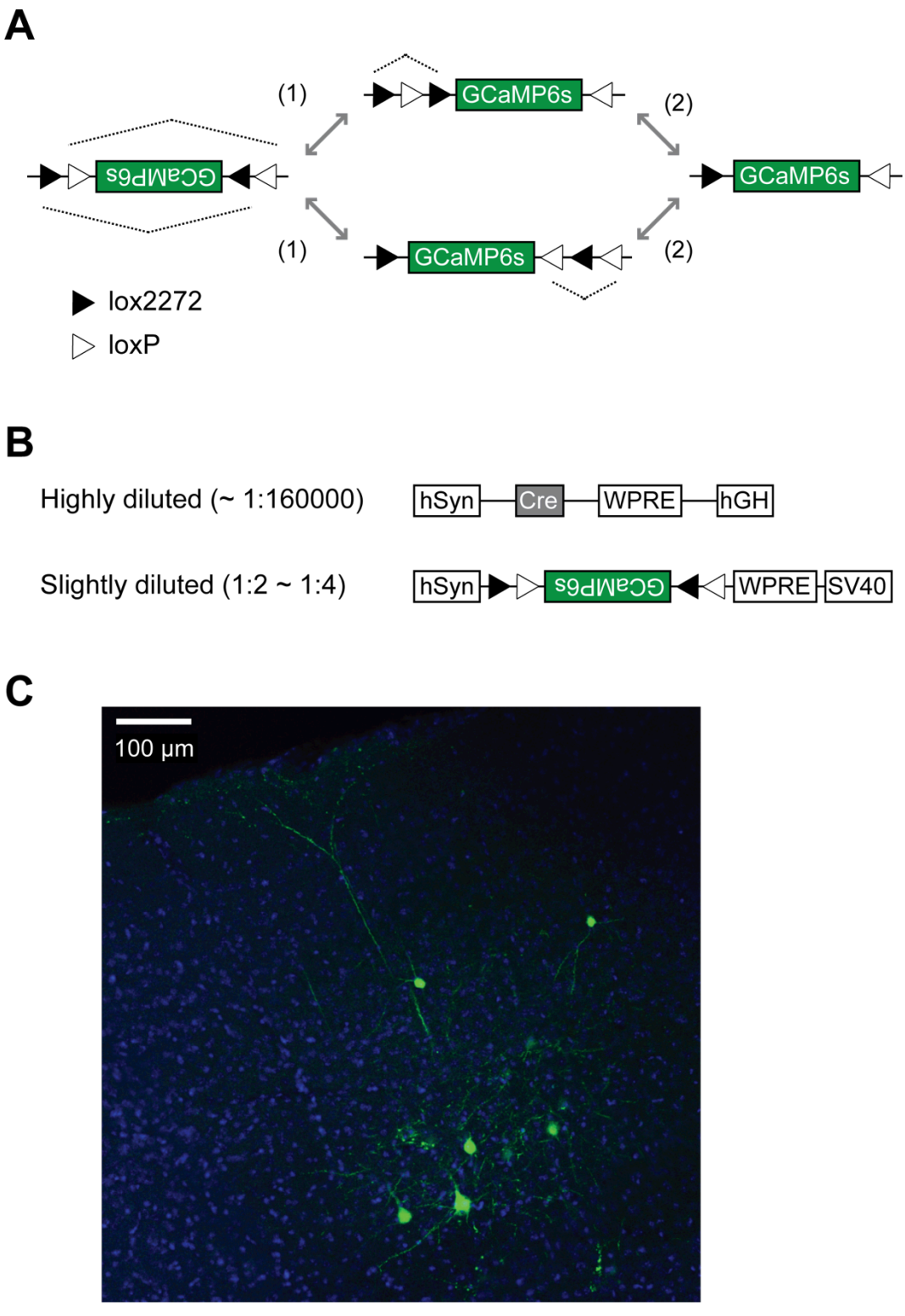

Figure 6.1 Cre-dependent sparse expression of GCaMP6s for dendritic calcium imaging

A, Flex switch recombination sequence for stable inversion mediated by Cre proceeds in two steps: (1) inversion followed by (2) excision. loxP and lox2272 are orthogonal recombination sites. **B**, Construct design for hSyn-Cre-WPRE-hGH and hSyn-Flex-GCaMP6s-WPRE-SV40. Two AAV solutions are injected together. Cre virus is highly diluted (~1:160000) to achieve sparse expression of GCaMP6s. **C**, An example image of sparse expression of GCaMP6s (green) obtained from sliced cortex with DAPI staining (blue).

Therefore I achieved sparse expression of GCaMP6s to identify dendrites by utilizing Cre-dependent gene expression (Sauer, 1998; Atasoy et al., 2008; Sohal et al., 2009) (Fig6.1A). I co-injected two AAV solutions: highly diluted (~ 1:160000) Cre virus and slightly diluted (1:2 ~ 1:4) Flex-GCaMP6s virus (Atasoy et al., 2008) (Fig6.1B). GCaMP6s is expressed in a Cre-dependent manner, and only small subsets of neurons express GCaMP6s since highly diluted Cre virus infects limited number of neurons (Xu et al., 2012a; Chen et al., 2013b) (Fig6.1C). Flex-GCaMP6s is also slightly diluted to avoid over-expression of GCaMP6s (Peters et al., 2014).

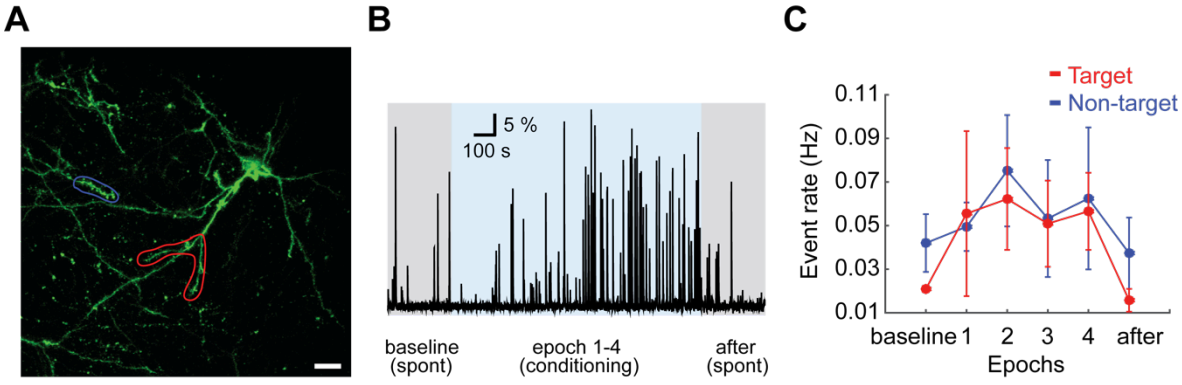

Figure 6.2 Operant conditioning of dendritic activity with two-photon calcium imaging

A, 3D stack image showing target (red) and non-target (blue) neurons in motor cortex with sparsely expressing GCaMP6s. Scale bar represents 20 μm. **B**, Calcium signals from the target dendrite in **A**, showing baseline spontaneous activity ("baseline"), activity during conditioning ("epochs 1-4"), and spontaneous activity after the conditioning ("after"). **C**, Event rate of target (red) and non-target (blue) dendrites during conditioning. N = 2 and 3 dendrites in 2 animals for target and non-target, respectively.

I then performed operant conditioning of dendritic activity using two-photon calcium imaging with GCaMP6s. I chose target dendrite by hand with the identification of neuron (Fig6.2A). I could simultaneously observe non-target dendrite that is not derived from the identified target neuron by occasion. I gave animals water rewards in response to spiking events inferred from calcium signal of target dendrite (Fig6.2B). I observed event rate change of target dendrites as I observed in previous chapters using somatic calcium imaging (Fig6.3C).

Dendritic calcium signals can be derived either from local dendritic spikes or bAPs. If the dendritic signals I observed were mostly bAP-derived signals, operant conditioning of dendritic activity (Fig6.3) is essentially the same as single-target operant conditioning of somatic activity (Chapter 5) since dendritic activity can be considered as a proxy of somatic activity. To investigate if I was able to train animals in response to local-dendritic-spike-derived calcium signals, simultaneous recording of dendritic and somatic activity is needed.

6.2.2 Simultaneous imaging of dendrite and soma

3D two-photon calcium imaging has been developed using piezoelectric focusing element (Göbel et al., 2006; Gobel and Helmchen, 2007), acousto-optic deflector (Katona et al., 2012; Cotton et al., 2013; Fernandez-Alfonso et al., 2014; Froudarakis et al., 2014), spatial light modulator (Anselmi et al., 2011), and electrical tunable lens (Grewe et al., 2011).

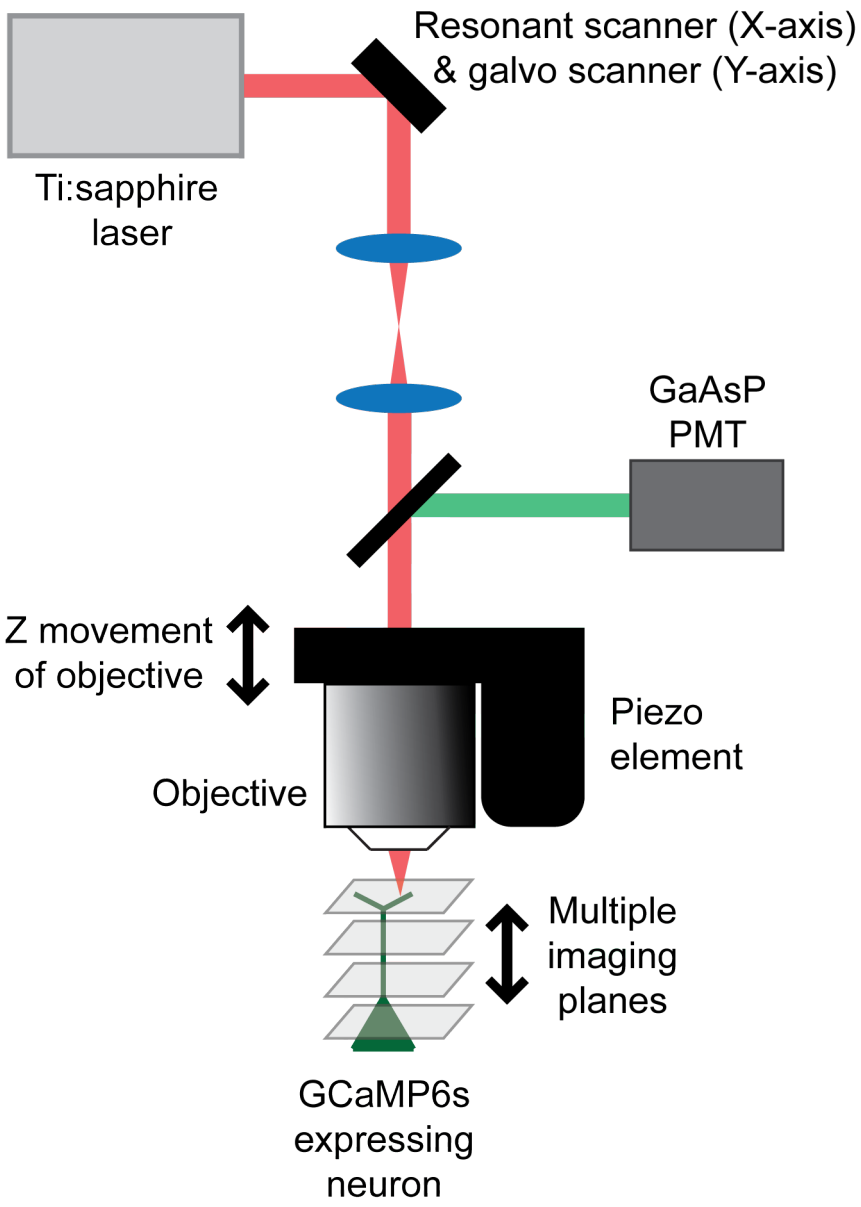

Figure 6.3 Schematic diagram of 3D two-photon imaging

3D two-photon imaging was achieved with resonant scanner (Y-axis), galvo scanner (X-axis), and piezoelectric focusing element (Z-axis). A piezo element induced vibration of the objective lens along z-axis. Multiple imaging planes were acquired in one cycle of z scanning.

I applied a piezoelectric focusing element to our two-photon microscope with a fast-scanning resonant galvanometer (Fan et al., 1999) (Fig6.3). Two-photon

microscopy with resonant scanner allows us to image sufficient amount of pixels much faster than conventional microscopy with galvanometer. For example, two-photon imaging in pervious chapters were conducted with 256 × 512 pixels at 7 Hz, whereas I can image 512 × 512 pixels at 30 Hz using the microscopy with resonant scanner. A piezoelectric focusing unit vibrates in z-axis during x-y scanning so that I can image from multiple planes. One cycle of z scanning takes approximately 2-3 Hz depending on number of image planes (2-7 planes) and gap between image planes (usually 20-30 μm).

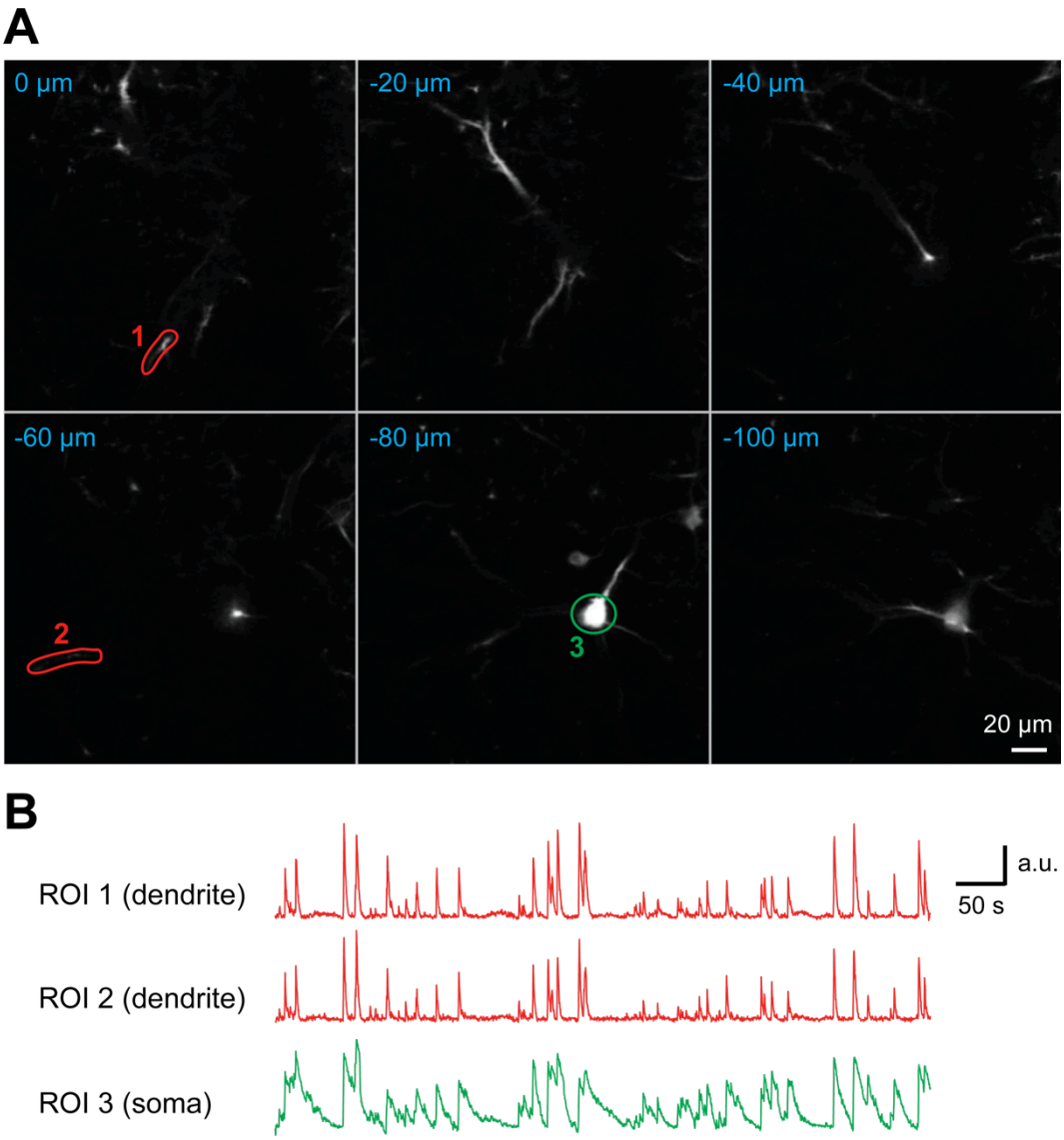

Figure 6.4 Simultaneous recording of dendrite and soma with 3D two-photon calcium imaging

A, Acquired images during 3D two-photon calcium imaging at six depths (positions indicated in blue characters). Three ROIs (two dendrites (red) and a soma (green)) were selected by hand. **B**, Calcium signals from three ROIs in (A) during 3D two-photon imaging in awake mice.

I performed 3D two-photon calcium imaging in either primary somatosensory cortex or primary motor cortex in awake mice. Sparse expression of GCaMP6s allowed us to identify dendrites. Since the axial distance that can be covered by our piezoelectric focusing element is limited to ~140 μm, I firstly targeted shallow-positioned L2 neurons so that I can image both dendrites and soma of the same cell (Fig6.4). ROIs were selected by hand from multiple imaging planes, and calcium signals were analyzed simultaneously for dendrites and soma.

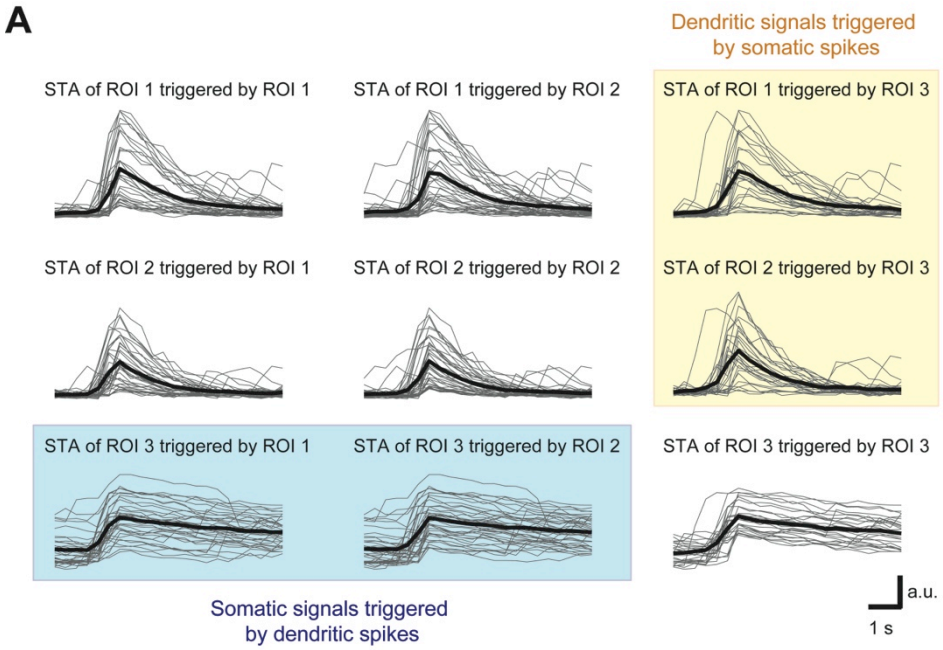
A
Dendritic signals triggered by somatic spikes
STA of ROI 1 triggered by ROI 1
STA of ROI 1 triggered by ROI 2
STA of ROI 1 triggered by ROI 3
STA of ROI 2 triggered by ROI 1
STA of ROI 2 triggered by ROI 2
STA of ROI 2 triggered by ROI 3
STA of ROI 3 triggered by ROI 1
STA of ROI 3 triggered by ROI 2
STA of ROI 3 triggered by ROI 3
Somatic signals triggered by dendritic spikes
a.u.
1 s

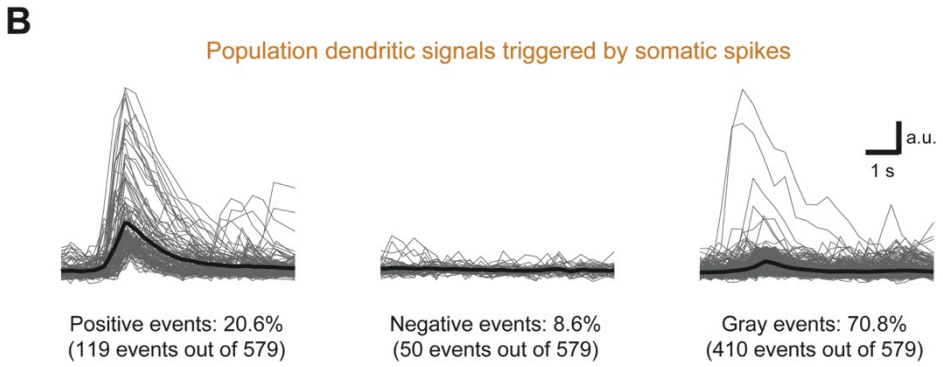
B
Population dendritic signals triggered by somatic spikes
a.u.
1 s
Positive events: 20.6%
(119 events out of 579)
Negative events: 8.6%
(50 events out of 579)
Gray events: 70.8%
(410 events out of 579)

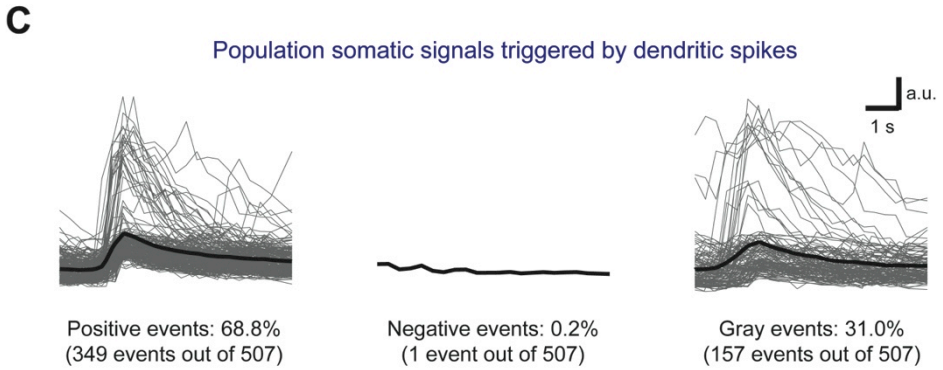
C
Population somatic signals triggered by dendritic spikes
a.u.
1 s
Positive events: 68.8%
(349 events out of 507)
Negative events: 0.2%
(1 event out of 507)
Gray events: 31.0%
(157 events out of 507)

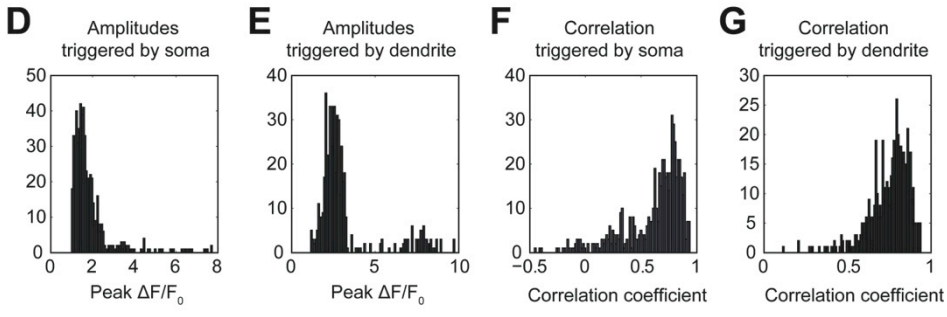
D
Amplitudes triggered by soma
Peak ΔF/F0
E
Amplitudes triggered by dendrite
Peak ΔF/F0
F
Correlation triggered by soma
Correlation coefficient
G
Correlation triggered by dendrite
Correlation coefficient

Figure 6.5 Spike-triggered averages of simultaneously recorded calcium signals from dendrite and soma in shallow-positioned L2 neurons

A, Spike-triggered averages (STAs) of calcium signals from the neuron described in Fig6.4 (ROI 1 and ROI 2 are dendrites, ROI 3 is soma). Thick black and thin gray lines represent mean and each signals, respectively. Dendritic STAs triggered by somatic spikes are highlighted with yellow rectangle. Somatic STAs triggered by dendritic spikes are highlighted with blue rectangle. **B**, Dendritic STAs are pooled from multiple neurons (N = 11 dendrites from 4 neurons). Dendritic STAs are classified into positive events (dendrites co-active with somatic spikes), negative events (dendrites silent with somatic spikes), and gray events (others) from 579 somatic spiking events. **C**, Somatic STAs are pooled from multiple neurons (N = 11 dendrites from 4 neurons). Somatic STAs are classified into positive events (soma co-active with dendritic spikes), negative events (soma silent with dendritic spikes), and gray events (others) from 507 dendritic spiking events. **D**, Histogram of amplitudes of dendritic calcium signals ($\Delta F/F_0$) triggered by somatic spikes (N = 579). **E**, Histogram of amplitudes of somatic calcium signals ($\Delta F/F_0$) triggered by dendritic spikes (N = 507). **F**, Histogram of correlation coefficient between dendritic and somatic calcium signals triggered by somatic calcium spikes (N = 579). **G**, Histogram of correlation coefficient between dendritic and somatic calcium signals triggered by dendritic calcium spikes (N = 507).

I analyzed spike-triggered average (STA) of calcium signals to investigate how co-active dendrites and soma are. I focused on STAs of dendrites and soma triggered by somatic and dendritic spiking events, respectively (Fig6.5A, the same ROIs from Fig6.4).

I classified STAs into three categories: positive events, negative events, and gray events. STAs were defined as positive events if (1) spiking events were detected,

(2) maximum $\Delta F/F_0$ was above 2, and (3) correlation coefficient with the source signal for triggering (e.g., somatic auto-STA with spiking event used for triggering dendritic STA) was over 0.4. Likewise, STAs were defined as negative events if (1) spiking events were not detected, (2) maximum $\Delta F/F_0$ was below 2, and (3) correlation coefficient with the source signal for triggering was below 0.4. If STAs were not classified into neither positive nor negative events, I called these STAs as gray events since I cannot reliably determine if dendrite/soma is co-active with soma/dendrite (Fig6.5 D-G).

Dendritic STAs triggered by somatic spikes were 20.6% positive events (119 events out of 579 somatic spiking events), 8.6% negative events (50 events out of 579 events), and 70.8% gray events (410 events out of 579 events) (Fig6.5B). I can say that bAPs can fail to propagate to dendrites with 8.6% chance from the number of dendritic negative events triggered by somatic spiking events. Somatic STAs triggered by dendritic spikes were 68.8% positive events (349 events out of 507 dendritic spiking events), 0.2% negative events (1 event out of 507 events), and 31.0% gray events (157 events out of 507 events) (Fig6.5C). I can say that somatic signals were highly co-active with dendritic spiking events (68.8% positive events), and there were almost no independent dendritic events that did not cause somatic spikes (0.2% negative events).

It should be noted that there was a very small number of independent dendritic events since I deliberately chose a strict criterion, as my goal was to perform on-line event detection for operant conditioning. The detected independent dendritic events are likely to be dendritic bursts, but confirmation with electrophysiology will be needed to for further discussion.

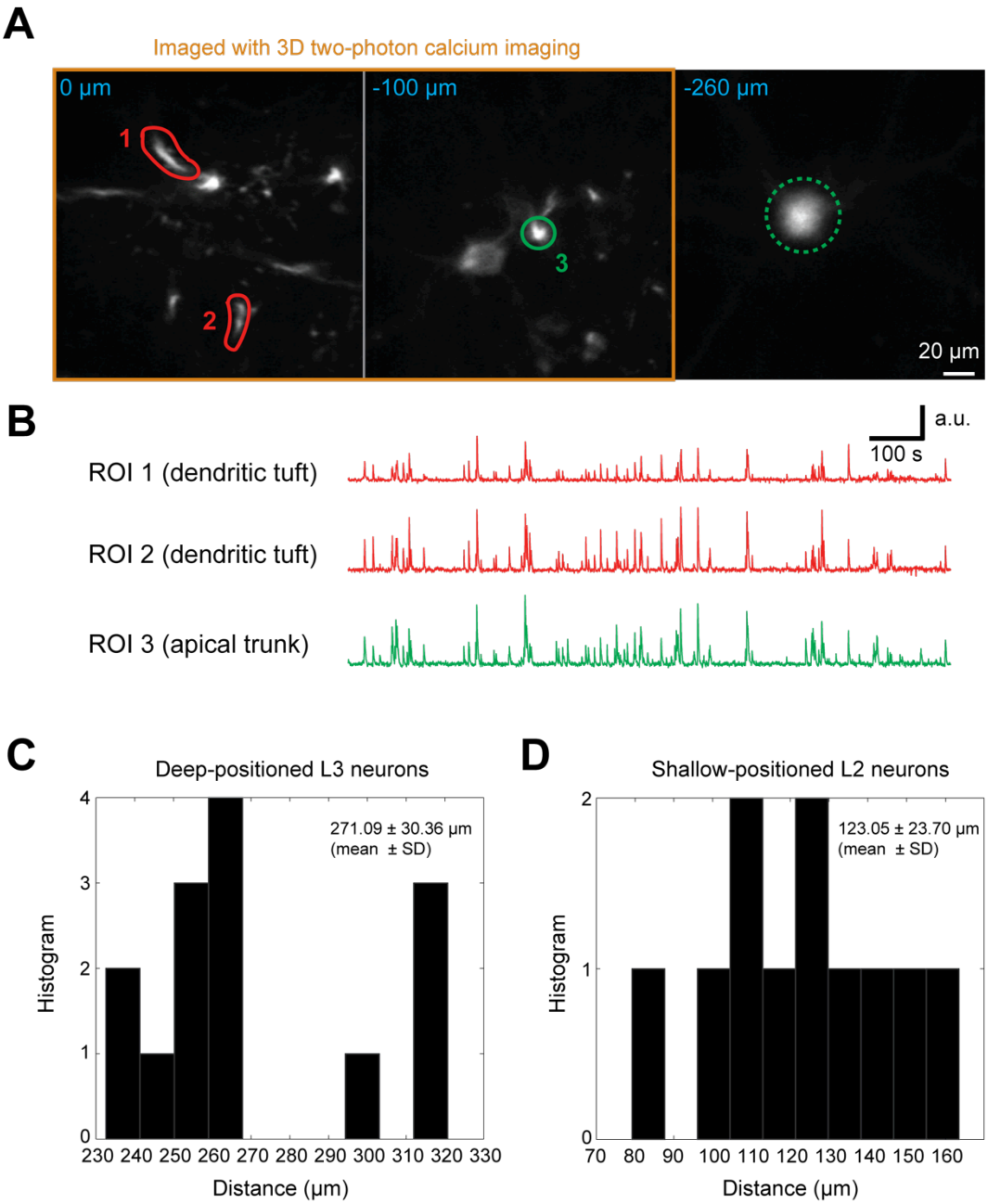

Figure 6.6 Simultaneous calcium imaging of dendritic tuft and apical trunk from deep-positioned L3 neurons

A, 3D two-photon calcium imaging with multiple depth (blue character) covering dendritic tufts and apical trunk (orange rectangle), but not soma. Three ROIs (two dendritic tufts (red) and an apical trunk (green)) coming from the same cell body (dotted green) were selected by hand. **B**, Calcium signals from three ROIs in (A)

during 3D two-photon imaging in awake mice. **C**, **D**, Histogram of distances between dendrites and soma in deep-positioned L3 neurons (C) and shallow-positioned L2 neurons (D).

It has been argued that co-activity of dendrites and soma depends on the distance between them (Waters, 2004). Therefore it is of interest to simultaneously record calcium signals from dendrites and soma in deep-positioned L3 neurons that have longer distances between dendritic tufts and soma. However the limitation of our piezo element covering only ~140 μm does not allow us to simultaneously image dendritic tufts and soma in deep-positioned L3 neurons. So I used calcium signals from apical trunk as a proxy of signals in soma, assuming they are highly co-active given our results from shallow-positioned L2 neurons (Fig6.5). I performed two-photon calcium imaging to simultaneously record signals from dendritic tufts and apical trunks coming from the same cell body (Fig6.6A, B). Distances between dendrites and soma are 271 ± 30 μm (mean ± SD, n = 14 dendrites. Fig6.6C) in deep-positioned L3 neurons. These are longer than distances between dendrites and soma in shallow-positioned L2 neurons: 123.05 ± 23.70 μm (mean ± SD, n = 11. Fig6.6D).

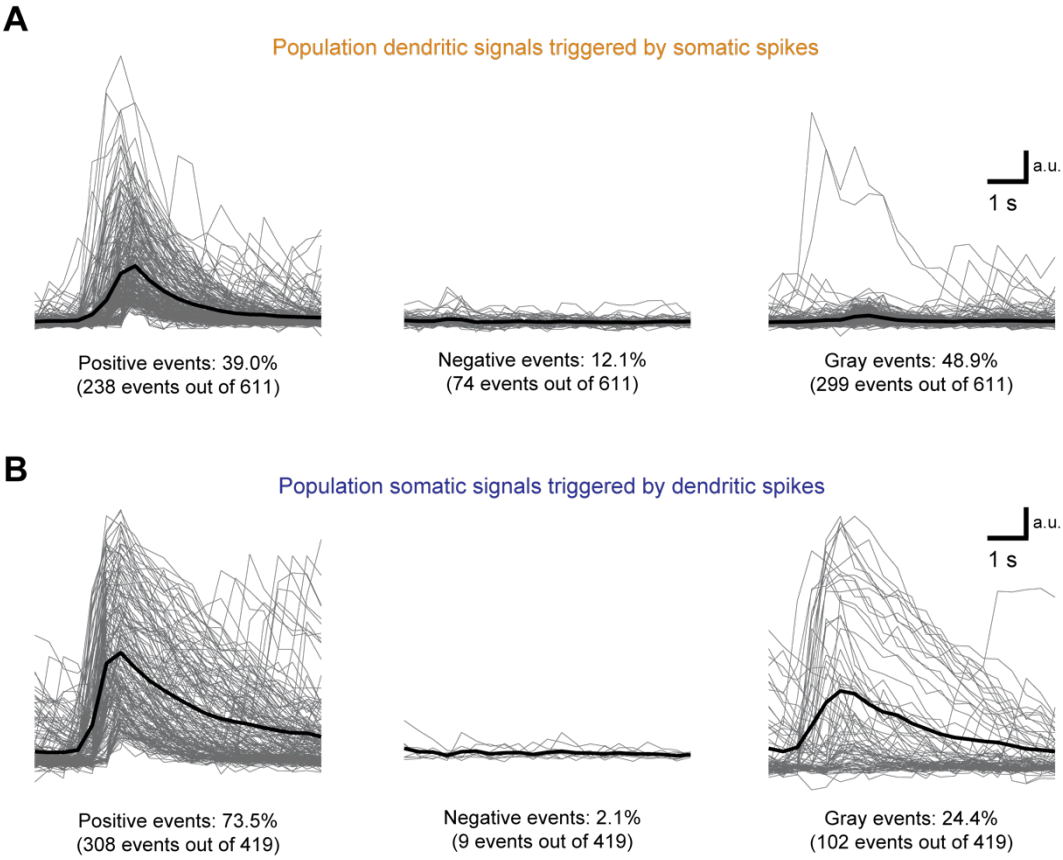

Figure 6.7 Spike-triggered averages of simultaneously recorded calcium signals from dendritic tuft and apical trunk in deep-positioned L3 neurons

A, Dendritic STAs are pooled from multiple neurons (N = 14 dendrites from 6 neurons). Thick black and thin gray lines represent mean and each signals, respectively. Dendritic STAs are classified into positive events (dendrites co-active with somatic spikes), negative events (dendrites silent with somatic spikes), and gray events (others) from 611 somatic spiking events. **B**, Somatic STAs are pooled from multiple neurons (N = 14 dendrites from 6 neurons). Somatic STAs are classified into positive events (soma co-active with dendritic spikes), negative events (soma silent with dendritic spikes), and gray events (others) from 419 dendritic spiking events.

Dendritic STAs (i.e., STA from dendritic tufts) triggered by somatic spikes (i.e., spiking events from apical trunks) were 39.0% positive events (238 events out of

611 somatic spiking events), 12.1% negative events (74 events out of 611 events), and 48.9% gray events (299 events out of 611 events) (Fig6.7A). I can say that bAPs can fail more often to propagate to dendrites with 12.1% chance in deep-positioned L3 neurons than in shallow-positioned L2 neurons (with 8.6% chance of failed propagation). Somatic STAs (i.e., signals from apical trunks) triggered by dendritic spikes (i.e., spiking events from dendritic tufts) were 73.5% positive events (308 events out of 419 dendritic spiking events), 2.1% negative events (9 event out of 419 events), and 24.4% gray events (102 events out of 419 events) (Fig6.7B). I can say that I observed independent dendritic spiking events that did not cause somatic spikes more often in deep-positioned L3 neurons (2.1% negative events) than in shallow-positioned L2 neurons (0.2% negative events).

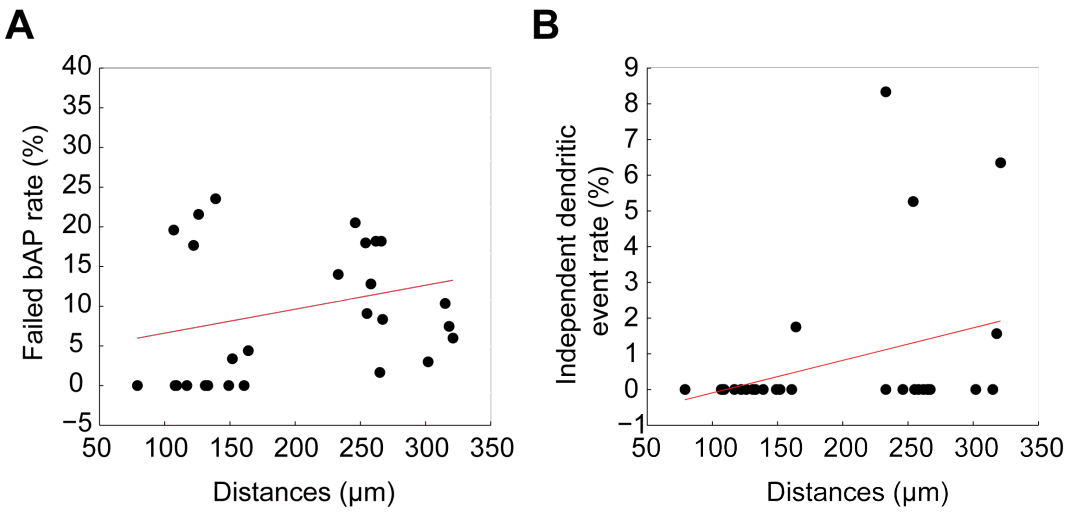

Figure 6.8 Relationships between distance and independence of dendritic activity

A, Rate of failed bAP (negative events of dendritic signals triggered by somatic spikes) as a function of distance between dendrite and soma. Red line shows the result of linear regression (y = 0.030 x + 3.589, R^2 = 0.029, correlation coefficient

0.23, P>0.05). N = 29 dendrite-soma pairs. **B**, Rate of independent dendritic events (negative events of somatic signals triggered by dendritic spikes) as a function of distance between dendrite and soma. Red line shows the result of linear regression (y = 0.009 x – 1.003, R^2 = 0.109, correlation coefficient 0.33, P>0.05). N = 29 dendrite-soma pairs.

I further analyzed the relationships between independence of dendritic activity and distance between dendrite and soma. We calculated the rate of failed bAP, i.e. negative events of dendritic signals triggered by somatic spikes (Fig6.5B, Fig6.7A), and independent dendritic events, i.e. negative events of somatic signals triggered by dendritic spikes (Fig6.5C, Fig6.7B), as a measure of independence of dendritic activity for each dendrite-soma pairs in L2 and L3 neurons. Correlation coefficients between the distance and the occurrence of failed bAP rate and independent dendritic event rate were positive but not statistically significant (Fig6.8).

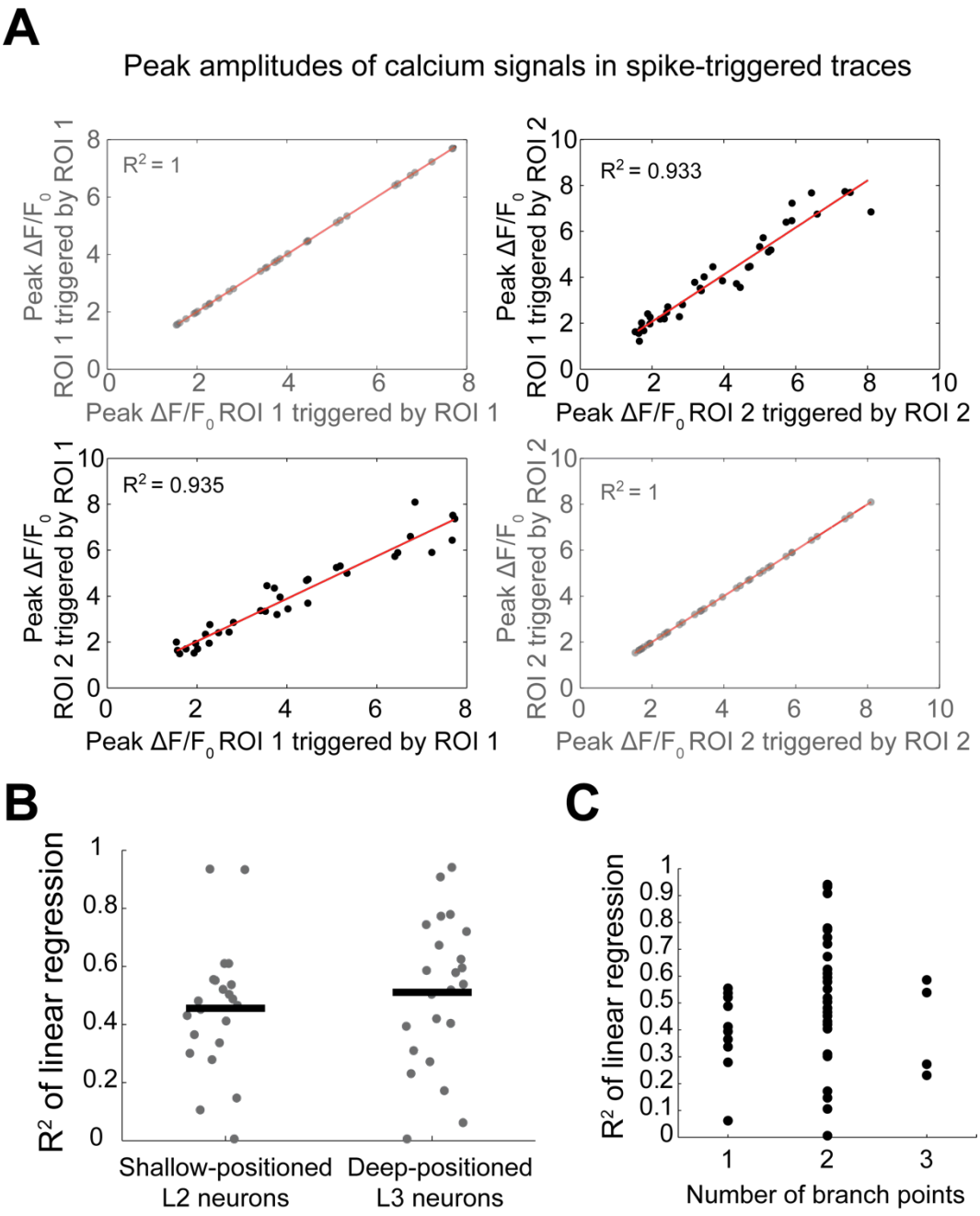

Figure 6.9 Comparisons of amplitudes of spike-triggered calcium signals between dendrites

A, Comparisons of amplitudes of calcium signals in STAs between dendrites. ROI1 and ROI2 are dendrites from Fig6.4/Fig6.6. Both axes indicate peak $\Delta F/F_0$. Black circles and red lines represent comparison of amplitudes at each dendritic spiking event and the results of linear regression, respectively. Plots in diagonal are made transparent because these are auto-comparisons and will not be used

in the following analysis. **B**, R^2 of linear regression in shallow-positioned L2 neurons and deep-positioned L3 neurons. Gray circles and Black bars represent results from each regressions and mean, respectively. **C**, R^2 of linear regression with the function of number of branch points between dendritic branch pairs.

Dendritic calcium signals could be derived from local dendritic/synaptic activity, bAP-evoked activity, or mixture of them. Amplitudes of dendritic calcium signals from different sources could be different, so I hypothesized that comparing calcium amplitudes between dendrites in the same cell could give us information about their sources. I compared amplitudes of calcium signals in STAs I analyzed in Fig6.5 and Fig6.7 to see how much correlated amplitudes of dendritic calcium signals from the same cells are (Fig6.9A). I performed linear regression between $\Delta F/F_0$ peak amplitudes in STAs, and used R^2 (coefficient of determination) as a measure of how much correlated dendritic activities are between branches in the same neurons. It turned out that R^2 values are very variable from dendritic pairs to pairs both in shallow-positioned L2 neurons and deep-positioned L3 neurons (Fig6.9B, C). This result would mean that comparing amplitudes of dendritic calcium signals could be informative in some subsets of dendritic pairs.

6.3 Discussion

6.3.1 Brief summary

In this chapter I firstly demonstrated operant conditioning of dendritic activity using two-photon calcium imaging, then described simultaneous imaging of dendrites and soma in awake animals by utilizing 3D two-photon calcium imaging. GCaMP6s can be sparsely expressed for dendritic calcium imaging by co-injecting highly diluted Cre viral solution and slightly diluted Flex-GCaMP6s viral solution (Fig6.1). I observed event rate change of dendritic activity during operant conditioning of dendrite as I saw with operant conditioning of soma in previous chapters (Fig6.2). I then implemented 3D two-photon imaging by combining fast-scanning resonant scanning and a piezoelectric focusing element (Fig6.3). I simultaneously recorded spontaneous calcium signals from dendrites and soma in shallow-positioned L2 neurons with 3D two-photon imaging (Fig6.4). Dendrites and soma were highly co-active in shallow-positioned L2 neurons, and there were almost no independent spontaneous dendritic spiking events that did not cause somatic spiking events (Fig6.5). I then simultaneously recorded calcium signals from dendritic tufts and apical trunks in deep-positioned L3 neurons, assuming I can use calcium signals from apical trunks as a proxy of signals from soma (Fig6.6). Dendritic tufts and apical trunks were also very co-active in deep-positioned L3 neurons, but I could observe failed bAPs and independent dendritic events more often than in shallow-positioned L2 neurons (Fig6.7). I compared amplitudes of calcium signals in STAs between dendrites, and the correlation between dendrites were varied from dendritic pairs to pairs (Fig6.9).

6.3.2 Local dendritic signals and bAP-derived signals

Dendritic signals can be derived from local dendritic/synaptic activity, bAP-evoked activity at dendrites, or mixture of them (Jia et al., 2010; Chen et al., 2013b; Sheffield and Dombeck, 2014). In order to investigate the function of dendrites for neural computation *in vivo*, it is important to be able to separate sources of dendritic activity (Smith et al., 2013).

I developed 3D two-photon calcium imaging to simultaneously record dendritic and somatic activity in the hope of separating the sources of dendritic activity. I found strong co-activity of dendrites and soma both in shallow-positioned L2 neurons (Fig6.5) and deep-positioned L3 neurons (Fig6.7). I observed independent dendritic activity that did not cause somatic activity more often with deep-positioned L3 neurons than shallow-positioned L2 neurons (Fig6.5C, Fig6.7B), but the chance was still very low (2.1%, 9 independent events out of 419 dendritic events, 108 min recording from 14 dendrites in 6 neurons).

I might be able to improve the chance to observe independent dendritic events by replacing somatic calcium imaging with somatic cell-attached recording (i.e., by performing simultaneous dendritic calcium imaging and somatic cell-attached recording). I had to define gray events (Fig6.5, Fig6.7) because of low temporal resolution and low SNR of 3D two-photon calcium imaging, but I might be able to reduce the ratio of gray events by recording somatic activity using cell-attached recording that has higher temporal resolution and higher SNR.

6.3.3 Optical operant conditioning of independent dendritic signals

Our motivation to separate independent dendritic signals and bAP-derived signals is to perform optical operant conditioning in response to independent dendritic activity. That is, animals will get rewarded if target dendrite showed dendritic activity without somatic activity using either 3D two-photon calcium imaging or simultaneous dendritic two-photon calcium imaging and somatic cell-attached recording. This experiment would show that dendritic activity could be specifically targeted by behavior as an independent functional unit.

I observed independent dendritic events at ~0.001 Hz (9 events per 108 min) in deep-positioned L3 neurons using 3D two-photon calcium imaging (Fig6.7B). This rate is far smaller than event rates of target neuron I used for optical operant conditioning (Fig4.4, Fig4.7, Fig5.2). Utilizing somatic cell-attached recording might increase the probability of observing independent events to some extent, but it would be necessary to find different experimental conditions in which I can observe independent dendritic events more often to achieve efficient operant conditioning.

6.3.4 Possible applications of 3D two-photon calcium imaging

3D two-photon calcium imaging can also be applied to neuronal population imaging from multiple depths. I am able to observe neuronal activity from >1000 cells with 3D two-photon calcium imaging (data not shown).

In single-target optical operant conditioning, I observed that non-target neurons in the FOV did not correlate their activity change with their relationships to target neurons (Fig5.6). These results suggest that neuronal assemblies generated by operant conditioning can be highly sparse (at least as sparse as our FOV, 250 × 250 μm). One possible way to find neuronal assemblies during operant conditioning would be to record from large numbers of neurons across multiple cortical depths. This idea can be supported by the fact that clonally related neurons are tend to be connected to each other, and they are often organized in close horizontal locations at different cortical depth forming “mini-columns” (Yu et al., 2009; Li et al., 2012; Ohtsuki et al., 2012; Yu et al., 2012).

7 General discussion and outlook

7.1 Summary of results

In this thesis, I developed on-line analysis of two-photon calcium imaging (Chapter 3). I applied the developed methods to perform optical operant conditioning by rewarding animals in response to neuronal activity analyzed on-line. I firstly performed multi-target optical operant conditioning, and animals learned to increase the activity of both target and non-target control population in a non-specific manner (Chapter 4). I then performed single-target optical operant conditioning, and animals learned to increase the activity of target neurons in a specific manner. Animals also learned to increase the activity earlier the session over multiple days (Chapter 5). I performed optical operant conditioning of dendritic activity, and animals leaned to change the activity during conditioning. With the aim of applying this method for optical operant conditioning of independent dendritic activity, I also developed simultaneous recording of dendritic and somatic activity by utilizing 3D two-photon calcium imaging (Chapter 6).

In this section I will discuss the context and meaning of these results in more details, and possible future experiments as well.

7.2 Modulated activity of specific neuronal assembly during operant conditioning

Neuronal populations can be trained in a non-specific manner during multi-target operant conditioning (Fig4.4). Single target neurons can be trained during operant conditioning, in the absence of a significant increase in their local neighbors (Fig5.2). Increase in the target neuron's activity primes operant conditioning over subsequent days (Fig5.2). Here I would like to raise two possibilities about mechanisms for phenomena observed during operant conditioning: mechanism for increasing in neuronal activity, and mechanism of priming of operant conditioning.

Regarding mechanisms for the increase in neuronal activity, there are two possible candidates: increased input rate from upstream neurons that excite target neurons, and increased synaptic efficacy from upstream neurons to the target neurons. I chose layer 2/3 neurons in primary motor cortex for operant conditioning, and these neurons are mainly innervated by neurons in frontal cortex (Hooks et al., 2013; Oh et al., 2014), motor thalamic nuclei (Hooks et al., 2013; Oh et al., 2014), and primary motor cortex in a recurrent way (Weiler et al., 2008; Oh et al., 2014). Increased activity of the upstream neurons might have played a key role for the increase in activity of target neurons, and identifying the upstream neurons will be necessary to understand how animals searched specific neuronal population that is linked to the reward during operant conditioning. Increased synaptic efficacy from the upstream neurons might also have caused the

increase in activity of target neurons. Since primary motor cortex is also innervated by dopaminergic neurons in ventral tegmental area (VTA), dopaminergic modulation of synaptic strength might have played a key role (Bao et al., 2001; Hosp et al., 2011; Oh et al., 2014) with possible engagement of STDP (Izhikevich, 2006; Legenstein et al., 2008; Legenstein et al., 2010; Cassenaer and Laurent, 2012).

Regarding the mechanism for priming, sustained plasticity in neural circuits over subsequent days would be one of the most plausible candidates. For example persistent plasticity in cerebellar nuclei has been investigated as a mechanism for savings in motor learning (Medina et al., 2001), and cerebellar nuclei could be one of the upstream neurons for primary motor cortex via motor thalamic nuclei during operant conditioning (Kuramoto et al., 2009; Kuramoto et al., 2011; Oh et al., 2014).

Understanding these mechanisms would lead us to understand how animals searched specific neuronal population activity that is linked to the rewards during operant conditioning. It might be unclear to the mouse which neuron's activity is rewarded during operant conditioning with four target neurons, whereas it was clear enough with single target neurons. This idea is supported by the fact that target and non-target neurons are co-active at the same time more often during multi-target conditioning than single-target conditioning (Fig5.6). There have been researches similar to our work that is published recently (Clancy et al., 2014; Hira et al., 2014), and their results also indicate possible mechanisms of how animals search the reward-related population. Clancy et al. showed that local neighbors increased activity together with target neurons at the early stage of

learning, and fewer number of neighbors increased activity along targets at the late stage of learning. This might indicate that animals firstly take a rough guess about reward-related neurons, and then learn to search the neurons with finer spatial resolution over multiple days. Hira et al. showed that increase/decrease in the activity of non-target neurons depends on their timing of active moments compared to reward timing. This result might imply STDP-dependent modulation of neuronal activity during operant conditioning, although this phenomenon was not confirmed at least with our data (Fig5.5D).

7.3 Outlook

Open questions from our results on optical operant conditioning of cortical population activity are (1) mechanisms of increased activity of specific neuronal population (as discussed in the previous section), and (2) why I did not clearly observe specific non-target neurons that increase activity together with target neurons during operant conditioning.

To answer question (1) I can tackle four sub-questions: whether the input rate of upstream neurons increased during conditioning, whether input efficacy from upstream neurons increased during conditioning, weather the excitability of target neurons increased during conditioning, and whether upstream neurons showed persistent plasticity over subsequent days as I discussed in chapter 7.2.

To investigate whether the input rate of upstream neurons increased during conditioning, I need to observe activity of upstream neurons together with target

neurons. This can be achieved with simultaneous two-photon calcium imaging of target neurons and upstream neurons, and one way to perform this would be simultaneous imaging of dendrites of target neurons and axons of upstream neurons. As I described in chapter 6, dendritic calcium signals are highly co-active with somatic signals especially with shallow-positioned L2 neurons. This means that I could use dendritic calcium signals as a proxy of somatic calcium signals. Since axons from frontal cortex and motor thalamic nuclei innervate layer 1 of primary motor cortex (Kuramoto et al., 2009; Hooks et al., 2013; Oh et al., 2014), axons of these area and dendritic tufts of primary motor cortex can be imaged in the same FOV. Dendrites and axons can be identified from their morphological difference (i.e., dendrites have spines whereas axons have boutons). I could perform two-color imaging (i.e., using green and red fluorescence) to separate dendrites and axons. RFP variants (Campbell et al., 2002; Davidson and Campbell, 2009; Day and Davidson, 2009) could be co-expressed with GCaMP6s specifically in upstream neurons to separate axons from dendrites expressing only GCaMP6s. I could also express red fluorescent genetically encoded calcium indicators (Zhao et al., 2011; Akerboom et al., 2013; Inoue et al., 2014) in upstream neurons to separate axons from dendrites expressing GCaMP6s. These methods will enable us to observe activity change of upstream neurons during operant conditioning of target neurons.

Investigating whether input efficacy from upstream neurons increased during conditioning would not be straightforward since it is difficult to observe synaptic efficacy with calcium imaging. I can estimate changes in synaptic strength by observing structural plasticity of dendritic spines during learning (Trachtenberg et

al., 2002; Matsuzaki et al., 2004; Holtmaat et al., 2006; Xu et al., 2009; Yang et al., 2009; Fu et al., 2012; Peters et al., 2014). I can also investigate the role of dopamine during optical operant conditioning by replacing/combining water rewards with optogenetic stimulation/inhibition of dopaminergic neurons in VTA. This is possible with expressing ChR2/NpHR variants (Boyden et al., 2005; Zhang et al., 2007; Yizhar et al., 2011; Berndt et al., 2014) specifically in dopaminergic neurons under tyrosine hydroxylase (TH) or dopamine transporter (DAT) promoters combined with light stimulation through optical fiber (Tsai et al., 2009; Adamantidis et al., 2011; Cohen et al., 2012; Tye et al., 2013). These experiments will give us more insights about how synaptic plasticity is involved in operant conditioning. Increased excitability of target neurons can also account for increased event rate during conditioning. Excitability can be estimated with input resistance of the cell, and input resistance can be modulated as a result of intrinsic plasticity (Desai et al., 1999; Zhang and Linden, 2003). It will be required to perform whole-cell recording to monitor change in input resistance during the task. Chronic observation of changes in synaptic strength will shed light on whether upstream neurons showed persistent plasticity over subsequent days.

Question (2) (i.e., why I did not clearly observe specific non-target neurons that increase activity together with target neurons during operant conditioning) could simply be answered by our limited size of FOV (250 × 250 μm). That is, cell assembly generated by operant conditioning might be sparsely organized in large 3D space and I have simply missed them in our FOV. 3D two-photon population

calcium imaging will give us opportunity to chase for the assembly during conditioning as discussed in chapter 6.3.4.

Neuronal circuits in motor cortex can be treated as dynamical systems (Churchland et al., 2012; Mante et al., 2013; Shenoy et al., 2013). It has been reported that BMI learning was more efficient when an intrinsic manifold was used to control machines, indicating that the existing structure of a network can shape learning (Sadtler et al., 2014). This idea can be applied to optical operant conditioning. I could define target "manifold" by analyzing activity of neuronal population and reward animals in response to the activity of the target manifold. For example, I could simply apply principal component analysis (PCA) to neuronal population signals and train mice in response to the activity of first principal component. In this way I might have more chance to observe specific neuronal population within an existing network increasing their activity during learning. Two-photon calcium imaging will also allow us to constrain neuronal activity in a cell-type specific manner (e.g., targeting intrinsic manifold with interneurons) utilizing genetic engineering.

Corticostriatal circuit is reported to exhibit plasticity during neuroprosthetic learning without physical movement, and disrupting the plasticity impairs learning (Koralek et al., 2012). It is possible that the same kind of plasticity was ongoing during our task, and studying corticostriatal circuit might give us more insight about what we observed in the task.

Optical operant conditioning of dendritic activity will give us direct evidence that dendrites can work as a functional unit for behavior. Our results with layer 2/3

neurons in primary motor cortex using 3D two-photon calcium imaging showed very low rate of spontaneous independent dendritic signals, making it difficult to perform optical operant conditioning with these neurons. I could perform cell-attached somatic recording to increase SNR and temporal resolution for separating dendritic and somatic signals, but it is in anyway necessary to search for cortical area/layer to obtain higher rate of independent dendritic activity to perform operant conditioning.

This project originated with the aim to investigate how neural circuits represent information during behavior. In this context I aimed to identify for cell assemblies (Harris et al., 2003; Buzsáki, 2010) by observing neuronal populations that increase their activity together with target neurons. I did not observe the assembly at least in our limited experimental environment during operant conditioning, and this outcome produced several open questions to tackle. Further development in scientific methods will enable us to study more questions that are difficult to address at this moment, and further accumulation of scientific knowledge will enable us to create more questions. I hope to keep advancing to understand our very original question: how the brain works.

References

Adamantidis AR, Tsai HC, Boutrel B, Zhang F, Stuber GD, Budygin EA, Tourino C, Bonci A, Deisseroth K, de Lecea L (2011) Optogenetic Interrogation of Dopaminergic Modulation of the Multiple Phases of Reward-Seeking Behavior. Journal of Neuroscience 31:10829-10835.

Akerboom J et al. (2013) Genetically encoded calcium indicators for multi-color neural activity imaging and combination with optogenetics. Frontiers in molecular neuroscience 6:2.

Akerboom J et al. (2012) Optimization of a GCaMP Calcium Indicator for Neural Activity Imaging. Journal of Neuroscience 32:13819-13840.

Anselmi F, Ventalon C, Begue A, Ogden D, Emiliani V (2011) Three-dimensional imaging and photostimulation by remote-focusing and holographic light patterning. Proc Natl Acad Sci U S A 108:19504-19509.

Atasoy D, Aponte Y, Su HH, Sternson SM (2008) A FLEX switch targets Channelrhodopsin-2 to multiple cell types for imaging and long-range circuit mapping. Journal of Neuroscience 28:7025-7030.

Averbeck BB, Lee D (2004) Coding and transmission of information by neural ensembles. Trends Neurosci 27:225-230.

Averbeck BB, Latham PE, Pouget A (2006) Neural correlations, population coding and computation. Nature Reviews Neuroscience 7:358-366.

Bao S, Chan VT, Merzenich MM (2001) Cortical remodelling induced by activity of ventral tegmental dopamine neurons. Nature 412:79-83.

Bermudez Contreras EJ, Schjetnan AGP, Muhammad A, Bartho P, McNaughton BL, Kolb B, Gruber AJ, Luczak A (2013) Formation and Reverberation of Sequential Neural Activity Patterns Evoked by Sensory Stimulation Are Enhanced during Cortical Desynchronization. In: Neuron, pp 555-566.

Berndt A, Lee SY, Ramakrishnan C, Deisseroth K (2014) Structure-guided transformation of channelrhodopsin into a light-activated chloride channel. Science 344:420-424.

Bi GQ, Poo MM (1998) Synaptic modifications in cultured hippocampal neurons: dependence on spike timing, synaptic strength, and postsynaptic cell type. J Neurosci 18:10464-10472.

Boureau Y-L, Dayan P (2010) Opponency Revisited: Competition and Cooperation Between Dopamine and Serotonin. Neuropsychopharmacology 36:74-97.

Boyden ES, Zhang F, Bamberg E, Nagel G, Deisseroth K (2005) Millisecond-timescale, genetically targeted optical control of neural activity. Nat Neurosci 8:1263-1268.

Branco T, Häusser M (2010) The single dendritic branch as a fundamental functional unit in the nervous system. Current opinion in neurobiology 20:494-502.

Branco T, Clark BA, Hausser M (2010) Dendritic Discrimination of Temporal Input Sequences in Cortical Neurons. Science (New York, NY) 329:1671-1675.

Burgess N, O'Keefe J (2011) Models of place and grid cell firing and theta rhythmicity. Curr Opin Neurobiol 21:734-744.

Buzsáki G (2010) Neural syntax: cell assemblies, synapsembles, and readers. Neuron 68:362-385.

Campbell RE, Tour O, Palmer AE, Steinbach PA, Baird GS, Zacharias DA, Tsien RY (2002) A monomeric red fluorescent protein. Proc Natl Acad Sci U S A 99:7877-7882.

Carlezon WA, Carlezon WA, Chartoff EH, Chartoff EH (2007) Intracranial self-stimulation (ICSS) in rodents to study the neurobiology of motivation. Nature protocols 2:2987-2995.

Carmena JM, Lebedev MA, Henriquez CS, Nicolelis MAL (2005) Stable ensemble performance with single-neuron variability during reaching movements in primates. Journal of Neuroscience 25:10712-10716.

Carmena JM, Lebedev MA, Crist RE, O'Doherty JE, Santucci DM, Dimitrov DF, Patil PG, Henriquez CS, Nicolelis MAL (2003) Learning to Control a Brain–Machine Interface for Reaching and Grasping by Primates. In: PLoS Biol., p e2.

Cassenaer S, Laurent G (2012) Conditional modulation of spike-timing-dependent plasticity for olfactory learning. Nature 482:47-52.

Centonze VE, White JG (1998) Multiphoton excitation provides optical sections from deeper within scattering specimens than confocal imaging. Biophys J 75:2015-2024.

Cerf M, Thiruvengadam N, Mormann F, Kraskov A, Quiroga RQ, Koch C, Fried I (2010) On-line, voluntary control of human temporal lobe neurons. Nature 467:1104-1108.

Chapin JK, Moxon KA, Markowitz RS, Nicolelis MAL (1999) Real-time control of a robot arm using simultaneously recorded neurons in the motor cortex. In: Nature Neuroscience, pp 664-670.

Chen JL, Pfaffli OA, Voigt FF, Margolis DJ, Helmchen F (2013a) Online correction of licking-induced brain motion during two-photon imaging with a tunable lens. The Journal of physiology 591:4689-4698.

Chen Q, Cichon J, Wang W, Qiu L, Lee SJ, Campbell NR, Destefino N, Goard MJ, Fu Z, Yasuda R, Looger LL, Arenkiel BR, Gan WB, Feng G (2012) Imaging neural activity using Thy1-GCaMP transgenic mice. Neuron 76:297-308.

Chen SX, Kim AN, Peters AJ, Komiyama T (2015) Subtype-specific plasticity of inhibitory circuits in motor cortex during motor learning. Nat Neurosci.

Chen T-W, Wardill TJ, Sun Y, Pulver SR, Renninger SL, Baohan A, Schreiter ER, Kerr RA, Orger MB, Jayaraman V, Looger LL, Svoboda K, Kim DS (2013b) Ultrasensitive fluorescent proteins for imaging neuronal activity. Nature 499:295-300.

Chen X, Leischner U, Rochefort NL, Nelken I, Konnerth A (2011) Functional mapping of single spines in cortical neurons in vivo. In: Nature, pp 501-505.

Churchland MM, Cunningham JP, Kaufman MT, Foster JD, Nuyujukian P, Ryu SI, Shenoy KV (2012) Neural population dynamics during reaching. Nature 487:51-56.

Clancy KB, Koralek AC, Costa RM, Feldman DE, Carmena JM (2014) Volitional modulation of optically recorded calcium signals during neuroprosthetic learning. Nature Neuroscience 17:807-809.

Cohen JY, Haesler S, Vong L, Lowell BB, Uchida N (2012) Neuron-type-specific signals for reward and punishment in the ventral tegmental area. Nature 482:85-88.

Cohen MR, Maunsell JHR (2009) Attention improves performance primarily by reducing interneuronal correlations. Nature Neuroscience 12:1594-1600.

Conchello JA, Lichtman JW (2005) Optical sectioning microscopy. Nat Methods 2:920-931.

Cotton RJ, Froudarakis E, Storer P, Saggau P, Tolias AS (2013) Three-dimensional mapping of microcircuit correlation structure. Front Neural Circuits 7:151.

Davidson MW, Campbell RE (2009) Engineered fluorescent proteins: innovations and applications. Nat Methods 6:713-717.

Day RN, Davidson MW (2009) The fluorescent protein palette: tools for cellular imaging. Chemical Society reviews 38:2887-2921.

Dayan P, Abbott LF (2001) Theoretical neuroscience : computational and mathematical modeling of neural systems. Cambridge, Mass.: Massachusetts Institute of Technology Press.

Denk W, Strickler JH, Webb WW (1990) Two-photon laser scanning fluorescence microscopy. Science 248:73-76.

Desai NS, Rutherford LC, Turrigiano GG (1999) Plasticity in the intrinsic excitability of cortical pyramidal neurons. Nat Neurosci 2:515-520.

Dittgen T, Nimmerjahn A, Komai S, Licznerski P, Waters J, Margrie TW, Helmchen F, Denk W, Brecht M, Osten P (2004) Lentivirus-based genetic manipulations of cortical neurons and their optical and electrophysiological monitoring in vivo. Proc Natl Acad Sci U S A 101:18206-18211.

Dombeck DA, Graziano MS, Tank DW (2009) Functional clustering of neurons in motor cortex determined by cellular resolution imaging in awake behaving mice. J Neurosci 29:13751-13760.

Dombeck DA, Khabbaz AN, Collman F, Adelman TL, Tank DW (2007) Imaging Large-Scale Neural Activity with Cellular Resolution in Awake, Mobile Mice. In: Neuron, pp 43-57.

Dombeck DA, Harvey CD, Tian L, Looger LL, Tank DW (2010) Functional imaging of hippocampal place cells at cellular resolution during virtual navigation. Nature Neuroscience 13:1433-1440.

Douglas RJ, Martin KA (2004) Neuronal circuits of the neocortex. Annu Rev Neurosci 27:419-451.

Eichenbaum H, Dudchenko P, Wood E, Shapiro M, Tanila H (1999) The hippocampus, memory, and place cells: is it spatial memory or a memory space? Neuron 23:209-226.

Einevoll GT, Franke F, Hagen E, Pouzat C, Harris KD (2012) Towards reliable spike-train recordings from thousands of neurons with multielectrodes. Current opinion in neurobiology 22:11-17.

Fan GY, Fujisaki H, Miyawaki A, Tsay RK, Tsien RY, Ellisman MH (1999) Video-rate scanning two-photon excitation fluorescence microscopy and ratio imaging with cameleons. Biophys J 76:2412-2420.

Fernandez-Alfonso T, Nadella KM, Iacaruso MF, Pichler B, Ros H, Kirkby PA, Silver RA (2014) Monitoring synaptic and neuronal activity in 3D with synthetic and genetic indicators using a compact acousto-optic lens two-photon microscope. J Neurosci Methods 222:69-81.

Ferster CB, Skinner BF (1957) Schedules of Reinforcement. Psychol Rep 3:695-695.

Ferster D, Miller KD (2000) Neural mechanisms of orientation selectivity in the visual cortex. Annu Rev Neurosci 23:441-471.

Fetz EE (1969) Operant Conditioning of Cortical Unit Activity. In: Science (New York, N.Y.), pp 955-958.

Fetz EE (2007) Volitional control of neural activity: implications for brain-computer interfaces. In: J. Physiol. (Lond.), pp 571-579.

Fetz EE, Baker MA (1973) Operantly conditioned patterns on precentral unit activity and correlated responses in adjacent cells and contralateral muscles. Journal of Neurophysiology 36:179-204.

Froudarakis E, Berens P, Ecker AS, Cotton RJ, Sinz FH, Yatsenko D, Saggau P, Bethge M, Tolias AS (2014) Population code in mouse V1 facilitates readout of natural scenes through increased sparseness. Nat Neurosci 17:851-857.

Fu M, Yu X, Lu J, Zuo Y (2012) Repetitive motor learning induces coordinated formation of clustered dendritic spines in vivo. Nature 483:92-95.

Fujisawa S, Amarasingham A, Harrison MT, Buzsáki G (2008) Behavior-dependent short-term assembly dynamics in the medial prefrontal cortex. In: Nature Neuroscience, pp 823-833.

Ganguly K, Carmena JM (2009) Emergence of a stable cortical map for neuroprosthetic control. PLoS Biology 7:e1000153.

Garner AR, Rowland DC, Hwang SY, Baumgaertel K, Roth BL, Kentros C, Mayford M (2012) Generation of a synthetic memory trace. Science (New York, NY) 335:1513-1516.

Gentet LJ (2012) Functional diversity of supragranular GABAergic neurons in the barrel cortex. Frontiers in neural circuits 6:52.

Gobel W, Helmchen F (2007) New angles on neuronal dendrites in vivo. J Neurophysiol 98:3770-3779.

Göbel W, Kampa BM, Helmchen F (2006) Imaging cellular network dynamics in three dimensions using fast 3D laser scanning. Nature methods 4:73-79.

Gollisch T, Meister M (2008) Rapid neural coding in the retina with relative spike latencies. Science 319:1108-1111.

Govindarajan A, Israely I, Huang SY, Tonegawa S (2011) The dendritic branch is the preferred integrative unit for protein synthesis-dependent LTP. Neuron 69:132-146.

Green AM, Kalaska JF (2011) Learning to move machines with the mind. Trends Neurosci 34:61-75.

Greenberg DS, Houweling AR, Kerr JND (2008) Population imaging of ongoing neuronal activity in the visual cortex of awake rats. In: Nature Neuroscience, pp 749-751.

Grewe BF, Voigt FF, van 't Hoff M, Helmchen F (2011) Fast two-layer two-photon imaging of neuronal cell populations using an electrically tunable lens. Biomedical optics express 2:2035-2046.

Grienberger C, Konnerth A (2012) Imaging calcium in neurons. Neuron 73:862-885.

Grynkiewicz G, Poenie M, Tsien RY (1985) A new generation of Ca2+ indicators with greatly improved fluorescence properties. The Journal of biological chemistry 260:3440-3450.

Guo ZV, Hires SA, Li N, O'Connor DH, Komiyama T, Ophir E, Huber D, Bonardi C, Morandell K, Gutnisky D, Peron S, Xu N-L, Cox J, Svoboda K (2014) Procedures for Behavioral Experiments in Head-Fixed Mice. In: PLoS ONE, p e88678.

Hafting T, Fyhn M, Bonnevie T, Moser MB, Moser EI (2008) Hippocampus-independent phase precession in entorhinal grid cells. Nature 453:1248-1252.

Han F, Caporale N, Dan Y (2008) Reverberation of Recent Visual Experience in Spontaneous Cortical Waves. In: Neuron, pp 321-327.

Harris KD (2005) Neural signatures of cell assembly organization. Nature Reviews Neuroscience 6:399-407.

Harris KD, Mrsic-Flogel TD (2013) Cortical connectivity and sensory coding. Nature 503:51-58.

Harris KD, Csicsvari J, Hirase H, Dragoi G, Buzsáki G (2003) Organization of cell assemblies in the hippocampus. Nature 424:552-556.

Harris KD, Henze DA, Hirase H, Leinekugel X, Dragoi G, Czurkó A, Buzsáki G (2002) Spike train dynamics predicts theta-related phase precession in hippocampal pyramidal cells. Nature 417:738-741.

Harvey CD, Svoboda K (2007) Locally dynamic synaptic learning rules in pyramidal neuron dendrites. Nature 450:1195-1200.

Harvey CD, Coen P, Tank DW (2012) Choice-specific sequences in parietal cortex during a virtual-navigation decision task. In: Nature, pp 62-68.

Harvey CD, Yasuda R, Zhong H, Svoboda K (2008) The Spread of Ras Activity Triggered by Activation of a Single Dendritic Spine. Science (New York, NY) 321:136-140.

Harvey CD, Collman F, Dombeck DA, Tank DW (2009) Intracellular dynamics of hippocampal place cells during virtual navigation. Nature 461:941-946.

Hatsopoulos NG, Donoghue JP (2009) The science of neural interface systems. Annual review of neuroscience 32:249-266.

Hausser M, Mel B (2003) Dendrites: bug or feature? Curr Opin Neurobiol 13:372-383.

Hausser M, Spruston N, Stuart GJ (2000) Diversity and dynamics of dendritic signaling. Science 290:739-744.

Hebb DO (1949) The organization of behavior; a neuropsychological theory. New York,: Wiley.

Helmchen F, Denk W (2002) New developments in multiphoton microscopy. Curr Opin Neurobiol 12:593-601.

Helmchen F, Denk W (2005) Deep tissue two-photon microscopy. Nat Methods 2:932-940.

Helmchen F, Svoboda K, Denk W, Tank DW (1999) In vivo dendritic calcium dynamics in deep-layer cortical pyramidal neurons. In: Nature Neuroscience, pp 989-996.

Hill DN, Varga Z, Jia H, Sakmann B, Konnerth A (2013) Multibranch activity in basal and tuft dendrites during firing of layer 5 cortical neurons in vivo. In: Proceedings of the National Academy of Sciences, pp 13618-13623.

Hira R, Ohkubo F, Masamizu Y, Ohkura M, Nakai J, Okada T, Matsuzaki M (2014) Reward-timing-dependent bidirectional modulation of cortical microcircuits during optical single-neuron operant conditioning. Nature communications 5:5551.

Hira R, Ohkubo F, Ozawa K, Isomura Y, Kitamura K, Kano M, Kasai H, Matsuzaki M (2013) Spatiotemporal Dynamics of Functional Clusters of Neurons in the Mouse Motor Cortex during a Voluntary Movement. Journal of Neuroscience 33:1377-1390.

Holtmaat A, Wilbrecht L, Knott GW, Welker E, Svoboda K (2006) Experience-dependent and cell-type-specific spine growth in the neocortex. Nature 441:979-983.

Holtmaat A, Bonhoeffer T, Chow DK, Chuckowree J, De Paola V, Hofer SB, Hübener M, Keck T, Knott G, Lee W-CA, Mostany R, Mrsic-Flogel TD, Nedivi E, Portera-Cailliau C, Svoboda K, Trachtenberg JT, Wilbrecht L (2009) Long-term, high-resolution imaging in the mouse neocortex through a chronic cranial window. In: Nat Protoc, pp 1128-1144.

Hooks BM, Mao T, Gutnisky DA, Yamawaki N, Svoboda K, Shepherd GMG (2013) Organization of Cortical and Thalamic Input to Pyramidal Neurons in Mouse Motor Cortex. Journal of Neuroscience 33:748-760.

Hopfield JJ (1982) Neural networks and physical systems with emergent collective computational abilities. Proceedings of the National Academy of Sciences of the United States of America 79:2554-2558.

Hosp JA, Pekanovic A, Rioult-Pedotti MS, Luft AR (2011) Dopaminergic Projections from Midbrain to Primary Motor Cortex Mediate Motor Skill Learning. Journal of Neuroscience 31:2481-2487.

Hubel DH, Wiesel TN (1959) Receptive fields of single neurones in the cat's striate cortex. J Physiol 148:574-591.

Huber D, Gutnisky DA, Peron S, O'Connor DH, Wiegert JS, Tian L, Oertner TG, Looger LL, Svoboda K (2012) Multiple dynamic representations in the motor cortex during sensorimotor learning. In: Nature, pp 473-478.

Inoue M, Takeuchi A, Horigane S, Ohkura M, Gengyo-Ando K, Fujii H, Kamijo S, Takemoto-Kimura S, Kano M, Nakai J, Kitamura K, Bito H (2014) Rational design of a high-affinity, fast, red calcium indicator R-CaMP2. Nat Methods.

Ishikawa D, Matsumoto N, Sakaguchi T, Matsuki N, Ikegaya Y (2014) Operant conditioning of synaptic and spiking activity patterns in single hippocampal neurons. J Neurosci 34:5044-5053.

Isomura Y, Harukuni R, Takekawa T, Aizawa H, Fukai T (2009) Microcircuitry coordination of cortical motor information in self-initiation of voluntary movements. Nature Neuroscience 12:1586-1593.

Izhikevich EM (2006) Solving the Distal Reward Problem through Linkage of STDP and Dopamine Signaling. Cerebral Cortex 17:2443-2452.

Jarosiewicz B, Chase SM, Fraser GW, Velliste M, Kass RE, Schwartz AB (2008) Functional network reorganization during learning in a brain-computer interface paradigm. Proceedings of the National Academy of Sciences 105:19486-19491.

Jeanne JM, Sharpee TO, Gentner TQ (2013) Associative learning enhances population coding by inverting interneuronal correlation patterns. Neuron 78:352-363.

Jia H, Rochefort NL, Chen X, Konnerth A (2010) Dendritic organization of sensory input to cortical neurons in vivo. In: Nature, pp 1307-1312.

Kalaska JF, Caminiti R, Georgopoulos AP (1983) Cortical mechanisms related to the direction of two-dimensional arm movements: relations in parietal area 5 and comparison with motor cortex. Exp Brain Res 51:247-260.

Kandel ER (2013) Principles of neural science, 5th Edition. New York: McGraw-Hill.

Kaneko T (2013) Local connections of excitatory neurons in motor-associated cortical areas of the rat. Frontiers in neural circuits 7:75.

Katona G, Szalay G, Maak P, Kaszas A, Veress M, Hillier D, Chiovini B, Vizi ES, Roska B, Rozsa B (2012) Fast two-photon in vivo imaging with three-dimensional random-access scanning in large tissue volumes. Nat Methods 9:201-208.

Kawaguchi Y, Kubota Y (1993) Correlation of physiological subgroupings of nonpyramidal cells with parvalbumin- and calbindinD28k-immunoreactive neurons in layer V of rat frontal cortex. J Neurophysiol 70:387-396.

Kawaguchi Y, Kubota Y (1998) Neurochemical features and synaptic connections of large physiologically-identified GABAergic cells in the rat frontal cortex. Neuroscience 85:677-701.

Kenet T, Bibitchkov D, Tsodyks M, Grinvald A, Arieli A (2003) Spontaneously emerging cortical representations of visual attributes. Nature 425:954-956.

Kerlin AM, Andermann ML, Berezovskii VK, Reid RC (2010) Broadly tuned response properties of diverse inhibitory neuron subtypes in mouse visual cortex. Neuron 67:858-871.

Ko H, Hofer SB, Pichler B, Buchanan KA, Sjöström PJ, Mrsic-Flogel TD (2011) Functional specificity of local synaptic connections in neocortical networks. Nature 473:87-91.

Kobayashi S, Schultz W, Sakagami M (2010) Operant conditioning of primate prefrontal neurons. Journal of Neurophysiology 103:1843-1855.

Komiyama T, Sato TR, O'Connor DH, Zhang Y-X, Huber D, Hooks BM, Gabitto M, Svoboda K (2010) Learning-related fine-scale specificity imaged in motor cortex circuits of behaving mice. In: Nature, Nature Publishing Group Edition, pp 1182-1186: Nature Publishing Group.

Koralek AC, Costa RM, Carmena JM (2013) Temporally precise cell-specific coherence develops in corticostriatal networks during learning. Neuron 79:865-872.

Koralek AC, Jin X, Long I, John D, Costa RM, Carmena JM (2012) Corticostriatal plasticity is necessary for learning intentional neuroprosthetic skills. In: Nature, pp 331-335.

Kuramoto E, Furuta T, Nakamura KC, Unzai T, Hioki H, Kaneko T (2009) Two types of thalamocortical projections from the motor thalamic nuclei of the rat: a single neuron-tracing study using viral vectors. Cerebral Cortex 19:2065-2077.

Kuramoto E, Fujiyama F, Nakamura KC, Tanaka Y, Hioki H, Kaneko T (2011) Complementary distribution of glutamatergic cerebellar and GABAergic basal ganglia afferents to the rat motor thalamic nuclei. The European journal of neuroscience 33:95-109.

Law AJ, Rivlis G, Schieber MH (2014) Rapid acquisition of novel interface control by small ensembles of arbitrarily selected primary motor cortex neurons. J Neurophysiol 112:1528-1548.

Lebedev MA, Nicolelis MA (2006) Brain-machine interfaces: past, present and future. Trends in neurosciences 29:536-546.

Legenstein R, Pecevski D, Maass W (2008) A learning theory for reward-modulated spike-timing-dependent plasticity with application to biofeedback. PLoS computational biology 4:e1000180.

Legenstein R, Chase SM, Schwartz AB, Maass W (2010) A reward-modulated hebbian learning rule can explain experimentally observed network reorganization in a brain control task. J Neurosci 30:8400-8410.

Li Y, Lu H, Cheng P-l, Ge S, Xu H, Shi S-H, Dan Y (2012) Clonally related visual cortical neurons show similar stimulus feature selectivity. Nature 486:118-121.

London M, Häusser M (2005) DENDRITIC COMPUTATION. In: Annu. Rev. Neurosci., pp 503-532.

Long MA, Jin DZ, Fee MS (2010) Support for a synaptic chain model of neuronal sequence generation. In: Nature, pp 394-399.

Losonczy A, Magee JC (2006) Integrative Properties of Radial Oblique Dendrites in Hippocampal CA1 Pyramidal Neurons. In: Neuron, pp 291-307.

Losonczy A, Makara JK, Magee JC (2008) Compartmentalized dendritic plasticity and input feature storage in neurons. Nature 452:436-441.

Lutcke H, Margolis DJ, Helmchen F (2013) Steady or changing? Long-term monitoring of neuronal population activity. Trends in neurosciences 36:375-384.

MacLean JN, Watson BO, Aaron GB, Yuste R (2005) Internal dynamics determine the cortical response to thalamic stimulation. Neuron 48:811-823.

Makara JK, Losonczy A, Wen Q, Magee JC (2009) Experience-dependent compartmentalized dendritic plasticity in rat hippocampal CA1 pyramidal neurons. In: Nature Neuroscience, pp 1485-1487.

Malone LA, Vasudevan EVL, Bastian AJ (2011) Motor adaptation training for faster relearning. Journal of Neuroscience 31:15136-15143.

Mank M, Santos AF, Direnberger S, Mrsic-Flogel TD, Hofer SB, Stein V, Hendel T, Reiff DF, Levelt C, Borst A, Bonhoeffer T, Hübener M, Griesbeck O (2008) A genetically encoded calcium indicator for chronic in vivo two-photon imaging. Nature methods 5:805-811.

Mante V, Sussillo D, Shenoy KV, Newsome WT (2013) Context-dependent computation by recurrent dynamics in prefrontal cortex. Nature 503:78-84.

Markram H, Lubke J, Frotscher M, Sakmann B (1997) Regulation of synaptic efficacy by coincidence of postsynaptic APs and EPSPs. Science 275:213-215.

Markram H, Toledo-Rodriguez M, Wang Y, Gupta A, Silberberg G, Wu C (2004) Interneurons of the neocortical inhibitory system. Nature reviews Neuroscience 5:793-807.

Matsuzaki M, Honkura N, Ellis-Davies GCR, Kasai H (2004) Structural basis of long-term potentiation in single dendritic spines. Nature 429:761-766.

Matsuzaki M, Ellis-Davies GCR, Nemoto T, Miyashita Y, Iino M, Kasai H (2001) Dendritic spine geometry is critical for AMPA receptor expression in hippocampal CA1 pyramidal neurons. Nature Neuroscience 4:1086-1092.

Medina JF, Garcia KS, Mauk MD (2001) A mechanism for savings in the cerebellum. Journal of Neuroscience 21:4081-4089.

Miller JE, Ayzenshtat I, Carrillo-Reid L, Yuste R (2014) Visual stimuli recruit intrinsically generated cortical ensembles. Proceedings of the National Academy of Sciences of the United States of America 111:E4053-4061.

Mitchell JF, Sundberg KA, Reynolds JH (2009) Spatial attention decorrelates intrinsic activity fluctuations in macaque area V4. Neuron 63:879-888.

Molitoris BA, Sandoval RM (2005) Intravital multiphoton microscopy of dynamic renal processes. American journal of physiology Renal physiology 288:F1084-1089.

Monahan PE, Samulski RJ (2000) Adeno-associated virus vectors for gene therapy: more pros than cons? Molecular medicine today 6:433-440.

Moritz CT, Fetz EE (2011) Volitional control of single cortical neurons in a brain-machine interface. Journal of neural engineering 8:025017.

Moritz CT, Perlmutter SI, Fetz EE (2008) Direct control of paralysed muscles by cortical neurons. Nature 456:639-642.

Nagai T, Yamada S, Tominaga T, Ichikawa M, Miyawaki A (2004) Expanded dynamic range of fluorescent indicators for Ca(2+) by circularly permuted yellow fluorescent proteins. Proc Natl Acad Sci U S A 101:10554-10559.

Nakai J, Ohkura M, Imoto K (2001) A high signal-to-noise Ca(2+) probe composed of a single green fluorescent protein. Nat Biotechnol 19:137-141.

Nicolelis MA, Lebedev MA (2009) Principles of neural ensemble physiology underlying the operation of brain-machine interfaces. Nature reviews Neuroscience 10:530-540.

Nicolelis MA, Fanselow EE, Ghazanfar AA (1997) Hebb's dream: the resurgence of cell assemblies. Neuron 19:219-221.

Nimchinsky EA, Sabatini BL, Svoboda K (2002) Structure and function of dendritic spines. Annual review of physiology 64:313-353.

Niv Y, Duff MO, Dayan P (2005) Dopamine, uncertainty and TD learning. Behavioral and brain functions : BBF 1:6.

O'Keefe J, Dostrovsky J (1971) The hippocampus as a spatial map. Preliminary evidence from unit activity in the freely-moving rat. Brain Res 34:171-175.

O'Keefe J, Recce ML (1993) Phase relationship between hippocampal place units and the EEG theta rhythm. Hippocampus 3:317-330.

Oh SW et al. (2014) A mesoscale connectome of the mouse brain. Nature 508:207-214.

Ohki K, Chung S, Ch'ng YH, Kara P, Reid RC (2005) Functional imaging with cellular resolution reveals precise micro-architecture in visual cortex. Nature 433:597-603.

Ohki K, Chung S, Kara P, Hübener M, Bonhoeffer T, Reid RC (2006) Highly ordered arrangement of single neurons in orientation pinwheels. Nature 442:925-928.

Ohtsuki G, Nishiyama M, Yoshida T, Murakami T, Histed M, Lois C, Ohki K (2012) Similarity of visual selectivity among clonally related neurons in visual cortex. Neuron 75:65-72.

Packer AM, Roska B, Häusser M (2013) Targeting neurons and photons for optogenetics. Nature Neuroscience 16:805-815.

Packer AM, Russell LE, Dalgleish HW, Hausser M (2014) Simultaneous all-optical manipulation and recording of neural circuit activity with cellular resolution in vivo. Nat Methods.

Packer AM, Peterka DS, Hirtz JJ, Prakash R, Deisseroth K, Yuste R (2012) Two-photon optogenetics of dendritic spines and neural circuits. Nature methods 9:1202-1205.

Palmer LM, Shai AS, Reeve JE, Anderson HL, Paulsen O, Larkum ME (2014) NMDA spikes enhance action potential generation during sensory input. Nature neuroscience 17:383-390.

Paukert M, Bergles DE (2012) Reduction of motion artifacts during in vivo two-photon imaging of brain through heartbeat triggered scanning. The Journal of physiology 590:2955-2963.

Peterka DS, Takahashi H, Yuste R (2011) Imaging voltage in neurons. Neuron 69:9-21.

Peters AJ, Chen SX, Komiyama T (2014) Emergence of reproducible spatiotemporal activity during motor learning. Nature 510:263-267.

Petreanu L, Gutnisky DA, Huber D, Xu N-L, O'Connor DH, Tian L, Looger L, Svoboda K (2012) Activity in motor-sensory projections reveals distributed coding in somatosensation. Nature.

Poirazi P, Brannon T, Mel BW (2003) Pyramidal neuron as two-layer neural network. Neuron 37:989-999.

Pologruto TA, Sabatini BL, Svoboda K (2003) ScanImage: flexible software for operating laser scanning microscopes. Biomedical engineering online 2:13.

Poulet JFA, Petersen CCH (2008) Internal brain state regulates membrane potential synchrony in barrel cortex of behaving mice. Nature 454:881-885.

Prakash R, Yizhar O, Grewe B, Ramakrishnan C, Wang N, Goshen I, Packer AM, Peterka DS, Yuste R, Schnitzer MJ, Deisseroth K (2012) Two-photon optogenetic toolbox for fast inhibition, excitation and bistable modulation. Nature methods 9:1171-1179.

Rickgauer JP, Deisseroth K, Tank DW (2014) Simultaneous cellular-resolution optical perturbation and imaging of place cell firing fields. Nat Neurosci 17:1816-1824.

Rubart M (2004) Two-photon microscopy of cells and tissue. Circulation research 95:1154-1166.

Sadtler PT, Quick KM, Golub MD, Chase SM, Ryu SI, Tyler-Kabara EC, Yu BM, Batista AP (2014) Neural constraints on learning. Nature 512:423-426.

Sakurai Y, Takahashi S (2012) Conditioned enhancement of firing rates and synchrony of hippocampal neurons and firing rates of motor cortical neurons in rats. The European journal of neuroscience.

Sauer B (1998) Inducible gene targeting in mice using the Cre/lox system. Methods 14:381-392.

Schafer RJ, Moore T (2011) Selective Attention from Voluntary Control of Neurons in Prefrontal Cortex. Science (New York, NY) 332:1568-1571.

Schultz W (2006) Behavioral Theories and the Neurophysiology of Reward. Annual Review of Psychology 57:87-115.

Schultz W, Dayan P, Montague PR (1997) A neural substrate of prediction and reward. Science (New York, NY) 275:1593-1599.

Shadlen MN, Newsome WT (1998) The variable discharge of cortical neurons: implications for connectivity, computation, and information

coding. The Journal of neuroscience : the official journal of the Society for Neuroscience 18:3870-3896.

Sheffield ME, Dombeck DA (2014) Calcium transient prevalence across the dendritic arbour predicts place field properties. Nature.

Shenoy KV, Sahani M, Churchland MM (2013) Cortical control of arm movements: a dynamical systems perspective. Annual review of neuroscience 36:337-359.

Shepherd GMG (2013) Corticostriatal connectivity and its role in disease. Nature Reviews Neuroscience 14:278-291.

Shibata K, Watanabe T, Sasaki Y, Kawato M (2011) Perceptual Learning Incepted by Decoded fMRI Neurofeedback Without Stimulus Presentation. In: Science, pp 1413-1415.

Slotnick B (2009) A simple 2-transistor touch or lick detector circuit. Journal of the experimental analysis of behavior 91:253-255.

Smith SL, Häusser M (2010) Parallel processing of visual space by neighboring neurons in mouse visual cortex. Nature Neuroscience 13:1144-1149.

Smith SL, Smith IT, Branco T, Häusser M (2013) Dendritic spikes enhance stimulus selectivity in cortical neurons in vivo. In: Nature, pp 115-120.

Sohal VS, Zhang F, Yizhar O, Deisseroth K (2009) Parvalbumin neurons and gamma rhythms enhance cortical circuit performance. Nature 459:698-702.

Stosiek C, Garaschuk O, Holthoff K, Konnerth A (2003) In vivo two-photon calcium imaging of neuronal networks. Proc Natl Acad Sci U S A 100:7319-7324.

Stuart G, Spruston N, Häusser M (2007) Dendrites, 2nd Edition. Oxford ; New York: Oxford University Press.

Svoboda K, Yasuda R (2006) Principles of Two-Photon Excitation Microscopy and Its Applications to Neuroscience. Neuron 50:823-839.

Takahashi N, Kitamura K, Matsuo N, Mayford M, Kano M, Matsuki N, Ikegaya Y (2012) Locally Synchronized Synaptic Inputs. Science (New York, NY) 335:353-356.

Taniguchi H, He M, Wu P, Kim S, Paik R, Sugino K, Kvitsiani D, Fu Y, Lu J, Lin Y, Miyoshi G, Shima Y, Fishell G, Nelson SB, Huang ZJ (2011) A resource of Cre driver lines for genetic targeting of GABAergic neurons in cerebral cortex. Neuron 71:995-1013.

Thestrup T, Litzlbauer J, Bartholomaus I, Mues M, Russo L, Dana H, Kovalchuk Y, Liang Y, Kalamakis G, Laukat Y, Becker S, Witte G, Geiger A, Allen T, Rome LC, Chen TW, Kim DS, Garaschuk O, Griesinger C, Griesbeck O (2014) Optimized ratiometric calcium sensors for functional in vivo imaging of neurons and T lymphocytes. Nat Methods 11:175-182.

Thevenaz P, Ruttimann UE, Unser M (1998) A pyramid approach to subpixel registration based on intensity. IEEE transactions on image processing : a publication of the IEEE Signal Processing Society 7:27-41.

Thompson RF, Sindberg RM (1960) Auditory response fields in association and motor cortex of cat. J Neurophysiol 23:87-105.

Thomson AM, Lamy C (2007) Functional maps of neocortical local circuitry. Front Neurosci 1:19-42.

Tian L, Hires SA, Mao T, Huber D, Chiappe ME, Chalasani SH, Petreanu L, Akerboom J, McKinney SA, Schreiter ER, Bargmann CI, Jayaraman V, Svoboda K, Looger LL (2009) Imaging neural activity in worms, flies and mice with improved GCaMP calcium indicators. Nature methods 6:875-881.

Trachtenberg JT, Chen BE, Knott GW, Feng G, Sanes JR, Welker E, Svoboda K (2002) Long-term in vivo imaging of experience-dependent synaptic plasticity in adult cortex. Nature 420:788-794.

Tsai HC, Zhang F, Adamantidis A, Stuber GD, Bonci A, de Lecea L, Deisseroth K (2009) Phasic Firing in Dopaminergic Neurons Is Sufficient for Behavioral Conditioning. Science (New York, NY) 324:1080-1084.

Tye KM, Mirzabekov JJ, Warden MR, Ferenczi EA, Tsai H-C, Finkelstein J, Kim S-Y, Adhikari A, Thompson KR, Andalman AS, Gunaydin LA, Witten IB, Deisseroth K (2013) Dopamine neurons modulate neural encoding and expression of depression-related behaviour. Nature 493:537-541.

Uchida N, Poo C, Haddad R (2014) Coding and transformations in the olfactory system. Annu Rev Neurosci 37:363-385.

Vogelstein JT, Watson BO, Packer AM, Yuste R, Jedynak B, Paninski L (2009) Spike Inference from Calcium Imaging Using Sequential Monte Carlo Methods. In: Biophysical Journal, pp 636-655.

Vogelstein JT, Packer AM, Machado TA, Sippy T, Babadi B, Yuste R, Paninski L (2010) Fast Nonnegative Deconvolution for Spike Train Inference From Population Calcium Imaging. In: Journal of Neurophysiology, pp 3691-3704.

Wallace DJ, Kerr JN (2010) Chasing the cell assembly. Current opinion in neurobiology 20:296-305.

Waters J (2004) Boosting of Action Potential Backpropagation by Neocortical Network Activity In Vivo. In: Journal of Neuroscience, pp 11127-11136.

Weiler N, Wood L, Yu J, Solla SA, Shepherd GMG (2008) Top-down laminar organization of the excitatory network in motor cortex. Nature Neuroscience 11:360-366.

Wessberg J, Stambaugh CR, Kralik JD, Beck PD, Laubach M, Chapin JK, Kim J, Biggs SJ, Srinivasan MA, Nicolelis MA (2000) Real-time prediction of hand trajectory by ensembles of cortical neurons in primates. Nature 408:361-365.

Wise RA (1996) Addictive drugs and brain stimulation reward. Annu Rev Neurosci 19:319-340.

Wise RA, Wise RA, Rompre PP, Rompre PP (1989) Brain Dopamine and Reward. Annual Review of Psychology 40:191-225.

Xu N-L, Harnett MT, Williams SR, Huber D, O'Connor DH, Svoboda K, Magee JC (2012a) Nonlinear dendritic integration of sensory and motor input during an active sensing task. In: Nature, pp 247-251.

Xu S, Jiang W, Poo M-M, Dan Y (2012b) Activity recall in a visual cortical ensemble. In: Nature Neuroscience, pp 449-455.

Xu T, Yu X, Perlik AJ, Tobin WF, Zweig JA, Tennant K, Jones T, Zuo Y (2009) Rapid formation and selective stabilization of synapses for enduring motor memories. Nature 462:915-919.

Yaksi E, Friedrich RW (2006) Reconstruction of firing rate changes across neuronal populations by temporally deconvolved Ca2+ imaging. In: Nature Methods, pp 377-383.

Yang G, Pan F, Gan W-B (2009) Stably maintained dendritic spines are associated with lifelong memories. Nature 462:920-924.

Yizhar O, Fenno LE, Davidson TJ, Mogri M, Deisseroth K (2011) Optogenetics in Neural Systems. Neuron 71:9-34.

Yu Y-C, Bultje RS, Wang X, Shi S-H (2009) Specific synapses develop preferentially among sister excitatory neurons in the neocortex. Nature 458:501-504.

Yu YC, He S, Chen S, Fu Y, Brown KN, Yao XH, Ma J, Gao KP, Sosinsky GE, Huang K, Shi SH (2012) Preferential electrical coupling regulates neocortical lineage-dependent microcircuit assembly. Nature 486:113-117.

Zariwala HA, Borghuis BG, Hoogland TM, Madisen L, Tian L, De Zeeuw CI, Zeng H, Looger LL, Svoboda K, Chen T-W (2012) A Cre-dependent GCaMP3 reporter mouse for neuronal imaging in vivo. Journal of Neuroscience 32:3131-3141.

Zhang F, Wang LP, Brauner M, Liewald JF, Kay K, Watzke N, Wood PG, Bamberg E, Nagel G, Gottschalk A, Deisseroth K (2007) Multimodal fast optical interrogation of neural circuitry. Nature 446:633-639.

Zhang W, Linden DJ (2003) The other side of the engram: experience-driven changes in neuronal intrinsic excitability. Nature reviews Neuroscience 4:885-900.

Zhao Y, Araki S, Wu J, Teramoto T, Chang YF, Nakano M, Abdelfattah AS, Fujiwara M, Ishihara T, Nagai T, Campbell RE (2011) An Expanded Palette of Genetically Encoded Ca2+ Indicators. Science (New York, NY) 333:1888-1891.

Zipfel WR, Williams RM, Webb WW (2003) Nonlinear magic: multiphoton microscopy in the biosciences. Nat Biotechnol 21:1369-1377.